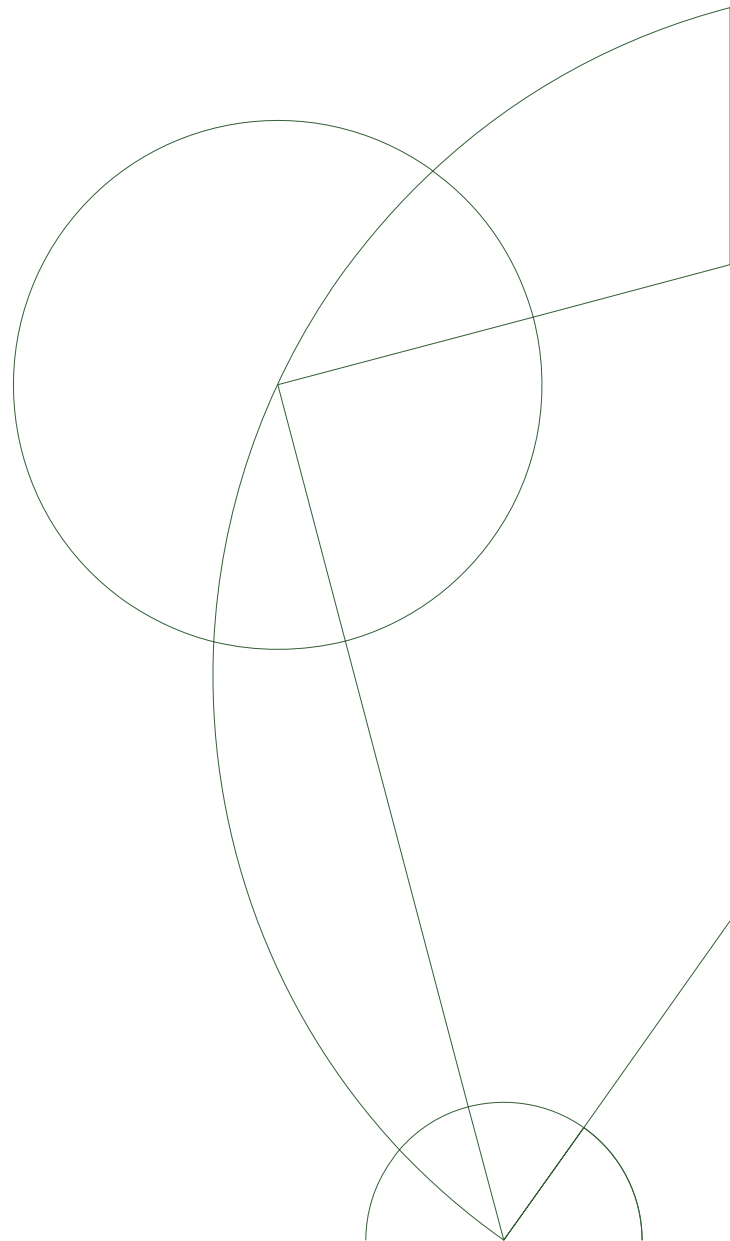# Master Thesis
Dust Dynamics in Molecular Clouds

Mark Falkenstrøm (tph679)

Supervisor - Troels Haugbølle & Aake Nordlund

Niels Bohr Institute - University of Copenhagen (Københavns Universitet)

May 20, 2021

Abstract

The DISPATCH framework is used to simulate molecular clouds of different sizes, containing gas and dust with a range of different dust particle sizes. A correlation between the dust particles and gas is found, with larger dust particles being less coupled to the gas. A dust particle size of approximately $50\mu m$ is found as the transition size where dust particles larger than this will mostly be decoupled from the gas at all scales. The scale independence of this result is related to the approximately constant column density seen across molecular clouds at different sizes. A latency is found between gas and dust particles, which makes dust particles react to a change in the direction of the gas, after the gas has already changed its direction. Dust particles of size $100\mu m$ are found to have a weak coupling to the gas, creating filaments of dust outside the filaments of gas. The largest velocity dispersion for the dust is found where the dust density is largest. These discoveries suggests a coherent movement of dust particles through molecular clouds, creating overdensities where groups of coherent dust motions overlap. The probability density function of the dust and gas shows an expansion-like behaviour from high dust density regions towards low dust density regions. A power law relation is found between the mean dust v_{rms} and the size of the molecular cloud, with an increasing mean dust v_{rms} for an increasing molecular cloud size. This power law behaviour is closely related to the famous Larson relations observed for the gas in molecular clouds, but is a novel result for dust grains. The power law relation is found to be different for different sized dust particles. A power law relation, for dust particles smaller than $1\mu m$, is also found between the average difference in the reference frame between the dust and gas velocity and the size of the molecular cloud observed as well as between the average difference in the reference frame between the dust and gas velocity and the size of the dust particle observed.

Table of Contents

1   Introduction

How molecular clouds (MCs) and giant molecular clouds (GMCs) are created has been a big question since the late 20th century. Today it is the common belief of astrophysicists that MCs/GMCs may originate from energy injection by stellar feedback and self-gravitating instabilities in the interstellar medium, having its formation and properties influenced by galactic turbulence associated with the magnetorotational instability (MRI), [1] as well as orbital dynamics and dissipative cloud-cloud collisions. This is clearly a complicated process, with a lot of different dynamics dictating the structure and properties of these MCs/GMCs primarily present in spiral galaxies [2]. One of the most interesting phenomenons of MCs/GMSs is the formation of stars, which almost exclusively happens inside of these giant clouds of gas and dust. In Mathewson, van der Kruit, and Brouw 1972, an estimate is made of needing 10^7 years to create a star inside of a MC/GMC with no external forces required [3] [4]. Star formation was described in 1987 by Shu, Adams, & Lizano, who knew that stars are made from massive gas clumps collapsing from self gravitation, but the question of how the massive gas clumps are created was somewhat a mystery to them. They suggested that there are two ways this accumulation of gas in MCs/GMCs can occur: either through some process of hierarchical fragmentation, or that stellar formation is intrinsically an accretion process where a small initial mass is accreted into a larger mass [5]. Nevertheless what they did not consider was turbulence, which has since been discovered to be an important property in star formation in MCs/GMCs in the Inter-Stellar Medium (ISM). This supersonic turbulence in MCs/GMCs creates over-dense regions, which become so dense that the self gravitation of these regions overpower the force of the turbulence, in a free-fall collapse, ultimately resulting in star formation [6].

The great difficulty of observing processes inside MCs/GMCs lies in MCs/GMCs primarily being made up of H_2, which lacks a permanent dipole moment, and therefore has no easily observational rotational transitions. Thus, most observational studies of shocks and regions containing high levels of ultraviolet emission in MCs/GMCs use rovibrational and fluorescent transitions for observational purposes. If observational astronomers want to explore physical conditions in other regions of MCs/GMCs, they need to use tracers like molecules other than H_2 and dust. Molecules colliding with H_2 excite different rotational transitions, which we are able to observe. The most common tracers in MCs/GMCs are a range of isotopic variants of CO, which can help determine global physical conditions of MCs/GMCs, such as the temperature and volume density [7]. In order to make dynamics of dust and gas inside MCs/GMCs easier accessible one can use numerical simulations. In such simulations it is possible to use already observed properties of MCs/GMCs and reproduce them computationally. This makes it possible to explore different properties of MCs/GMCs and explore how a change in parameters could impact the dynamics inside a MC/GMC.

The gas dynamics in MCs/GMCs are interesting when studying star formation, but what about the dust dynamics in MCs/GMCs? In 1993 Jack J. Lissauer concluded that the planets in our solar system were formed inside a protostellar disc, which remained after the sun was almost formed, having a large dust density. He also refers to a planet found outside of the solar system discovered by Wolszczan and Frail in 1992, but he could not conclude that planet formation also occurs outside of the solar system [8] [9]. The "maybe-planet" referred to by Lissauer was indeed a planet, and it was one of the first exoplanets ever discovered. From then, the number of exoplanets discovered has continued to grow. With telescopes like Kepler [10], Hubble [11] and TESS [12], more than 4000 exoplanets have been confirmed and more are discovered every day [13]. With the help of new telescopes such as the James Webb telescope, we will be able to explore these exoplanets in greater detail. With the James Webb Telescope it will be possible to investigate the chemical properties of planetary systems, and thereby understand the genesis

of planets even better than we do today [14]. Thus, the dynamics of dust in MCs/GMCs from single dust particles to planets is of great interest in the field of early planet formation in astrophysics today.

The subject of protoplanetary discs, and the formation of planets inside of these, are well described, researched, and simulated, although by no means fully understood. These subjects are continuously developed upon, with new discoveries constantly made [15] [16]. One thing missing from these simulations and calculations is the dust contributions made from the surrounding MC/GMC. Interactions of dust molecules in MCs/GMCs can lead to different sizes of molecular dust due to coagulation and destruction of dust particles. Molecular dust can interact differently with the protoplanetary systems depending on the size of the dust particles [17] [18]. This means that the dust dynamics in MCs/GMCs can help us get a better understanding of planet formation. Both in the form of a contribution of dust when the planet formation phase has begun, but also how dust becomes present, in the regions of self-gravitating dust clouds on their way to becoming protostellar clouds, in such a quantity that it can end up creating planets in a protoplanetary disc.

Having some universal laws of how dust behaves inside a MC/GMC, which describes relations between quantities observable from telescopes, could possibly help us determine which MCs/GMCs are more probable to be cradles for planet formation. Knowing more about where dust accumulates can also illuminate how eight planets can be present within our own solar system. Additionally, where to find other planetary systems with a large number of planets revolving around the same sun. According to Tom Barclay, of NASA's Ames Research Center in Moffett Field, California: *"If you do not have giant planets in your system, you have a very, very different planetary system"*. Tom is highlighting the giant gas planets shielding Earth and the inner terrestrial planets from asteroids, that would otherwise potentially have destroyed the possibility of life to form [19]. Knowing more about the dust dynamics in MCs/GMCs could therefore potentially help us find over-dense regions with the right composition for giant gas planets to form around inner terrestrial planets, which possibly can be a necessity for life.

In this thesis we study dust dynamics inside MCs and GMCs, simulated with the use of the DISPATCH code, using the HLLC adapted from the RAMSES code. These experiments are performed to find a relationship between how dust moves in a MC/GMC on average compared to how gas moves inside a MC or a GMC. Section 2 of this thesis gives an introduction to the Larson relations, and the physics already developed to explore dynamics inside MCs and GMCs, with a focus on how the size of a dust particle can affect its dynamics inside a MC or GMC. Lastly, section 2 gives an introduction to shocks and turbulence inside MCs and GMCs. Section 3 Explains the DISPATCH and RAMSES framework, and how it is used to create the experiments needed to analyze the behaviour of dust in MCs and GMCs. Section 4 explains the setup used, and the inputs and boundaries given in the experiments, when using the DISPATCH framework to generate data, as well as presenting quantitative results from analysing the average root mean square velocity for the dust at different dust sizes in different sizes of MC and GMC experiments, compared to gas dynamics inside the clouds. Section 5 discusses the future work needed in order to build on top of the work performed throughout this thesis.

2   Molecular Cloud Dynamics

2.1   Larson Relations

In order to explain the dynamical state of a MC/GMC we need to look at the Larson Relations, also called the Larson laws. There are three Larson laws, which are all important when analyzing

MCs/GMCs. The three Larson laws according to Heyer et al. (2009) (notice that the second Larson relation here is different than in Heyer et al (2009) due to a typo in their article, and the relation in the original Larson (1981) paper is instead used) are given by [20] [21]:

$$\sigma_v \sim 1.2 km/s \cdot \left(\frac{L}{1pc}\right)^{0.38} , \tag{1}$$

$$2\sigma_v^2 L/GM \sim 1 , \tag{2}$$

$$n \sim n_0 \left(\frac{L}{1pc}\right)^{-1.1} . \tag{3}$$

The first Larson law gives a power law relationship between the velocity dispersion (σ_v) and the size of the cloud (L), the second Larson law ensures self-gravitating equilibrium in MCs/GMCs and the third Larson law is an inverse relationship between the mean density n and the size of the cloud L. What the Larson laws provide are basically scaling relations between some of the most well-known observable quantities of MCs/GMCs, which can be used when investigating the dynamics of MCs/GMCs [20].

2.2   Evolution of dust and gas in a MC/GMC

The Mach number of an experiment is a measure of whether the gas the particles are moving through is in (or a fluid) is in a subsonic ($M < 1$), a transonic ($M = 1$), a supersonic ($5 > M > 1$), or a hypersonic ($M > 5$) regime. The Mach number regime of the medium can be important for compression in front of the particle, as the drag in a supersonic and hypersonic environment can be much larger than in the subsonic or transonic regimes [22]. The Mach number is given by the ratio between the velocity dispersion and the speed of sound inside a medium. The definition of the Mach number can be seen in equation 4, where the definition of the velocity dispersion, from the first Larson relation, has been used (equation 1), if we use a sound speed of $0.18 km/s$ for a gas with temperature $10K$ [23]

$$M = \frac{\sigma_v}{c_s} = 6.7 \cdot L^{0.38} . \tag{4}$$

If we look at the radial evolution of dust inside a system consisting of gas and dust only, the dust will not dynamically affect the gas if the dust to gas ratio is in the order of 10^{-2}, contrarily the gas will affect the dynamics of the dust. In order to describe the evolution of dust and gas, we need to define the eddy turn-over time and the stopping time of a system. The stopping time of a particle is given by the ratio of the momentum and the drag force acting on it. Depending on the ratio of the mean free path (λ_{mfp}) of the gas molecules and the dust particle size a, as well as the the Reynolds number ($Re = 2au/\nu_{mol}$, where u is the velocity of the dust particle with respect to the gas and ν_{mol} is the gas molecular viscosity) there are four different regimes for the drag force acting on the particle [17].

The mean free path is given by $\lambda_{mfp} = 1/n\sigma_{H_2}$ where n is the mid-plane number density and $\sigma_{H_2} \approx 2 \cdot 10^{-15} cm^2$. If the typical dust particle size is negligible compared to the mean free path of the gas particles, the dust particles are surrounded by a dilute gas phase and we can assume the dust particles to be in the Epstein regime. More specifically, in order to be in the Epstein regime we need $\lambda_{mfp}/a \gtrsim \frac{4}{9}$ [24] [17]. For this thesis I assume the dust to be in the Epstein regime as we investigate MCs/GMCs. MCs/GMCs have low average densities and therefore it is safe to assume that the dust particle sizes will be small compared to the mean free path of the gas [25]. The stopping time for subsonic particles in the Epstein regime is given by:

$$t_s = \frac{4}{3}\frac{\rho_s a}{\rho_g \bar{u}} \, .$$ (5)

Where the mean thermal velocity of the gas molecules ($\bar{u}$) is given by:

$$\bar{u} = c_s \sqrt{\pi/8} \, .$$ (6)

Here ρ_s is the solid density of the particles, ρ_g is the local gas density and c_s is the speed of sound [17]. The stopping length of a particle is defined as the length a particle can move inside a fluid, before the accumulated mass in front of it is equal to the mass of the particle, i.e. the length over which a particle can travel before being stopped. This stopping length is given by

$$L_{stop} \cdot \langle \rho_g \rangle \pi a^2 = m_p = \frac{4\pi}{3} a^3 \rho_s \, ,$$ (7)

$$L_{stop} = \frac{4a\rho_s}{3\langle \rho_g \rangle} \, .$$ (8)

It is now appropriate to define a characteristic scale length (L) which is the size of the box an experiment is confined inside. From this length scale, we can define the eddy turn over time (also called the dynamical time), for a MC/GMC, which is defined as the time scale for an eddy of length l to undergo a significant distortion [26]. The eddy turn over time is given by

$$t_{turn} = \frac{L}{2 \cdot v_{rms}},$$ (9)

where v_{rms} is the root mean square velocity of the gas flow. The mean root mean square velocity of a gas inside a MC/GMC is given by the first Larson relation in equation 1 [17]. The root means square velocity is a measure of the difference in velocity between two points separated by a distance [27]. Thereby equation 10 can tell us the average velocity difference between two points in the experiment. The correct correlation between the mean gas v_{rms} and the size of the MC/GMC the gas moves around in is actively discussed, and there is a relative big spread in the value to be multiplied by the size of the MC/GMC L, and the factor the size needs to be in the power of, looking at equation 1. In this thesis, 1.2 and 0.38 was chosen, where others might have chosen 1 and 0.4. This would be insignificant as the spread in different observed values of these two numbers are above 10% [20] [21].

$$v_{rms} = \sqrt{\frac{v_1^2 + v_2^2 + v_3^2 + ...v_n^2}{n}} \, .$$ (10)

If we assume that the mass is mostly made up of gas, we can describe the interplay between dust and gas by the Stokes number of the system, which is a dimensionless coupling constant. The Stokes number is a relation between the eddy turn over time (t_{turn}) and the stopping time (t_s) of the system and is given by [17]

$$St = \frac{t_s}{t_{turn}} \, .$$ (11)

Now let us consider a dust particle with size diameter a, that travels through a cloud of gas. This particle will have a cylinder of gas in front of it as it moves through the MC/GMC, illustrated in figure 1.

This allows us to find the mass of the particle moving inside the MC/GMC with the gas column in front of it, defined by

$$m_p = \frac{4}{3}\pi a^3 \rho_s \, .$$ (12)
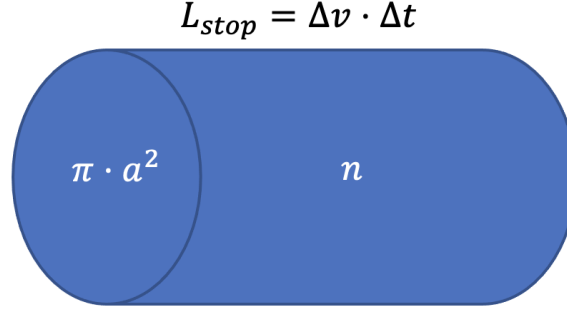
$$L_{stop} = \Delta v \cdot \Delta t$$

Figure 1: Example of a gas column in front of a dust particle inside a MC/GMC, which we can analyze the dynamics and evolution of. a is the radius of the gas column, L_{stop} is the length of the gas column (i.e. the stopping length), Δv is the velocity of the dust particle, Δt is the stopping time, and n is the number density of particles inside the gas column.

From the Larson relations we can define the number density of a region inside a MC/GMC by $n = \frac{n_0}{L/1pc}$, where n_0 is the normalization of the number density, which in my thesis is set to $1200cm^{-3}$. The column density the dust particle will meet in its trajectory in the distance it travels before being stopped (stopping length) L_{stop}, is given by $N = nL_{stop} = n_0(1pc)$. The column density in front of the dust particle will be constant for all different sizes of MCs/GMCs, since n_0 is a constant. The surface density that the dust particles "sees" is given by $\Sigma = N\mu m_p$, where μ is the mean molecular weight being 2.4 in my thesis, and m_p is the proton mass. The surface density can be seen as the average total mass of gas that impacts the dust particle through the cloud. The mass of the gas in the gas column in front of the dust particle is given by

$$m_{gas} = \pi a^2 \Sigma = \pi a^2 \mu m_p n_0 L(1pc) \,. \tag{13}$$

In order to stop a particle inside the MC/GMC, it must meet the condition $L_{stop} < L$, which is the stopping length must be smaller than the length of the experiment. The stopping length is, as previously disclosed, the distance a particle needs to travel in the gas, before it is stopped due to friction. In order for the stopping length to be shorter than the length of the experiment we need the experiment to meet the condition $m_{gas} > m_{dust} = \frac{4\pi}{3}a^3\rho_{solid}$, otherwise the gas will not have a big enough effect on the dust to stop it (m_{gas} is the mass inside the cylinder in front of the particle). If we now set m_{gas} equal to m_{dust}, we will be looking at an experiment exactly where we transition from the particle not being stopped, to the particle being stopped

$$\frac{4\pi}{3}a^3\rho_{solid} = \pi a^2 \mu m_p n_0 L(1pc) \,. \tag{14}$$

Rearranging equation 14 we find the critical value for the size of the dust particle a where particles smaller will be stopped by the gas, but particles larger will not be stopped inside the MC/GMC, the result of this is

$$a_{crit} = \frac{3}{4}\frac{\mu m_p n_0(1pc)}{\rho_{solid}} \,. \tag{15}$$

In my experiments ρ_{solid} was chosen to be $\rho_{solid} = 2gcm^{-3}$. Solving equation 15 by inserting the defined values gives us

$$a_{crit} = \frac{3}{4}\frac{2.4 \cdot 1.673 \cdot 10^{-24}g \cdot 1200cm^{-3} \cdot 3.09 \cdot 10^{18}cm}{2gcm^{-3}} = 55.83\mu m \,. \tag{16}$$

Therefore, a particle with a size smaller than approximately $50\mu m$ will be stopped inside all sizes of MCs/GMCs, and a particle with a size larger than approximately $50\mu m$, will not be

stopped inside all sizes of MCs/GMCs. Next we define the dynamical time. In this case, it is the time it takes before a dust particle in motion fells an effect on its velocity, due to the velocity of the gas. The dynamical time of a particle is defined as the size of the environment we look at divided by the typical velocity of the particle $t_{dyn} = R/v$ [28]. In my experiments I abide by the common interpretation that inside of a periodic box, the distance between two points can at most be $L/2$. Thus, the dynamical time can be expressed as

$$t_{dyn} = \frac{L}{2V_{1pc}(\frac{L}{1pc})^{0.38}} \, , \tag{17}$$

where $(\frac{L}{1pc})^{0.38}$ normalizes the dynamical time to the experiment size chosen. In my setup $V_{1pc} = 1.2km/s$. We now realize that $\rho_g = n\mu m_p$ expresses the gas density as the number density of gas times the mean molecular weight and mass of a proton, and normalize this to Larson's 3rd law by dividing it with the length scale of our experiment L. This is given by

$$\rho_g = \frac{n_{1pc}\mu m_p}{L/1pc} \, . \tag{18}$$

In the reference frame of the dust particle it will, on its journey through the gas column, be bombarded by gas with a bulk and thermal velocity. If the dust particle moves with velocities larger than the speed of sound c_s, the bulk velocity of the gas it is bombarded by is larger than the thermal velocity. This is due to the scaling of equation 6 where c_s is constant. We can neglect the effects of the thermal velocity and the difference in velocity between the dust and the gas is therefore independent of the speed of sound in this regime. In order to define the difference between the dust and gas velocity, we can define the cross section of a dust grain which is given by equation 19. The cross section of a particle gives the probability of interaction between two particles, and if we assume the dust particles to be spherically shaped, the cross section is defined as the area of the circle that goes through the middle of the sphere [29] [30]

$$\sigma_{cross} = \pi a^2 \, , \tag{19}$$

where a is the diameter of the dust particle we are looking at. We can now define the gas mass swept up in front of the dust particle on its way through the experiment. This mass can be set equal to the mass of the particle from equation 5

$$m_{sweep} = \sigma_{cross}\Delta v t_s \rho_g = m_s \, . \tag{20}$$

Rearranging equation 20 and using equation 12 and 18, we find

$$\Delta v t_s = \left(\frac{4\rho_s a}{3}\right)\frac{1}{\rho_g} = \left(\frac{4\rho_s a}{3\rho_0}\right)\frac{L}{1pc} \, . \tag{21}$$

Assuming that t_s follows the Larson scaling similar to the dynamical time from equation 17, we can define:

$$t_s \propto t_{dyn} \propto \frac{L}{v_{rms}} \, . \tag{22}$$

Solving equation 21 for Δv and using the proportionality in equation 22, we get equation 23, which formally valid only as long as the resulting velocity is indeed supersonic as assumed:

$$\Delta v = \left(\frac{4\rho_s a}{3\rho_0 t_s}\right)\frac{L}{1pc} \propto a v_{rms} \, . \tag{23}$$

From equation 23, we can see that the difference between the dust and gas velocity is proportional to the size of the dust particle and the root mean square velocity of the dust particle. Knowing that the v_{rms} of a dust particle is proportional to the size of the MC/GMC, we can thus conclude

that some relation must exist between the average relative difference between the dust and gas velocity, the dust particle size, and the size of the MC/GMC observed. Another way we can define the mean difference between the dust and gas velocity

$$\Delta v = \alpha V_{1pc} \left(\frac{L}{1pc} \right)^{0.38} ,$$
(24)

where α is an amplification factor and V_{1pc} the velocity over the length scale $1pc$. If we insert equation 18 and 24 into the definition of the stopping time in equation 5 we get

$$t_s = \frac{4\rho_s}{3} \frac{(\frac{L}{1pc})^{0.62} a}{\alpha V_{1pc} n_{1pc} \mu m_p} .$$
(25)

When the stopping time of a particle is either equal to or less than the dynamical time, the particle is significantly affected by the gas motion. This can result in the dust particle following the dynamics of the gas and cause accumulation of dust particles. If the stopping time exceeds the dynamical time, the particle will not have enough space inside the experiment, in which the experiment takes place, to be significantly affected by the dynamics of the gas, and the friction force from the gas will act like a stochastic forcing on the dust particle. This is just like the before mentioned case where the stopping time needs to be larger than the size of the experiment. If we set the dynamic time equal to the stopping time, as done in equation 26 (where V_{1pc} is the velocity of the dust particles inside the experiment of size $1^3 pc^3$),

$$\frac{4\rho_s}{3} \frac{(\frac{L}{1pc})^{0.62} a}{\alpha V_{1pc} n_{1pc} \mu m_p} \sim \frac{L}{2V_{1pc}(\frac{L}{1pc})^{0.38}} .$$
(26)

We see that there must exist a size of dust particles a, if we have a fixed experiment size L, where the stopping time exceeds the dynamic time and the particle can not be caught by the gas. We have already found this dust size to be approximately $50\mu m$. The particles exceeding this diameter will either be caught in larger accumulations of gas outside the experiment or they will break apart as a consequence of collision with other dust particles.

2.2.1   Collisions

If a particle that are not caught in accumulations of gas are instead broken apart it can be estimated by looking at the mean free path of the particle given by equation 27.

$$\lambda_{mfp} = \frac{1}{n_{dust}\sigma} ,$$
(27)

where n_{dust} is the number density of particles and σ is the geometric cross-section of a particle defined by $\sigma = \pi a_{coll}^2$, where a_{coll} is the size of the particle. The mean free path is a definition of how long a particle needs to travel on average before it collides with another particle. If the mean free path is larger than the experiment length $1pc$, the particles in our system are unlikely to collide. However, if the mean free path is smaller than the length of our experiment there is a significant probability that the particles collide and break apart. If we look at a 3D volume element of a MC/GMC that has sides larger than the mean free path but smaller than the system size L, collisions between particles drives the velocity of the particles to end up as a Maxwellian distribution, given by

$$F(\vec{v})d^3v = \left(\frac{m}{2\pi kT} \right)^{3/2} exp\left(-\frac{mv^2}{2kT} \right) d^3v .$$
(28)

Here m is the mass of the particle, and T is the kinetic temperature of the gas, which is a measure of the kinetic energy per particle. If we integrate over the Maxwellian distribution in equation 28 we get the mean kinetic energy per particle

$$\frac{1}{2}m\langle v^2\rangle = \frac{3}{2}kT\,.\tag{29}$$

Equation 29 suggests that no matter what extra energy we give the particles inside a volume, they will always, through collision, go back into a kinetic equilibrium with a fixed kinetic temperature T and a fixed average velocity. This transition back to the equilibrium happens in a timescale given by [31]

$$t_{KE} \sim \frac{\lambda_{mfp}}{\langle v^2\rangle^{1/2}} \sim \frac{1}{n\sigma}\left(\frac{m}{3kT}\right)^{1/2}\,.\tag{30}$$

2.3 Self-gravity of the gas, and the Jeans' length

In this sub-section we look schematically at the question of at which scale the self-gravity of the gas might become important. As a simplified representation of the gas dynamics inside a MC/GMC, we can look at the gas as a fluid where the different movements of gas inside the cloud are seen as waves traveling in the cloud. If we look at a MC/GMC, consisting of an ideal gas with no viscosity or heat conduction, and we only look at the gas in one direction, we can define the properties of the gas by its time t and its position x. This means that the cloud has plane parallel symmetry and that the mass continuity equation is given by

$$\frac{\partial \rho}{\partial t} + \frac{\partial}{\partial x}(\rho u) = 0\,,\tag{31}$$

the momentum equation is given by

$$\frac{\partial}{\partial t}(\rho u) + \frac{\partial}{\partial x}\left(\rho u^2\right) = -\frac{\partial P}{\partial x} + g\rho\,,\tag{32}$$

and equation 31 multiplied by the bulk velocity $u(x,t)$ subtracted from equation 32 is given by

$$\rho\frac{\partial u}{\partial t} + \rho u\frac{\partial u}{\partial x} = -\frac{\partial P}{\partial x} + g\rho\,.\tag{33}$$

Here P is the gas pressure, ρ is the gas density, and g is the gravitational acceleration. If we now consider a region of the MC/GMC with a uniform gas, a uniform density ρ_0, a uniform pressure P_0, and no bulk velocity $u_0 = 0$, we can define small perturbations of the form of

$$\rho(x,t) = \rho_0 + \rho_1(x,t)\,,\tag{34}$$

$$u(x,t) = u_1(x,t)\,,\tag{35}$$

$$P(x,t) = P_0 + P_1(x,t)\,.\tag{36}$$

Inserting equation 34 to 36 into equation 31 and 33 gives us the linearized mass continuity equation

$$\frac{\partial \rho_1}{\partial t} + \rho_0\frac{\partial u_1}{\partial x} = 0\,,\tag{37}$$

and the linearized momentum equation

$$\rho_0\frac{\partial u_1}{\partial t} + \frac{\partial P_1}{\partial x} = g_1\rho_0\,.\tag{38}$$

The gravitational acceleration from the density perturbation $\rho_1(x,t)$ is given by $\frac{\partial g_1}{\partial t} = -4\pi G\rho_1$. If we assume that the pressure is a function of only the density ρ, we can rewrite equation 38 into

$$\rho_0 \frac{\partial u_1}{\partial t} + \left(\frac{dP}{d\rho} \right) \frac{\partial \rho_1}{\partial x} = g_1 \rho_0 \,. \tag{39}$$

Now we can take the time derivative of equation 37, then take the spacial derivative of equation 39, and subtract the two. This gives us a wave equation

$$\frac{\partial^2 \rho_1}{\partial t^2} - \left(\frac{dP}{d\rho} \right) \frac{\partial^2 \rho_1}{\partial x^2} = 4\pi G \rho_0 \rho_1 \,, \tag{40}$$

defining the movements in a fluid consisting of gas, with a wave propagation speed given by

$$c_s \equiv \left(\frac{dP}{d\rho} \right)^{1/2} \,. \tag{41}$$

The movements are seen as perturbations, also known as sound waves, as the pressure moves through the fluid at the speed of sound c_s. Looking at a polytrope, the speed of sound is given by

$$c_s \equiv \left(\frac{\gamma P_0}{\rho_0} \right)^{1/2} = \left(\frac{\gamma k}{\bar{m}} T_0 \right)^{1/2} \,, \tag{42}$$

with γ being the adiabatic index, $\bar{m}$ is the mean mass per gas particle, the gas density is ρ_0, and the gas pressure is P_0. In an environment without self-gravity, where the waves would propagate stably with constant amplitude, and a sinusoidal density perturbation, given by $\rho_1(x,t) \propto e^{i(\omega t - kx)}$, we can get the dispersion relation by inserting this density perturbation into equation 40. This dispersion relation is given by

$$\omega^2 = k^2 c_0^2 - 4\pi G \rho_0 \,, \tag{43}$$

where c_0 is the sound speed in the unperturbed gas. This wave will propagate stably as long as the wavenumber is larger than the Jeans wavenumber $k > k_J$, which is given by

$$k_J \equiv 2\sqrt{\pi} \frac{\sqrt{G\rho_0}}{c_0} \,. \tag{44}$$

When $k < k_J$ the frequency ω is imaginary and self-gravity will make the amplitude of the perturbations grows exponentially. All wavelengths larger than the Jeans wavelength will make the wave unstable to gravitational collapse. The Jeans wavelength is given by

$$\lambda_J \equiv \frac{2\pi}{k_J} = \sqrt{\pi} \frac{c_0}{\sqrt{G\rho_0}} \,. \tag{45}$$

If the wavelength of the waves is shorter than the mean free path between gas particle collisions, the sound wave is unable to propagate. Entering the typical values we have been using so far, a sound speed of 0.18 km/s and a gas density of $4.8 \cdot 10^{-21} gcm^{-3}$, we get a Jeans' length of order $5pc$, and since in practice the gas velocity is even larger (by the Mach number), we can conclude that self-gravity is unimportant on average under our conditions. As can be seen from equation 45 it could become important at sub-pc scales only at gas densities hundreds to thousands of times larger than the average densities we are using. As discussed in the next subsection, turbulence can create densities large enough for self-gravity to become important, but the resolution of my experiments is not large enough to capture that, and therefore self-gravity can be neglected [31].

2.4   Turbulence inside the ISM

A very important property of MCs/GMCs in the ISM is turbulence. It is due to turbulence that we have a diffusion of gas and dust and a dissipation of kinetic energy inside of MCs/GMCs. It is also due to turbulence that overly dense regions form, where stars and planet formation happens [32]. Turbulence consist of irregular motions. In a turbulent flow, the fluid velocity $\vec{u}(\vec{x}, t)$ at a fixed point $\vec{x}$ varies in time almost randomly. The same is true for the velocity of the fluid in a turbulent flow at a fixed time t. Turbulent flow is a chaotic process that we need to examine statistically [31]. Interstellar turbulence has been shown to be supersonic, and needs to be driven by an external force in order for it not to die out in a crossing time [32] [33]. The crossing time is given by: $\tau_c = R/\bar{v}$ [34]. This driving could be sourced by stellar feedback, gravitation, magneto-rotational instability, cloud–cloud collisions, or other processes affecting the ISM, such as supernova explosions. There are two different kinds of turbulence inside MCs/GMCs, namely solenoidal turbulence, which is divergence-free, or compressive turbulence which is curl-free. Both are present in all clouds, and while the compressive part is the only one that can create overdensities directly, supersonic solenoidal motions are also important, since non-linear effects (inertia) tend to turn them into compressional motions. If we create a density probability distribution function (PDF) of an isothermal turbulent gas, we would find it to have the shape of a log-normal. The Mach number and the driving parameter can be used to determine the width of the PDF, and this parameter can also quantify the turbulent stirring. The driving parameter can move between the limits of 1/3 for purely solenoidal driving and 1 which is entirely compressive driving. If we have a purely compressive driving we will see a broader density PDF and a larger fraction of gas will be at high densities, and if we have solenoidal driving we will see smaller widths of the resulting PDF [32].

If we first look at homogeneous and isotropic turbulence, which thus can be seen as incompressible, we can define the maximum length an eddy can have, also called the correlation length. This is given by

$$\Lambda_T \equiv \frac{1}{\langle |u^{\vec{T}}|^2 \rangle} \int_0^\infty R(r)\, dr \,, \tag{46}$$

where $\langle |u^{\vec{T}}|^2 \rangle$ is the average squared turbulent velocity, and $R(r)$ is the velocity correlation function of the distance between two points r. Inside a turbulent flow, we will usually see a lot of different structures with different sizes, and it is, therefore, convenient to Fourier transform the turbulent velocity field, as

$$\vec{u}_{\vec{k}}^T = \frac{1}{(2\pi)^3} \int \vec{u}^T(\vec{r}) e^{i\vec{k}\vec{r}}\, d^3 r \,, \tag{47}$$

here k is the wavenumber ($k = 2\pi\nu$). From equation 47 we can now look at the different Fourier modes for different wavenumbers k. Next we can define three properties, namely the energy spectrum of the turbulent flow

$$E(k) = 2\pi k^2 \frac{1}{(2\pi)^3} \int R(r) e^{-i\vec{k}\cdot\vec{r}} d^3 r \,, \tag{48}$$

the specific turbulent kinetic energy

$$\epsilon_T = \frac{1}{2}\langle |\vec{u}^T|^2 \rangle = \int_0^\infty E(k)\, dk \,, \tag{49}$$

and if we assume a Newtonian fluid with constant kinematic viscosity, the rate at which the turbulent kinetic energy is dissipated

$$\psi_d = 2\nu \int_0^\infty k^2 E(k)\, dk\,. \tag{50}$$

Here ν is the viscosity, which in equation 50 is assumed to be the constant kinematic viscosity of a Newtonian fluid. From equation 50 we can see that the dissipation is weighted to high wavenumbers so that the smallest eddies present dissipates the turbulent energy through viscous heating. In order for the turbulent flow to remain in a steady-state, there must be an income of turbulent kinetic energy at the large scales at the same rate as energy is dissipated at small scales ψ_d. If this is not the case, the turbulence will die out. According to Kolmogorov, turbulent velocity fields of incompressible fluids need to be self-similar over a range of length scales. Combining the dimensions of the energy dissipation ψ_d ($L^2 T^{-}3$) and the viscosity ν ($L^2 T^{-}1$), we can get the length scale

$$l_K = \left(\frac{\nu^3}{\psi_d}\right)^{\frac{1}{4}}\,, \tag{51}$$

which is called the Kolmogorov length scale. This length scale defines, roughly, the size of the smallest features in the fluid, since structures smaller than the Kolmogorov length scale will dissipate their kinetic energy by viscous heating, and thereby disappear in less than one dynamical time. Next, we can define the velocity at the Kolmogorov scale, given by

$$u_K = (\nu \psi_d)^{\frac{1}{4}}\,, \tag{52}$$

and we can define the time it takes for a structure of that size to dissipate its energy away, which is given by

$$t_K = \frac{l_K}{u_K} = \left(\frac{\nu}{\psi_d}\right)^{\frac{1}{2}}\,. \tag{53}$$

Kolmogorov assumed an energy spectrum for self-similar turbulence, with power on all length scales from the smallest l_K to the largest Λ_K, in the form of

$$E(k) = u_K^2 l_K E_*(l_K k)\,, \tag{54}$$

where $E_*(l_K k)$ is a dimensionless function of the dimensionless wavenumber $l_K k$, and $u_K^2 l_K$ that gives the energy spectrum the right dimensions. Now we assume to be at a wavenumber in the range $\Lambda_T^{-1} \ll k \ll l_K^{-1}$, where negligible dissipation occurs, and the dominant energy process is the transfer of kinetic energy from large structures to smaller structures by inertial forces. Here the viscous force also is negligible, and the energy spectrum $E(k)$ thus is independent of ν, and we have $u_K = \nu^{1/4}\psi_d^{1/4}$ and $l_K = \nu^{3/4}\psi_d^{-1/4}$. With all of the just mentioned conditions in mind, the energy spectrum of the Kolmogorov spectrum can then be defined as

$$E(k) = \alpha \psi_d^{2/3} k^{-5/3} \sim \psi_d^{2/3} l^{5/3}\,, \tag{55}$$

where α is a dimensionless factor of order unity, and l is the radius of the eddies. Now we can define the typical velocity of structures with size l as

$$u(l) \sim u_K \left(\frac{l}{l_K}\right)^{\frac{1}{3}}\,, \tag{56}$$

and the Reynolds number for scales larger than the smallest eddies l_K as

$$Re = \frac{ul}{\nu} \propto l^{4/3}\,. \tag{57}$$

This means that viscous dissipation occurs on the smallest length scales close to l_K. From observations, it has been found that the initial condition stating that MCs/GMCs were incompressible fluids with a Kolmogorov spectrum of turbulence, is incorrect. Most studies of MCs/GMCs give a slope steeper than $1/3$ for the relationship between σ and l, and we, therefore, need numerical simulations to adequately simulate the turbulence inside a MC/GMC [31].

3   The simulation code

3.1   An overview of the DISPATCH framework

The DISPATCH code is a high-performance numerical simulation framework, written in the object-oriented Fortran programming language. It works by updating a collection of patches in space-time, where it performs a semi-independent task-based solution to partial differential equations. These patches are further divided into smaller volumes called cells. The tasks can be a variety of different systems. They can, for instance, solve the partial differential equations of ideal magnetohydrodynamics (MHD), non-ideal MHD, or particle motion. In my experiments, I am using a dust particle motion solver in order to solve for the motion of dust particles in a MC/GMC, and a hydrodynamic-solver in order to solve for the motion of gas in the same MC/GMC. Two features that make the DISPATCH framework ideal to use are firstly that the time steps are determined as well as applied locally and secondly, its use of a simple load balancing algorithm, consisting essentially of over-subscribing the work that needs to be performed, by having many more tasks then there are arithmetic units (CPU "cores"). The local time stepping is important for the overall performance of the framework since it lessens the needed total number of updates, thereby reducing computing time. The load balancing algorithm reduces the local load and communication imbalance. In order to solve the partial differential equations needed to run the simulations in the code, the DISPATCH code imports already existing solvers, with an augmented performance resulting inside the DISPATCH framework. This augmentation of the performance comes from more efficient cache usage, vectorization, and local time stepping [35].

The Fortran language is structured through the definition of objects, which hold both data and methods to handle the data. The Fortran language makes use of an inheritance structure where we can define a base object, which has "child classes" automatically inheriting attributes and methods from their parent class. The inheritance structure can also have "grandchildren classes" of children classes that inherit the attributes and methods from their parent class, the class it is made from, and its "grandparent class", and so on. If we, for instance, make a geometry object, then inside this object we can have a rectangle-class, and a circle-class. These 2 will then be child-classes of the base geometry object. If we have defined the geometry object with an integer called colour, then the two child classes would also have access to the colour component. If we make a class under the rectangle class that is called square and give the rectangle class attributes of length and width, the square class will inherit the length and the width components, from its parent class rectangle, as well as the colour component from its grandparent object, the geometry class, which is the base object. [36] [37]. DISPATCH is built on two base classes of objects namely tasks and task lists. The tasks class hierarchy is made up of a task data type that holds information of the fundamental state of the experiment like task position, times, and time steps. The task data type also holds methods for acquiring a task ID and inquiring about status flags among others.

The base object task is extended into a child-object which holds mesh-based tasks called a patch data type, holding spatial properties, including size, resolution, number of guard zones, number of physical variables, and so on. The patch data type also includes methods for measur-

ing intersections between different patches in space and time, as well as methods for writing and reading snapshots. The generic properties and methods can be extended into mesh-based solver data types. These data types can specify the physical variables to be advanced, add methods to initialise, and advance the patch data forward in time. They can also specify any parameters specific to the solver in question. Lastly, we can extend the solver data type into experiment data types. The experiment data types hold experiment specific functionalities, such as initial and boundary conditions. The experiment data type is also used as a generic wrapper and can be accessed through the task list hierarchy, which will hide the solver and thereby make it possible to run the same experiment with different solvers.

The other class hierarchy, namely task lists have as base member a list node data type, which is defined as a node in a doubly-linked list. The pointers attributed to the nodes are pointers to the next and previous node, as well as a pointer directed at the head of a neighbour list, consisting of `nbor` nodes. An `nbor` generalizes neighbours beyond spatial proximity, thereby including tasks that are dependent on the current task, and tasks that the current task is dependent upon.

The list node data type is used to define a doubly-linked list of nodes and keeps track of its properties, as well as containing the methods necessary to manipulate linked lists. This includes appending, removing, and sorting nodes. Lastly, the list data type extends into a task list data type which includes methods that are specific to the execution of tasks and the handling of task relations. It is the task list data type that holds the update method, which is the key procedure in DISPATCH. The update method handles task selected for updating. Now, when we run a DISPATCH experiment what essentially happens is that we call the task list update procedure repeatedly until all tasks are finished [35]. To sum up, the code is structured so that every patch in the experiment that the user wants to explore, has an instance of the task hierarchy. The code creates `nbor` lists that are made up of `nbor` data types, which point at the node data type. This is the base data member of the task list hierarchy, and the task data type, being the base data member in the task data type. For a visualisation see figure 2.

In order to generate these task lists, DISPATCH uses a set of components. Each component creates a sub-set of tasks, organized in some systematic way. In my experiments, I have used a component that creates a cartesian grid of patches in 3D.

In order to understand how the DISPATCH code functions, we first explore the DISPATCH framework running an experiment from the point of view of a single task, as it goes through its steps cyclically, in the mesh-based experiment. We need to have our guard zone values up-to-date before a task can advance to the next time step. The guard zones are regions in the neighbouring patches, that we use in order to get the right results in the boundaries of the patch we are looking at. These guard zones need to be interpolated in time and space, due to the patches using local time-stepping, thereby not synchronized in time, and because they can have different resolutions. In order to interpolate in time, values of field variables, like density and momentum, are saved in each patch in a number of time slices using a circular buffer [35]. A circular buffer is a contiguous block of memory that acts like it has an arbitrary beginning and no end [38]. In order to make an interpolation in space (prolongation) DISPATCH uses conservative interpolation and averaging operators, the same is true for the reverse process (restriction) [35]. Conservative interpolation is important when discretizing the experiment to small patches since the conservative interpolation conserves physical quantities globally like the density of the experiment [39]. An averaging operator is also important when having a large mesh of patches since they find the average value between two points and can help make a smoother environment in the experiment, so we do not see unnatural transitions between the patches [40]. Next the `dispatcher` will move the current patch to a (time-sorted) 'ready queue', but only if it deter-
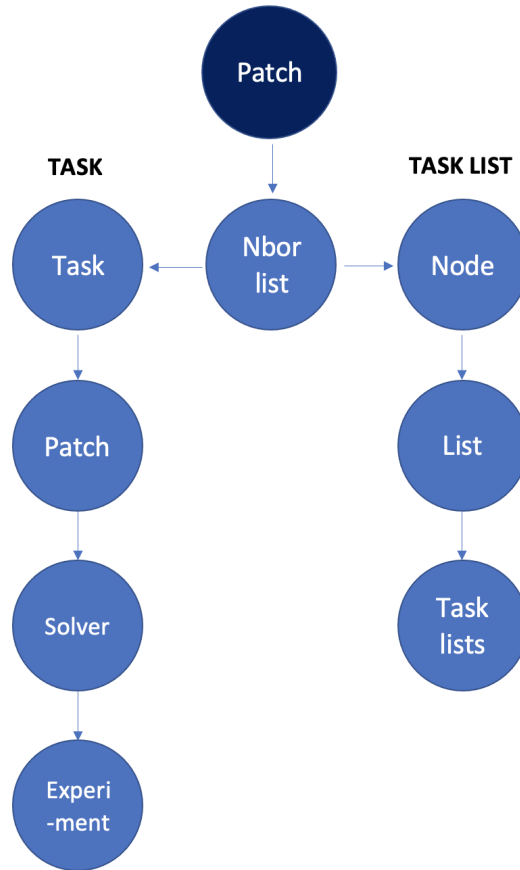
Figure 2: The experiment is divided into different patches so that we can solve equations for a part of the experiments at a time. Each patch holds an `nbor` list which points at the task list structure and the task structure. The `nbor` structure is, therefore, a list of how the different nodes in the patch are connected.

mines that the neighbouring patches have advanced sufficiently in time to supply guard zone values to the current patch. When the `dispatcher` selects a patch for updating it gives it a 'busy' state indication. Here both the internal values such as the mass or the density as well as the patch time is updated. After the update, the circular buffer will change the state of the patch back to 'not ready', since the guard zone values for the next time step are not yet available.

The `dispatcher` described above is the task scheduler of the framework. Looking at the DISPATCH framework process from the point of view of the `dispatcher`, it first selects tasks for updating and then later returns to evaluate the consequences of the updates on the tasks. As previously stated, what essentially happens when we run the DISPATCH framework is that it updates. The way that the update procedure operates is that each OpenMP thread uses it to pick the oldest task in the "ready queue", goes ahead to update it, while in the mean time another thread picks up the task that now had become the oldest one [35].

OpenMP is a mechanism common to Fortran and other compiled languages, which makes it possible for a number of "threads" to execute in parallel, using available CPU "cores". The code starts out on a single thread, but then branches out to a chosen number of threads, all executing the same code, thus making the code run faster. Since this keeps all cores busy, there is no need or benefit to obtain from parallelizing inside each task. After a task update is done, the code finds and queues any neighbouring patches ready to update because of the update of the current patch.

The problem with thread parallelism is that a large number of threads are doing the updating and nested locks at the same time, and thus the procedure is protected with OpenMP critical regions so that only one thread is allowed to operate with the 'ready to update' queue at one time. The way a task is defined as 'ready to update', is by examining the difference between the time of a task and its neighbours. If the condition

$$t_{self} \leq t_{nbor} + g\Delta t_{nbor} \tag{58}$$

is satisfied, where g is a grace parameter specifying the amount of extrapolation permitted relative to the neighbour time step, defined as Δt_{nbor}. Since the update does not happen instantaneously, this condition just needs to be true at some point, and not necessarily when the update happens. Now if we take the point of view of the input-output subsystem, we can explore how snapshots can be written to the disk for post-processing. When running an experiment in DISPATCH the parameter `task%out_next` is given, and the input/output view will, after the task has been updated, compare the task's current time in code units with this parameter. If it passes the `out_next` benchmark and it, thereby, is time for an output to be created, the task output method is called and a snapshot is written out. DISPATCH writes out the patch data as raw binary data to one file and patch information as text to another file.

The DISPATCH code has ported several well-used and well-documented astrophysical fluid solvers. These solvers have been tested using DISPATCH and different results have been replicated using these solvers inside the DISPATCH framework [35]. The one used in my experiments has been the HLLC from the public domain RAMSES code, which is a Godunov-type Riemann solver.

3.2   The fluid solver used: HLLC

The Euler equations are solved using their conservative form which is given by

$$\frac{\partial \rho}{\partial t} + \nabla \cdot (\rho \mathbf{u}) = 0 \,, \tag{59}$$

$$\frac{\partial}{\partial t}(\rho \mathbf{u}) + \nabla \cdot (\rho \mathbf{u}\mathbf{u}) + \nabla p = -\rho \nabla \phi \,, \tag{60}$$

$$\frac{\partial}{\partial t}(\rho e) + \nabla \cdot [\rho \mathbf{u}(e + p/\rho)] = -\rho \mathbf{u} \cdot \nabla \phi \,. \tag{61}$$

Here ρ is the mass density, u is the fluid velocity, e is the specific total energy, and p is the thermal pressure given by $p = (\gamma - 1)\rho(e - \frac{1}{2}u^2)$, where γ is the ideal gas gamma, and ϕ is the gravitational potential. In the experiments in this thesis $\gamma = 1$, and $\phi = 0$ [41]. What is meant by conservative form of the Euler equations is that they can be written on the form $U_t = +F(U)_x = 0$, where U_t is the vector of conserved variables and $F(U)$ is the vector of fluxes [42]. One of the main advantages of solving the Euler equations in conservative form is that no energy sink or source, to numerical errors, has an effect on the flow dynamics. In the above system of equations, gravity is also included as a non-stiff source term and thus the total energy is conserved at a percent level. Now we can write the Euler equations with gravitational source term as

$$\frac{U_i^{n+1} - U_i^n}{\Delta t} + \frac{F_{i+1/2}^{n+1/2} - F_{i-1/2}^{n+1/2}}{\Delta x} = S_i^{n+1/2} \,, \tag{62}$$

where U_i^n is the numerical approximation to the cell averaged value of $(\rho, \rho\mathbf{u}, \rho e)$ at time t^n and cell i. The code uses a Godunov method, also known as the Piecewise linear model or PLM, to calculate the time-centered fluxes [41]. As said by Van Leer, Godunov type methods are

non-oscillatory finite volume schemes that incorporates the solution to a Riemann initial value problem. The Godunov method uses the numerical values of U_i^n as cell averages of the analytical solution $U(x,t)$ at the time level n, which is expressed as

$$U_i^n = \frac{1}{\Delta x} \int_{x_{i-1/2}}^{x_{i+1/2}} U(x, n\Delta t)dx \,. \tag{63}$$

Now the fluxes will look like figure 3, and we therefore are left with Riemann problems at the cell boundaries. In a Godunov method scheme, the Riemann problem is solved locally [43].
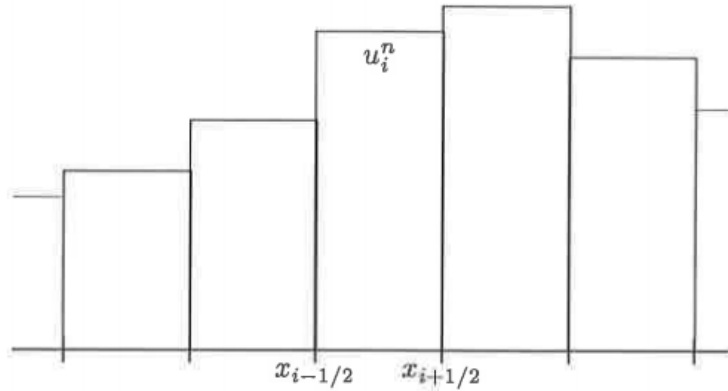

Figure 3: The solution to the Godunov method before the Riemann problem of the cell boundaries has been implemented [43]

.

In order to explain the Godunov solver in the RAMSES HLLC code we look at the solver at a single grid, which means solving equations 59 to 61. In order to do so, the code needs the correct boundary conditions, which consist of, looking at the hydrodynamical scheme, two ghost zones on each side and in each direction. The PLM scheme uses a Riemann solver with left and right states obtained by a characteristic tracing step, to compute second-order, time-centered fluxes at cell interfaces for a given time step [41]. A Riemann solver solves the problem that arises when you have solutions similar to figure 3, where the transition from cell to cell is not smooth. The most simple Riemann solver, developed by P. L. Roe, looks at the conservation laws we need to solve in a quasi-linear form: $u_t + A(u)u_x = 0$, with A_u being the Jacobian matrix $\frac{\partial f}{\partial u}$. This form of the equations are then linearized in each interval (x_{i-1}, x_i), replacing the Jacobian with interval-wise constant matrices $\tilde{A}(u_{i-1}, u_i)$. For any two adjacent states u_L and u_R, we need the interval-wise constant matrices to be diagonalisable with real eigenvalues $(\tilde{A}(u_L, u_R))$, we need $\tilde{A}(u_L, u_R) \leftarrow A(u)$ as $u_L, u_R \leftarrow u$, and we need $F(u_L) - F(u_R) = \tilde{A}(u_L, u_R)(u_L - u_R)$. We need these conditions to be fulfilled in order to gain hyperbolicity, consistency and conservation. The $\tilde{A}$ used, is an average of the Jacobian $\tilde{A}(u_L, u_R) = A(\bar{u})$. This average Jacobian $\tilde{A}$ is then diagonalised $(\tilde{X}\tilde{\Lambda}\tilde{X}^{-1})$, which gives a set of decoupled linear advection equations in the different intervals. We can decompose the flux differences in each interval onto the local eigenvalues as

$$\Delta f = f_R - f_L = \sum_{k=1}^{n} \tilde{\alpha}^k \tilde{\lambda}^k \tilde{x}^k \,, \tag{64}$$

with $\tilde{\alpha}$ being the coefficient for Δu, $\tilde{\lambda}$ being the eigenvalue, and $\tilde{x}$ being the eigenvector, corresponding to the kth characteristic field of $\tilde{A}$ [43].

In the RAMSES HLLC code the first thing that happens when running its Riemann solver is a standard characteristic analysis which is done by Taylor expanding the wave equations to second-order and projecting out the waves that cannot reach the interface within the time step. In order to ensure the monotonicity of the solution, a slope limiter is used to compute the slopes that enter into the Taylor expansion [41]. A slope limiter, limits the gradient when reconstructing a cell to the neighbouring centroid, so that it does not exceed the neighbouring cell average [44]. In the final step, we use the Godunov states to compute the fluxes of the conserved variables. The output of the single grid algorithm is in the form of fluxes across cell interfaces [41].

3.3   Parts of the DISPATCH framework used

DISPATCH was used by applying the `extras` module in the DISPATCH framework, where you are able to add extra modules, in order to include mechanisms of interest in the world of astro-physics, at a level between the basic patch and the layers of solvers. It is here the particles in the experiment are created. The extras module gets access to optional modules, like the one I am using for my experiments, being the `particles_solver_mod` responsible for the dust and gas interaction, explained in more detail later. In order for the extra module to create dust particles, a function called `init_conditions` is defined. This function first defines how many particles there will be present in the experiment, then it creates the particles. Another procedure, called `update`, is responsible for updating the particle positions.

The list of particles is made in the module `particles_mod`. In this module, the velocity of the gas, the gas density, and the dust density is imported. The time of the particle, which is needed in order to know at what time we are looking at the particle, is defined. A location mechanism is set up so that we can locate the particles, which works by looking at their index (what number cell are the particle in) defined by the parameter q, and by its position in that cell defined as r. When r is 1 it means that the particle has left that cell and thus the cell index will change. The particle properties are described by the attributes q r, v, and w. Here r is the position inside cell q, and v is the velocity in cells per time, and w is the weight of that particle. Next, the code creates the prerequisites for a list of particles to be created. It does so by creating a variable of type `particle_t`, which is a data type for a single particle. It makes the particles point at the next particle and the next particle and so on by a pointer called `next`. It also creates another pointer pointing at the previous particle and the previous and so on by the name `prev`. The list stops when the `next` variable points to a "zero pointer", called `null()`. This mechanism makes the list stop if it points at a `null()`. The procedure just described is the procedure that creates all particles. A small fraction of the particles are used to also keep track of the properties of the gas as they move along, using a `cell_t` data type.

Now we want to define a variable of type `particles_t`, being a data type for particle lists. Here we want to define the number of particles in the list, by first making the head and the tail of the list point at a `null()`, so that we have defined pointers showing that the list has come to an end for the first and last particle. Then we define a variable of type integer called n, which holds the number of particles in the experiment. Now we define an integer called `type`, which is defined to be 0 if the particle information is not printed, and 1 if the particle information is printed. We thereby only receive the information of the particles (like density and velocity) with `type` $= 1$, in the data file created at the end of the framework. Now we create a variable of type `real`, that holds the momentum of the experiment in order to make sure the total momentum is conserved. If we want to remove a particle from the list we just need to adjust the next or previous pointers, so that they skip a particle, and thereby points at the next next particle or the previous previous particle. The overstepped particle will then be written out of the list, but can still be included in another list corresponding to another cell. This is

useful when a particle e.g. leaves the cell it was in before we proceeded by a time step. This procedure is more expensive at the start and end of the list. This is why we are not interested in having real particles, that are crucial for the data in the experiment, in the beginning, and end of the lists. Therefore we create fake particles, that look like particles, but never need to be removed, at the start and end of the list holding particles for one cell. If we, for instance, want to look at 200 dust particles, the list will contain 202 dust particles, 200 real, and 2 unreal particles.

Next, we add various procedures that can calculate different quantities of the experiment, like the total momentum, density, velocity, and dispersion. These are calculated in the different functions inside the module. In order to calculate the velocity of the particles, the function `velocity` is created. This function starts by making the sum of the density and the velocity 0. Then it creates the pointer `p`, which points at the particles in the list and automatically skips the first and last particle when moving between the particles. We also define $p\%w$ as the weight of the particles, where the sum of all the weights is the mass density per unit volume of the particles. The function loops over the list of particles and calculates $sumd = sumd + p\%w$, so that $sumd$, in the end, is the summed density, and it also calculates $sumv = sumv + p\%w \cdot p\%v$, which calculates the sum of the weighted velocity. After the loop, $sumv$ is calculated as $sumv/sumd$ if $sumd$ is non zero. If $sumd$ is zero, $sumv$ is set to 0. This gives a weighted velocity normalized to the density of the dust particles, corresponding to the mean dust velocity. Then a dispersion function is made where the same procedure is performed as for the velocity, where the RMS dispersion is calculated by looping over the different particles in the list, making the calculation: $rms = rms + p\%w \cdot ((p\%v(1) - vav(1))^2 + (p\%v(2) - vav(2))^2 + (p\%v(3) - vav(3))^2)$. Here v is the velocity of a single particle and vav is the mean velocity (the same we calculated in the velocity function just with another name). After the loop we take the square root of the sum of the squares of the net velocity in all 3 dimensions, corresponding to the RMS dispersion.

The turbulence driving of the experiment is also added in the extras module, through two other modules called `forces_mod` and `force_mod` and is a purely solenoidal driven turbulence. In the `extras_mod` a `pre_update` procedure is called, before the Riemann solver. The forces created in the `forces_mod` and `force_mod` are extra terms in the prediction step and in the source update in the Riemann solver. To give a brief presentation of how turbulence is made inside the DISPATCH code, a force is calculated as a sum of all the different Fourier components of a random force created, that lies in the form of a cylindrical shell in k-space. Two time snapshots of forces are created and the turbulence module then interpolates softly between the two forces. This change in forces creates, after a short amount of time, a cascade that transports energy between large and small scales, and because the velocities are supersonic inertia creates compressive motions, even though the driving is solenoidal. With a high number of free parameters, this transport of energy creates turbulence in the experiment.

If we now go into detail with how the DISPATCH code creates turbulence, the inputs that you can give the turbulence (given in a file called `inputs.nml` file) is `ampl_turb` (amplitude of the turbulence), `k1` and `k2` (limits and slopes in k-space), `t_turn` (the turn over time), and `seed` (the random seed of the random force). The code then introduces variables needed to run the `force_mod` module, including `t_turb` which is set to $-1.5 \cdot$ `t_turb`. Then a do-while loop is started, running until `t_turb` $> time$, where time is the task time in code units (since `t_turb` is set to a negative value it works from a negative time up until the task time). The turbulence then works by introducing two random forces, in the form of a shell in k-space (where k is the wavenumber), and it continues to create new forces every `t_turb`. The first force is set equal to the force calculated in the last time step, and the new force is then calculated in the following code. When calculating the force it assumes that the density, pressure, and the sound speed inside the experiment is close to unity. The force is, therefore, a Fourier transformation of a

number of waves each with a wavenumber k, a phase that is randomly chosen, and an amplitude. The velocity amplitude of the force should be on the order of the input parameter `ampl_turb`, and the size scale of the driving motion should be on the order of $1/$`k1`. The turn over time of the turbulence is then calculated as `t_turn = t_turb · ampl_turb = 1/k1` and the acceleration is of the order `ampl_turb/t_turb`. The random force is created in a do-while loop, that loops over `t_turb`, that is interpolated with `t_turn` every loop (`t_turb = t_turb + t_turn`). It then creates a force snapshot and counts the number of wavenumbers the collected force has. It counts the number of wavenumbers by first defining a max wavenumber `kmax` defined as `k2 + 1`. Then a 3-dimensional loop is run from `-kmax` to `kmax` where the loop variables for the three do loops are given by jx, jy, and jz with an increment of unity. Then the number of wavenumbers are counted by creating the wavenumber: $fk = \sqrt{jx^2 + jy^2 + jz^2}$ inside the three do loops, and if the wavenumber is $fk <= k2 + 10^{-5}$ or $fk >= k1 - 10^{-5}$ (making sure it is inside the limits) it adds one to `nrand` which is the number of wavenumbers. Then it calculates the normalized acceleration factor of the turbulence with $accel = $ `ampl_turb/t_turn`$/\sqrt{float(\text{nrand})/8}$, normalized to the number of wavenumbers.

It is important for the turbulence to get a Kolmogorov slope of the driving alone, where the amplitude $a(k)$ drops with $k^{-11/6}$ and thus $a(k)^2 \cdot k^2 = k^{-5/3}$. The amplitudes of the Fourier modes need to be proportional to the driving. The module calculates the first part of the Fourier series namely the $e^{2i\pi n}$ part, where n is chosen to be a random number. The turbulence scheme will calculate a force inside a region of the experiment corresponding to the wavenumber k. This can make the region where this k is used, look like a bump in the density, and thus the Fourier mode is normalized with $k^{7/6}$ to avoid this effect. Then the compressive part of the velocity is subtracted from the Fourier mode to make sure it is divergence-free. Next the power spectrum of the energy is calculated from $fpow = fpow + fact \cdot (fxx^2 + fyy^2 + fzz^2)$, and is added to the existing power spectrum. Here $fact$ is a factor due to the amplitude of the wave in the Fourier series and can take the values 1, 0.5, 0.25, or 0.125, and fxx, fyy, and fzz is the Fourier modes in the x, y, and z-direction. Now the module loops over the different zones inside the cells, as well as the ghost zones of the cells, and calculates $a \cdot e^{ikr}$ where r is the position inside the cell of interest, and a is the amplitude/acceleration. Then the collected Fourier mode ($a \cdot e^{i2\pi kr}$) is added to the force, in all three dimensions. The force is then interpolated in time by first calculating a time $w = ($`t_turn`$ - ($`t_turb`$ - time))/$`t_turn`, where $time$ once again is the current time in seconds since 0:0:0, GMT, 1/1/70. Then a phase is calculated from the time just derived: $w = 0.5 \cdot (1 - cos(w \cdot \pi))$, that can be used to calculate the final force in the experiment $ff(:,:,:,:) = fran(:,:,:,:,1) + (fran(:,:,:,:,2) - fran(:,:,:,:,1)) \cdot w$, where $fran(:,:,:,:,1)$ is the old force and $fran(:,:,:,:,2)$ is the new force just calculated. The force it returns is thereby the difference between the new and old force added to the old force, which is returned to the `forces_mod`.

The `forces_mod` module works by taking the force calculated in the `force_mod` module and adding it to the patch being updated in the `pre_update` section in the `extras_mod module`.

Now let us look at the `particle_solver_mod` module in the DISPATCH framework, creating the interaction between dust and gas in the experiment. This file starts out by creating the module `particle_solver_mod`, which we use in the `extra_mod` file, calling all the functions created in the file. Now it defines all the lists and parameters needed to make a particle solver in a particle solver data type called `particle_solver_t`. This includes the `particle_t`, and `particles_t` data types. Also inside the `particle_solver_t` is information stored like gas density, dust density, and so on for the different cells in the experiment. Different integers used in the particle solver are then defined like the number of bins used, the random seed, the maximum particle size, and so on. The last thing happening inside the `particle_solver_mod`

function is the calculation of the total momentum, in order to make sure it is conserved. This is counted in the `mpi_counter` data type. Now the file goes on defining the subroutines inside the `particle_solver_mod` module. The first thing it does is to initialize the particle solver, then reading the parameters, and adding task links. This procedure collects the parameters we write in the `input.nml` file when running the experiment, and replaces the integers already defined like the number of bins and the particle sizes, with the integers in the `input.nml` file. Then the drag coefficient is calculated, which is a pre-factor for the drag force. This is calculated by looking at the density in cgs units for 1 year for a $1cm$ particle converted to code units by multiplying with the density scaling and dividing by the value of one year in code units. The procedure then transforms the scaling to code units, converting dust particle size and mass to cgs units. Then the patches are made, with the number of patches being dependent on the user input of the number of bins. Next, the solver solves the partial differential equations of the dust and gas movement, where the gas velocities are allocated and stored dynamically in an array having the form of the number of particles per cell bin. Then the gas density is loaded in (since it is already calculated in the module) as a variable.

Next, the module loops through the different cells in the experiment and calculates r (i.e. the position of the particles inside their cell) and finds the particles that need to go to another patch, (i.e. they have traveled from one patch to another). Then it goes through the export lists and exports the particles that need to be exported. Next, it loops through the bins and the cells. Inside the loop a pointer is pointing to the particles within the cell, and the number of particles within the cell is counted. If there are too few particles inside the cell, in order for them to represent the dust well in a statistical sense, the module adds particles to the cell and renormalizes the weights. The module makes a warning and adds particles to the cell that has too few particles. The module then checks if any cell has too many particles, which will cost too much memory to run. If this is the case it removes particles from that cell and renormalizes. After this loop, it loops over the different bins and recalculates the properties of the particles after the time step. Then inside this loop, it loops over the particles inside the bins and calculates the friction between the gas and the dust. If we have a non-supersonic environment the friction is defined to be the density multiplied with the drag coefficient divided by the size of the particle, which is constant. But we are in a supersonic environment, therefore the module subtracts the dust velocity from the gas velocity in the three dimensions. Then it finds the supersonic Epstein constant by

$$ pc = pc0 \cdot \sqrt{1 + \left(\frac{dv(1)^2 + dv(2)^2 + dv(3)^2}{cs^2} \right)}, \tag{65} $$

where $pc0$ is the constant mentioned when we talked about the subsonic environment (i.e. the density multiplied with the drag coefficient divided by the size of the particle), $dv(1-3)$ is the difference in gas and dust velocity for the three different dimensions, and cs is the speed of sound. Lastly the drag force is calculated in each direction individually by multiplying pc (the result from equation 65) with the difference between the gas velocity and dust velocity in each dimension. If the friction is very large ($pc \rightarrow \infty$), we need a mechanism in the module to handle it. This can happen when the dust to gas ratio are extreme, and causes a backreaction. Based on a forward-centering of the equation of motion, the code uses an expression for the updated particle velocity that goes asymptotically to the gas velocity, as it should in this case, while for smaller values of the friction it goes to the Epstein expression limit [35]. If this happens the module sets the dust particle velocity equal to the gas velocity. Finally, the procedure updates all the particles and the time.

4   Results

4.1   Outputs produced by experiments

4.1.1   Setup

In order to understand the dynamics of dust inside MCs/GMCs I started by exploring the behavior of gas and dust inside the confinements of an experiment, when changing the size of the dust particles present in the experiment. In this experiment, the dust and gas behave like a fluid and their motions are found by solving the Euler's equations of the experiment in the HLLC hydrodynamic solver. I chose the experiment size to be $1^3 pc^3$, the number density to be $1200 cm^{-3}/pc$ (the number density of the experiment is calculated as $1200 cm^{-3}/L$), the velocity unit to be set to $1 km/s$, the temperature to be set to $10K$, corresponding to a speed of sound of $0.18 km/s$, and the mean molecular weight of the gas to be 2.4, which corresponds to the mass of molecular hydrogen, helium, and a small fraction of metals. In the DISPATCH code, length scales are calculated in code units that are $1pc$ i.e. $3.086 \cdot 10^{18} cm$. The time in code units of the experiment is calculated for a $1^3 pc^3$ experiment as

$$t_{code\_1pc} = \frac{l}{u} = \frac{3.086 \cdot 10^{18} cm}{10^5 cm/s} = 3.086 \cdot 10^{13} s \approx 0.98 \cdot Myr \,, \tag{66}$$

where l is the length scale of the experiment, and u is the velocity scale of the experiment, which in my experiment is set to $10^5 cm/s$. The gas density of the experiment is calculated for a $1^3 pc^3$ experiment as

$$d_{code} = n_{H2} \cdot \mu = 1200 \; \frac{particles}{cm^3} \cdot 2.4 \cdot 1.6726219 \cdot 10^{-24} g = 4.8 \cdot 10^{-21} g/cm^3 \,, \tag{67}$$

where n_{H2} is the number density of the gas and μ is the molecular weight in cgs units. Thereby a density of 1 in code units corresponds to a density of $4.8 \cdot 10^{-21} g/cm^3$ in real units. The Courant factor of the system was set to 0.25 in order to have a stable system, and in order to suppress numerical oscillation, a slope limiter parameter value of 3 was chosen. The amplitude of the turbulence (`ampl_turb`), driving the turbulent force cascades in the experiment, was set to 0.45. In my experiments, I used 48 parallel threads when using OpenMP in the `dispatcher`. In my fiducial experiments, which I will discuss in the following, dimensions consist of a $1^3 pc^3$ sized experiment with $8 \times 8 \times 8 = 512$ patches, and $32 \times 32 \times 32$ cells per patch. This results in a total resolution of $256 \times 256 \times 256$ cells in the experiment. The number of dust particles per bin was set to 10 so the entire experiment starts out with $10 \cdot 256 \times 256 \times 256 = 167,772,160$ dust particles. The experiment needs time before it reaches an equilibrium of motions where the dust and gas has reached its terminal velocity and we see a quasi-steady state through time. There is, therefore, no need to keep all of the data made by the experiment, we are only interested in data from a time where the gas in the experiment has a physical state (e.g. the probability density function is a log-normal), as seen in nature. The data we need to collect is how gas and dust moves from the time where the quasi-steady state is reached, and a couple of turn over times ahead. For a $1^3 pc^3$ experiment the turn over time is, in code units (using equation 9 and 1 combined), given by

$$t_{turn} = \frac{1pc}{2 \cdot 1.2 \cdot (1pc)^{0.38}} \approx 0.42 \,. \tag{68}$$

In order to find an appropriate time to start the collection of data in the experiment, we can look at how the v_{rms} behaves as a function of time, for the 6 different dust particle sizes as seen in figure 4.

In figure 4 we see that dust of the 6 different sizes are sped up from the added turbulence that drives its velocity until it reaches a somewhat constant plateau, where the dust starts moving
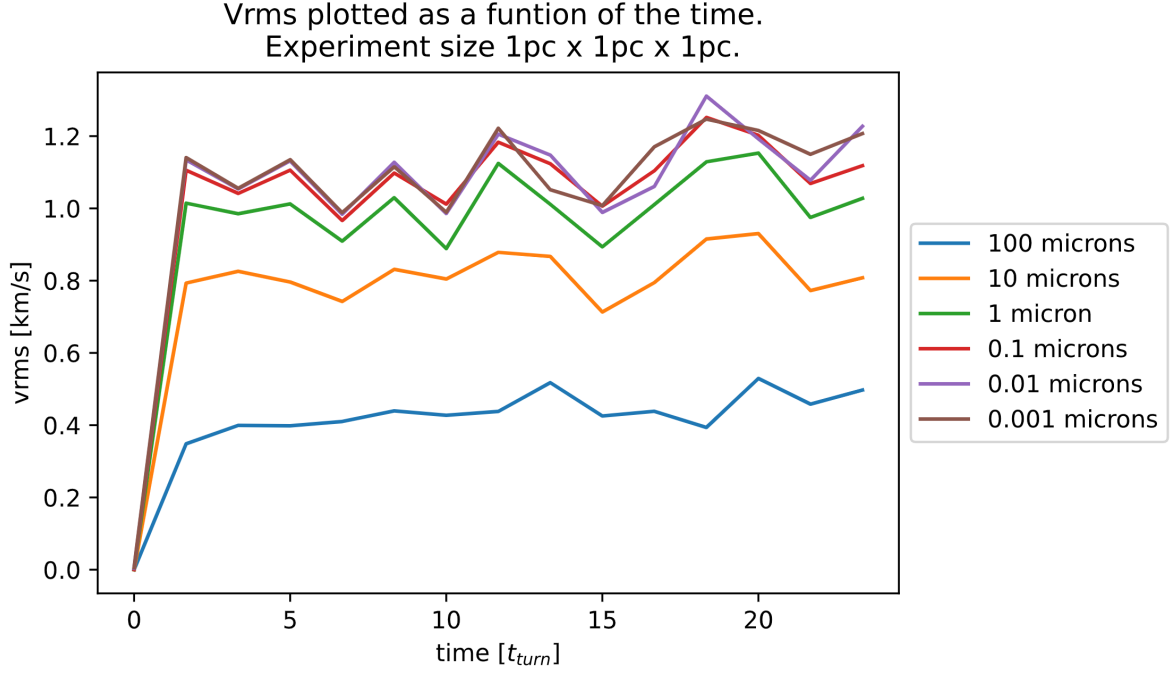
Figure 4: The v_{rms} as a function of time for the 6 different dust sizes between the times $t = 0$ t_{turn} and $t = 24$ t_{turn}, for an experiment of size $1^3 pc^3$.

like a physical MC/GMC. Thus we need to look at experiments after $t = 2.4$ t_{turn} in order to use data from when the particles have arrived at a proper v_{rms}, that imitate the movements of dust in a MC/GMC. I choose to start the experiment after 7 t_{turn}, and run for 7 t_{turn}. In order to get significant statistics in my experiment data I choose to have 40 snapshots of the time between the start- and end time which corresponds to an output every 0.24 t_{turn}.

The experiments were set as gravity, friction, and MHD free environments. I took the mean over 8 central cells in the z-axis in order to be able to explore the different parameters of interest for the gas and the dust in a 2-dimensional representation. First I wanted to explore how the density of the gas and the dust would behave when looking at a small range of dust sizes (diameter). The dust particle sizes I choose to explore were $0.001\mu m$, $0.01\mu m$, $0.1\mu m$, $1\mu m$, $10\mu m$, and $100\mu m$.

4.1.2   Outputs of a $1pc \times 1pc \times 1pc$ experiment

In order to get an understanding of how the dust and gas density behaves as we move between the 6 different dust particle sizes we can look at figure 5 and 6.

The way dust and gas can interact in these experiments is by coupling due to friction. Using the Stokes number (equation 11) to identify the level of coupling, we would expect dust to be more coupled to the gas when we are looking at smaller dust particles than when we look at larger dust particles. We would expect larger dust particles to behave more autonomous since the coupling to the gas will not be as effective for larger dust particles. The reason for the larger dust particles not being as coupled to the gas as the smaller particles is due to the larger dust particles having a longer dynamic time by equation 17, than the gas. Another way of looking at this, is that the large dust particles have a stopping length, from equation 8, that is longer than the length of the experiment, and will not be stopped inside the experiment. What this means is that when the large dust particles, affected by the coupling to the gas, change direction because of the gas changing direction, the gas will already have changed its direction again, since the
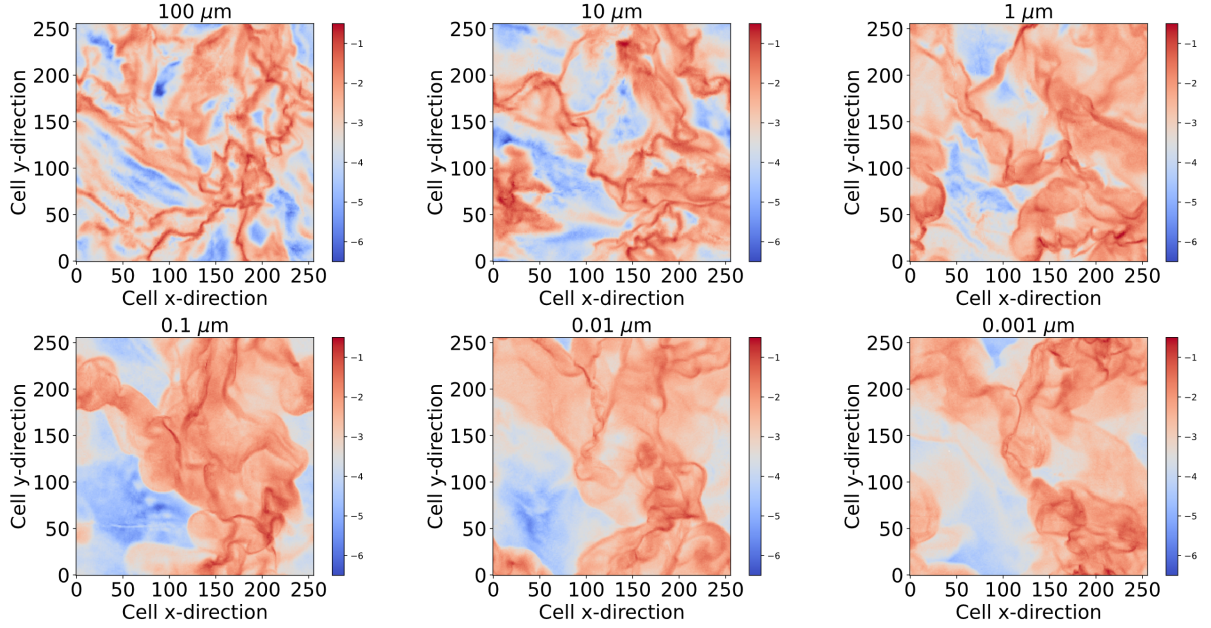
Figure 5: The 10-logarithm of the dust density of 6 different experiments of size $1pc \times 1pc \times 1pc$, after 14 turnover times. The colour here represents the 10-logarithm of the density summed over the mean of 8 cells in the z-direction, being the cells $60 - 67$ out of 256. The colour bar should be read so that a density of 1 corresponds to $4.8 \cdot 10^{-21} g/cm^3$ in real units. From the top to the bottom, from left to right we see the result for an experiment with the dust size being $100 \mu m$, then $10 \mu m$, and so on all the way down to $0.001 \mu m$. The x and y axes of the 6 plots are the cell counts, from 0 to 256.
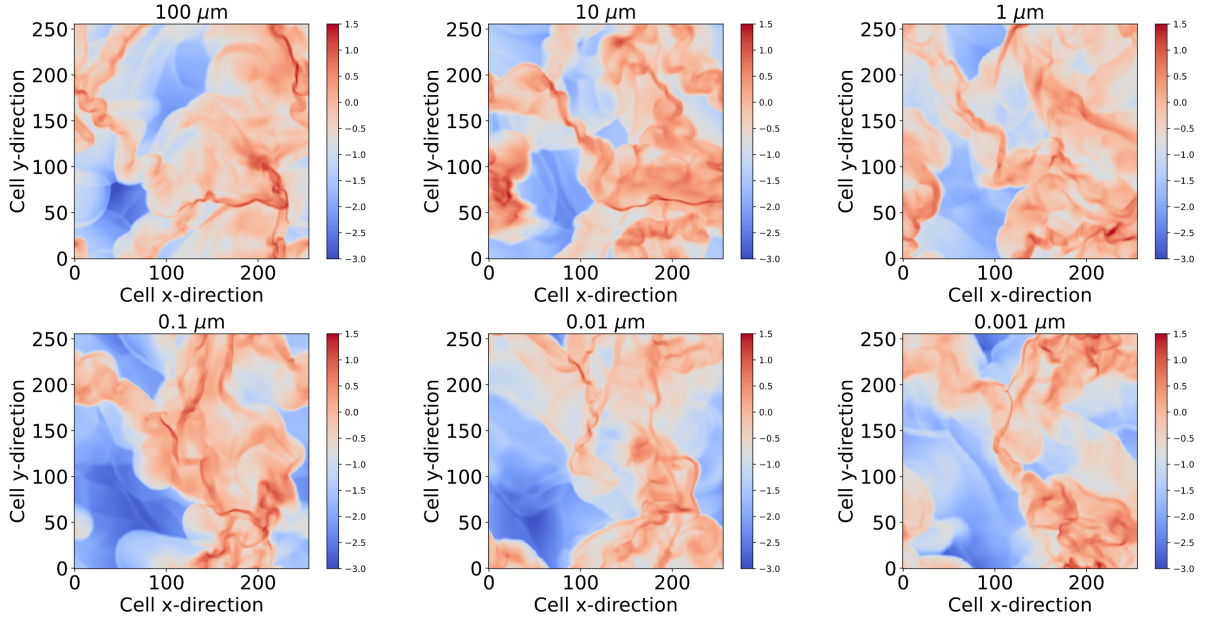

Figure 6: The 10-logarithm of the gas density of 6 different experiments of size $1^3 pc^3$, after 14 turnover times. The colour here represents the 10-logarithm of the density summed over the mean of 8 cells in the z-direction, being the cells $60 - 67$ out of 256. The colour bar should be read so that a density of 1 corresponds to $4.8 \cdot 10^{-21} g/cm^3$ in real units. From the top to the bottom, from left to right we see the result for an experiment with the dust size being $100 \mu m$, then $10 \mu m$, and so on all the way down to $0.001 \mu m$. The x and y axes of the 6 plots are the cell counts, from 0 to 256.

larger dust particles needs more time to change direction than the gas does.

If we look at figure 5 and 6, we see that the dust particles of smaller density are accumu-

lating in formations that replicate the structures of the gas accumulations accurately, inside and around the dense gas in the bulk. If we, for instance, look at the experiment with dust size $0.001\mu m$, the structure for the dust density is almost identical to the one for the gas density. We would expect the larger dust grains to be stopped by the large overdense gas structures, due to a large gas mass being accumulated in front of them, but this is not what we see happening. The larger the dust particles become, the less the dust density snapshot looks like the gas density one. If we compare the structure of the snapshot with a dust size of $100\mu m$ with the structure of the gas density, we see that the two have almost no similarity. If we look at the dust particles of size 1 and $10\mu m$, we see that they also start to have a different dust density distribution in the experiment, compared to the gas density. The main overdense structures are replicated for the dust, but there are structures in the dust density figure that are not to be seen in the gas density figure. Another thing to notice is that some dust density structures similar to the ones in the gas density are located in different regions of the experiments, indicating a delay in the coupling effect on the dust created by the gas, caused by the stopping time of the dust particles being longer than the dynamical time of the gas. This is a clear indication that the larger $100\mu m$ particles are mostly decoupled from the gas, but that the transition from being coupled to the gas to being mostly decoupled starts happening for dust particles of size $1\mu m$.

If the large dust particles were completely decoupled from the gas, we would expect to see the dust randomly distributed throughout the experiment, but this is not what we see when we look at the dust density of large dust particles. If we again look at the dust density of the $100\mu m$ dust particles, we see that there are indeed dust structures in the bulk, with a larger dust density than the rest of the experiment. These overdensities are created through the large dust particles being affected by the gas though friction, and are therefore still coupled to the gas by a small friction. The small effect of the friction will result in some effect on the dust particles, and after some time the small "puffs" due to friction by the gas will have caused the dust particles to form structures in the dust density. Taking a closer look at the dust density of the $100\mu m$ particles compared to the gas density in the same experiment, we see a large structure from $x = 100, y = 0$, to $x = 256, y = 200$ in both the dust and the gas density. This further confirms that there still exist a weak coupling between the dust and the gas, for large dust particles, which will be apparent after some time. What this shows us, is that all the different sized dust particles will, after a couple of turn over times, move around as groups of coherent dust through the GMC, due to the coupling to the gas. When two groups of dust cross path, an overdense dust region will form, seen in figure 5. For smaller dust particles, the coherent dust groups move with the gas, and therefore create the same overdensities as the gas. This shows us that an overdensity of dust will be formed for both large and small dust particles. For the smaller particles below $1\mu m$, the overdensities of dust will be formed in the same regions as the gas, and for large particles above $1\mu m$, the overdensities of dust will be formed both in the overdense gas regions but also outside of these overdense gas regions. The larger the dust particle, the more we see the overdense dust in filaments form outside the confinements of the gas overdensities.

We can also look at the dust to gas ratio, which will give us a clearer representation of the difference in coupling when looking at smaller and larger particles. This is illustrated in figure 7.

In figure 7 our picture of the larger dust particles being less coupled to the gas than the smaller dust particles is once again confirmed. The smaller dust particles have a much smaller dust to gas density ratio than the larger dust particles. For particles smaller than $1\mu m$, we see a predominantly constant dust to gas ratio over the entire experiment, deviating by having a larger dust to gas ratio in regions of extremely low gas density. This makes sense, since just a few dust particles inside a region of very low gas density will have a large impact on the dust to
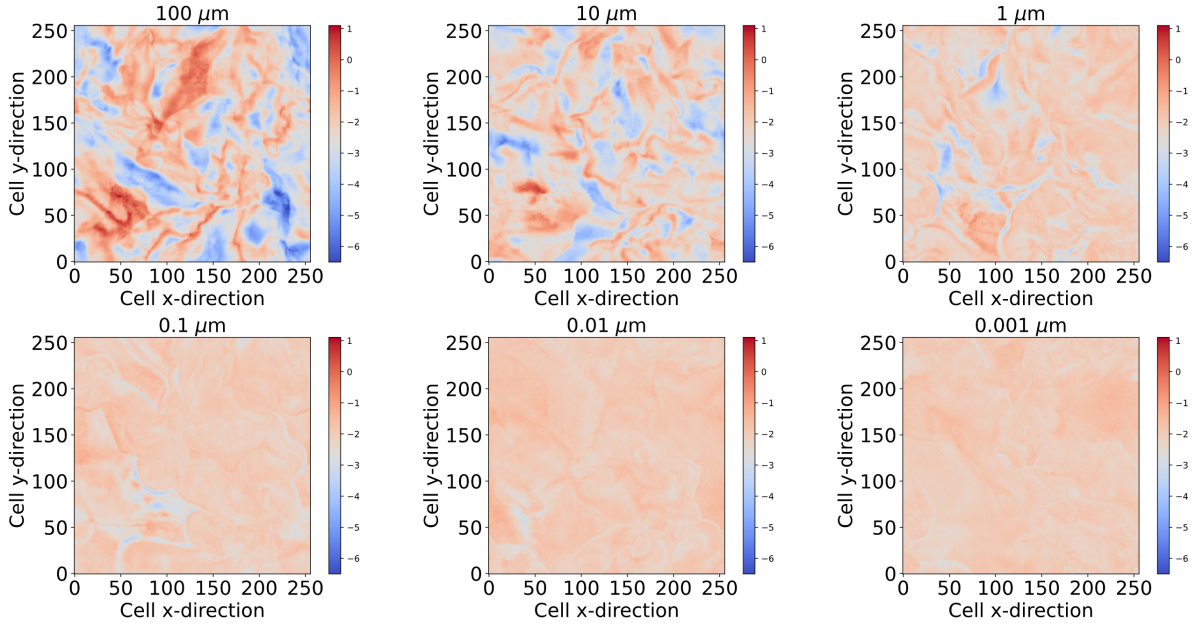
Figure 7: The 10-logarithm of the dust to gas ratio of 6 different experiments of size $1^3 pc^3$, after 14 turnover times. The colour here represents the 10-logarithm of the dust to gas ratio summed over the mean of 8 cells in the z-direction, being the cells $60 - 67$ out of 256, which is a mean of the dust ratio divided by the gas density. From the top to the bottom, from left to right we see the result for an experiment with the dust size being $100\mu m$, then $10\mu m$, and so on all the way down to $0.001\mu m$. The x and y axes of the 6 plots are the cell counts, from 0 to 256.

gas ratio. For the larger dust particles of size $1\mu m$ and larger, we see that the largest dust to gas ratios are present in regions where the dust density is large, due to the dust accumulating in different regions than the gas.

As a last way of exploring the coupling of dust to gas for different dust particle sizes, I looked at the actual Stokes number calculated from equation 11 for the same snapshots we have look at up until now. Looking at figure 8, shows us the same trend as we have seen so far with a larger Stokes numbers for the larger dust particles. In the experiment with $100\mu m$ particles, we see that the Stokes number is in the range $0.5 - 1000$, which means that there are some regions within the experiment which have a large decoupling from the gas, but there are still regions that have a Stokes number below 1, indicating that there still exists a locally significant coupling between the dust and gas. For smaller dust particles, such as the $0.001\mu m$ the Stokes number has a maximum value around 0.1, which means that dust particles of this size is largely coupled to the gas. We can also see a transition from the dust particles being largely coupled, with very small Stokes numbers for $0.001\mu m$ dust particles, to becoming largely uncoupled, starting for dust particles of size $1\mu m$. The regions in the experiment containing dust particles of size $0.1\mu m$, with low gas density have Stokes numbers between $1 - 10$, indicating that dust starts concentrating in regions outside of the overdense gas regions for these dust particles. For the experiment containing dust particles of size $10\mu m$, the Stokes number is roughly 1 throughout the entire experiment, having some regions with Stokes numbers above 1 and some below 1, indicating the transition between being largely coupled to being largely decoupled from the gas.

If we consider all of the results so far we can find the transition between where dust is completely coupled to the gas and where the dust is not mostly decoupled from the gas. Looking at figure 5 and 6 we see a transition happening between the $1\mu m$ and $100\mu m$ snapshots. In the $1\mu m$ snapshot, the main structures of the gas are still present in the dust snapshot, which means that the dust is still coupled to the gas, whereas in the $100\mu m$ snapshots, we see that
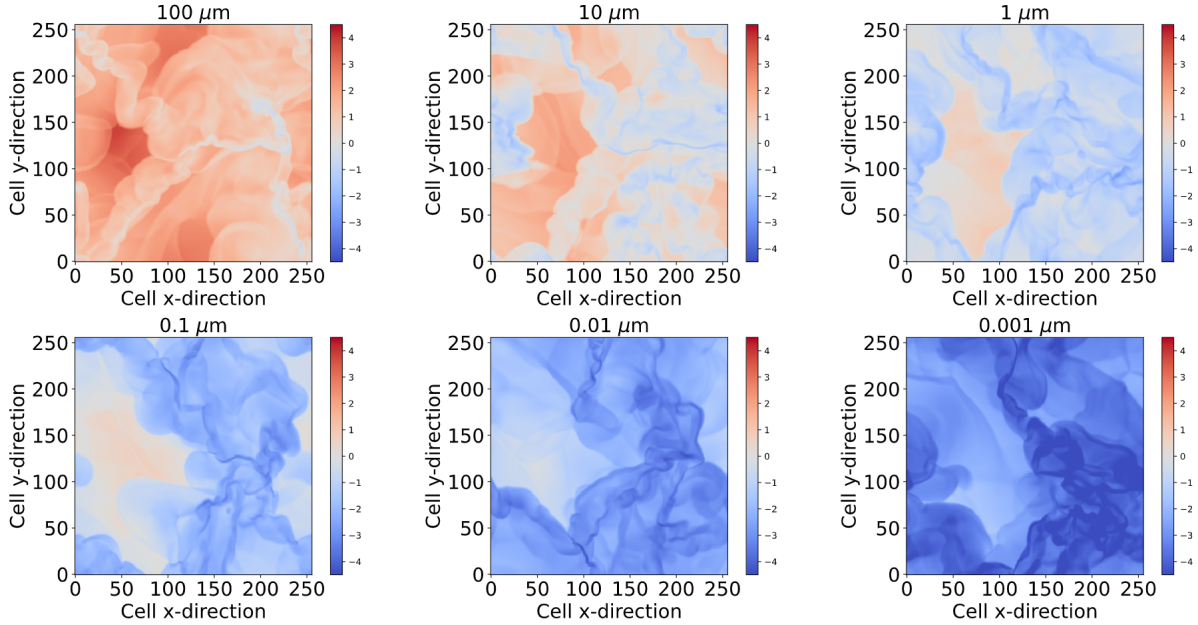
Figure 8: The 10-logarithm Stokes number of 6 different experiments of size 1^3pc^3, after 14 turnover times. The colour here represents the 10-logarithm Stokes number summed over the mean of 8 cells in the z-direction, being the cells $60 - 67$ out of 256, which is a mean of the Stokes number. From the top to the bottom, from left to right we see the result for an experiment with the dust size being $100\mu m$, then $10\mu m$, and so on all the way down to $0.001\mu m$. The x and y axes of the 6 plots are the cell counts, from 0 to 256.

the structures present in the gas density plot are not replicated in the dust density plot. The two plots have almost no similarity, and we can thereby conclude from these experiments that the dust is mostly uncoupled to the gas when the dust particles have a size between $1\mu m$ and $100\mu m$. This is also where we would expect to see a transition from our calculation in equation 16, where we found the dust size that would cause the dust particle to have a longer dynamical time than the stopping time of the particle inside the gas medium, should be about $50\mu m$.

In order to look at how dust concentrates in MCs/GMCs, consisting of gas and dust, I created 2D-histograms portraying the dust-to-gas ratio as a function of the dust and gas density. This made it possible to explore if the dust density is concentrated where the gas density is high, or if it is concentrated where the gas density is low. These figures can be seen in figure 9. From the figure portraying the dust to gas ratio as a function of the gas density, we see the 0.001, 0.01, and 0.1 gas density is centralized around a dust to gas ratio of 10^{-2}, and we see the dust to gas ratio taking on a wider range of values for all different gas densities starting from the $1\mu m$ plot continuing to the $100\mu m$ plot. If we observe the $100\mu m$, $10\mu m$, and to some extend the $1\mu m$ dust to gas ratio as a function of the gas density, we see that there exist a declining linear trend with a lower dust to gas ratio for larger gas densities and a larger dust to gas ratio at smaller gas densities. A linear relationship in the loglog space is equivalent to a power law relationship. This suggests that there is a significant amount of dust outside of the overdense gas regions. The spread of the different dust to gas ratios over a wide field of gas densities for the large particles is due to the dust being more present outside regions of high gas density, for the larger dust particles. This is also what we would expect from the previous discoveries of large dust particles not being as coupled to the gas as smaller dust particles. We can explain the smaller dust particles having its dust to gas ratio centralized around 10^{-2} for all gas densities, by the smaller dust particles being largely coupled to the gas, and therefore the dust to gas ratio will be the same in almost all regions of the experiment.
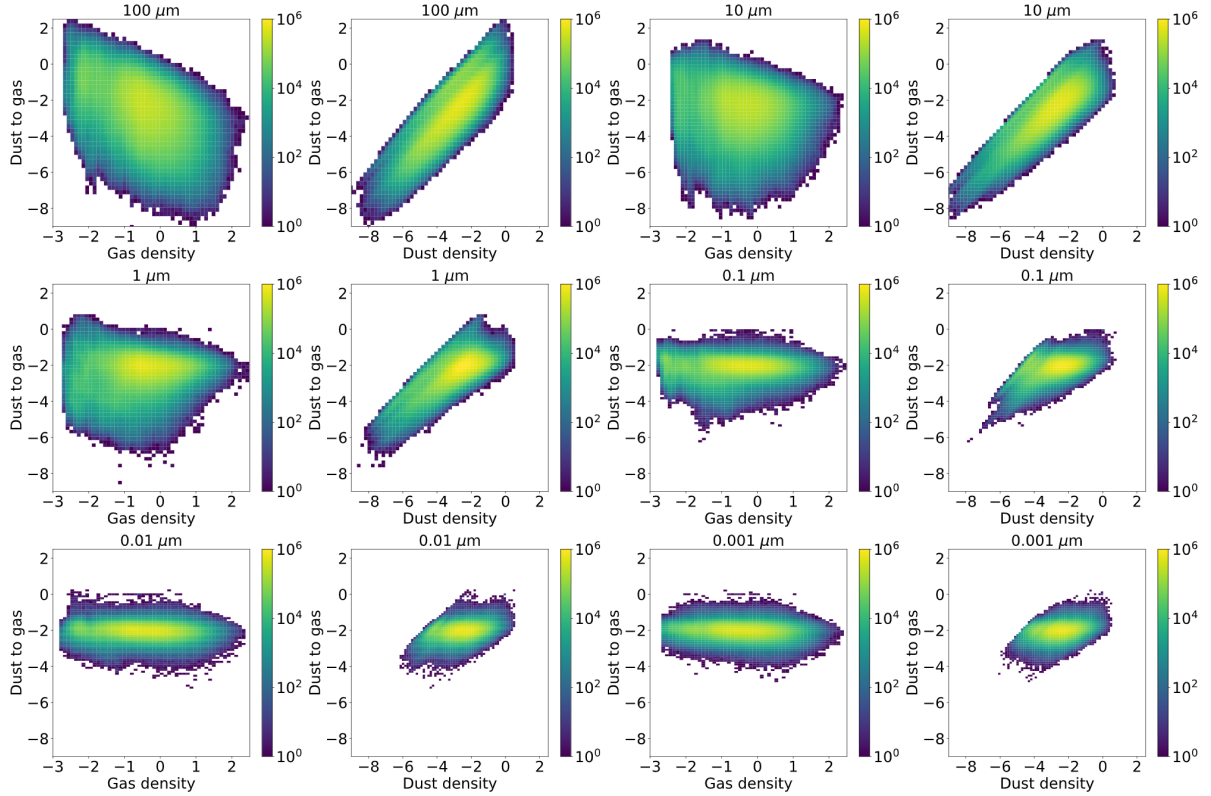
Figure 9: Dust-to-gas ratio as a function of the density of dust and of gas plotted in a double logarithmic 2d-histogram, made from an experiment of size $1^3 pc^3$, after 14 turnover times. The colour bar expresses the number of dust particles in the given regime of dust-to-gas ratio and gas/dust density. The figures are made for dust particles of size $0.001\mu m$, $0.01\mu m$, $0.1\mu m$, $1\mu m$, $10\mu m$, and $100\mu m$.

If we now look at the dust to gas ratio as a function of the dust density plots in figure 9, we see a linear relation in the double logarithmic regime for the larger dust particles of size $1\mu m$ to $100\mu m$, again meaning that a power relationship exists between the dust to gas ratio and the dust density for the larger dust particles. As we move down to smaller dust particle sizes, we see that this linear relationship is broken and we now have most of the dust in a dust density region around 10^{-3} and a dust to gas ratio of 10^{-2}. Looking at the larger dust particles almost linear relationship in these double logarithmic plots, we see that the dust density is smaller in regions with a low dust to gas ratio, and larger in high dust to gas regions. From the previous discoveries we know that the dust moves with its own velocity field with its own divergence and convergence, and now we can see that after some time there will, for large particles, be a exponential growth in the divergent regions. This suggests that dust is distributed in the gas structures for smaller dust particles, and for larger dust particles the dust will accumulate outside of the overdensities in the gas with time. There is thereby a larger probability of dust being concentrated in the gas structures for smaller dust particles than for the larger dust particles. The turning point of when the dust will be distributed more in its own overdensities is for a dust particle size of $1\mu m$ and larger.

Another important property I have chosen to look at is the v_{rms} of the dust and the gas in the experiments, which can be seen depicted at the same time as before $t = 14 \ t_{turn}$ and for the same size experiment $1^3 pc^3$, in figure 10 and 11. We can start by comparing the velocity of the dust in figure 11 with the dust density in figure 5. Doing this we see that where the dust density is largest the velocity dispersion is largest. This can be explained by the dust density being large where different groups of coherent dust overlap, and the dust v_{rms} values in these overlapping regions are therefore also large. We do see that even the largest dust velocity dispersion (v_{rms})
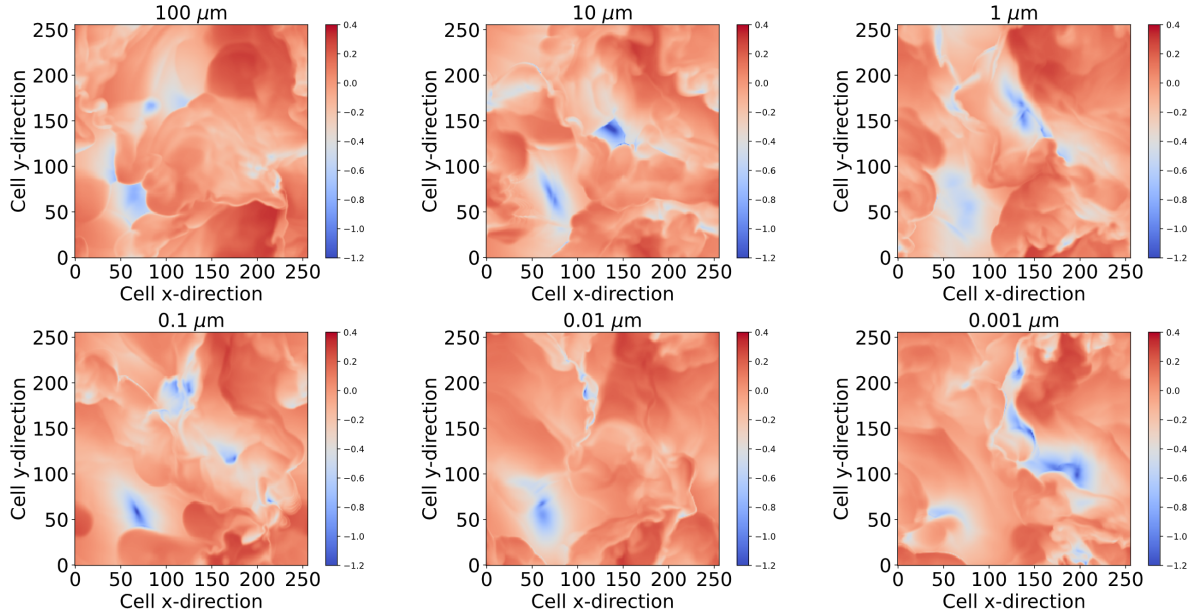
Figure 10: The 10-logarithm of the gas v_{rms} of 6 different experiments of size $1^3 pc^3$, after 14 turnover times. The colour here represents the 10-logarithm of the v_{rms} of the gas summed over the mean of 8 cells in the z-direction, being the cells $60 - 67$ out of 256. 1 in the colourbar corresponds to $1km/s$. From the top to the bottom, from left to right we see the result for an experiment with the dust size being $100\mu m$, then $10\mu m$, and so on all the way down to $0.001\mu m$. The x and y axes of the 6 plots are the cell counts, from 0 to 256.
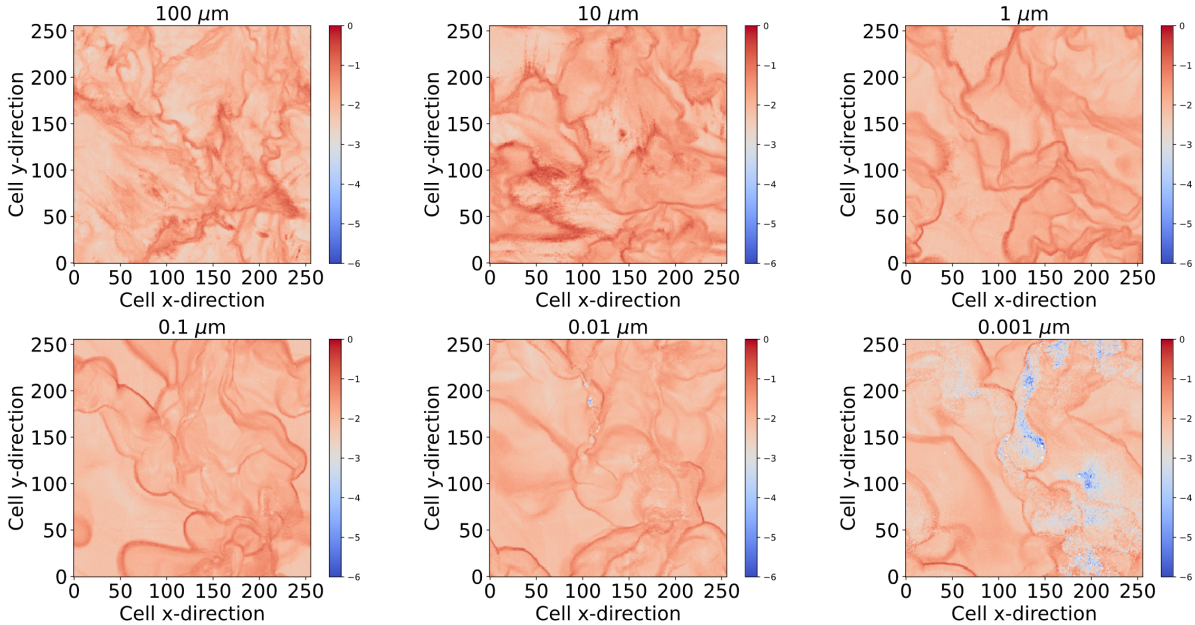

Figure 11: The 10-logarithm of the dust v_{rms} of 6 different experiments of size $1^3 pc^3$, after 14 turnover times. The colour here represents the 10-logarithm of the v_{rms} of the dust summed over the mean of 8 cells in the z-direction, being the cells $60 - 67$ out of 256. 1 in the colourbar corresponds to $1km/s$. From the top to the bottom, from left to right we see the result for an experiment with the dust size being $100\mu m$, then $10\mu m$, and so on all the way down to $0.001\mu m$. The x and y axes of the 6 plots are the cell counts, from 0 to 256.

is not very large, if we look at the colour bars of figure 11. This illustrates that even for the largest dust particles of $100\mu m$, the dust moves collectively, as a group. This illustrates that regions of large dust density are created by groups of coherent dust overlaps. If we now look at figure 10 and 6, we also see that where the gas density is largest the gas v_{rms} is largest. If we now compare all 4 plots (figure 11, 10, 5, and 6), we see that there is a displacement between

this mechanism for the dust and the gas, since the dust can not "keep up" with the gas, and reacts after the gas already changed its direction of movement. This is so because (as previously stated) the timescale of the dust to change direction is larger than that the gas. This throws the dust in many different directions, making more overdensities for the dust than for the gas.

4.1.3   Setup for experiments with different box sizes

In order to explore the difference in dynamics of dust particles of different sizes, when looking at different MCs/GMCs, I repeated the above experiment for experiments of sizes: $0.33^3 pc^3$, $3^3 pc^3$, $9^3 pc^3$, and $27^3 pc^3$, and compared these to each other. More specifically I wanted to explore the mean dust v_{rms} compared to the mean gas v_{rms}. I also ran the $1^3 pc^3$ experiment data with new parameters in line with what is explained as follows. In order to scale these experiments correctly we need to adjust the number density of the gas in accordance to $n_{H2} = 1200/l_{pc}$ in code units, and the density as in equation 67 with the correct number density according to the experiment size. All experiments had a resolution of 10^3 patches with 36^3 cells per patch and thus a resolution of 360^3, which was the maximum resolution, the DISPATCH framework could run without experiencing overuse of memory on a single standard computational node with 192GB of memory. The time was scaled in agreement with $\frac{L}{v_{vms}} = \frac{L}{1km/s}$, which is the way we calculate time in code units. To figure out where to begin the data collection for the different experiments of different sizes, we can once again assume that after 2.4 dynamical times is the best place to start for all the different experiment sizes. If we then choose to have 40 outputs from every experiment and if we want to run the experiments over 10 dynamical times, since it is enough data to do proper statistics without being too demanding on the storage, we can now calculate the different times to use in the experiments in code units, and scale them accordingly. For the $0.33^3 pc^3$ experiment we have a dynamical time of (from equation 17 and 1): $t_{dyn} = 0.33pc/ \left(2 \cdot 1.2pc^{-0.38}km/s \cdot (0.33pc)^{0.38}\right) = 0.21\frac{pc}{km/s}$, but in order to gain it in code units we need $t_{dyn} = \frac{L}{1km/s}$, which in our case is $t_{dyn} = 0.21\frac{pc}{km/s} = \frac{0.33pc}{1km/s} = 0.21\frac{pc}{km/s} \cdot \frac{1km/s}{0.33pc} = 0.63$. And therefore the start time for the $0.33^3 pc^3$ experiment will be $0.63 \cdot 2.4 = 1.5$, the end time will be $0.63 \cdot 10 + 1.5 = 7.8$, and the output time will be $\frac{0.63 \cdot 10}{40} = 0.16$. Performing the same calculations on on the experiment sizes we end up with times as seen in table 1.

Another property that needed updating when changing the size of the experiment is the amplitude of the turbulence and the turnover time which needs to be updated with respect to equation 9. The amplitude of the turbulence corresponding to the different experiment sizes was found by running experiments with different turbulence amplitudes and then calculating the average gas v_{rms} in the experiment, and comparing it to the expected v_{rms} found from the first Larson relation (equation 5). By trial and error, it was possible to find the turbulence amplitude that gave rise to the most correct Larson relation, in order for the experiment to represent a physical MC/GMC. The different amplitudes and turn over times can be found in table 2.

Experiment size	Dynamical time	Start time	End time	Out time
$0.33^3 pc^3$	0.63	1.5	7.8	0.16
$1^3 pc^3$	0.42	1	5.2	0.11
$3^3 pc^3$	0.27	0.65	3.35	0.07
$9^3 pc^3$	0.18	0.43	2.23	0.05
$27^3 pc^3$	0.12	0.29	1.49	0.03

Table 1: Table showing the times used for the experiments of different experiment sizes calculated in the same way as in the above example.

Experiment size	Mean v_{rms} in experiment	v_{rms} from first Larson relation	Turn over time	Turbulence amplitude
$0.33^3 pc^3$	0.67	0.66	0.63	0.23
$1^3 pc^3$	1.00	1	0.42	0.38
$3^3 pc^3$	1.51	1.52	0.27	0.78
$9^3 pc^3$	2.31	2.30	0.18	1.6
$27^3 pc^3$	3.50	3.50	0.12	2.88

Table 2: Table showing the turnover time and amplitude of the turbulence for the experiments of different sizes found from trial and error so that the average gas v_{rms} in the experiments corresponded to the ones found from the first Larson relation.

4.1.4   Investigating physical and numerical convergence

Specifically two limitations are important when looking at the v_{rms} of particles driven by simulated turbulence. The first limit is the limit associated with the turbulent cascade in the experiment. This limit is due to the acceleration per volume of the turbulence, that pushes all cells in the experiment, having a wavenumber so small that it drives the turbulence on large scales only. The drive of the acceleration is a sinus wave moving in space. If we look at an experiment of a fixed size, let us say $1^3 pc^3$, the dust v_{rms} of the experiment, looking at the whole experiment of $1^3 pc^3$, will be affected by the turbulent force. If we now look at an experiment of a larger size, e.g. an experiment of size $3^3 pc^3$, we could divide this experiment into 27 sub boxes of size $1^3 pc^3$. Then if we look at the v_{rms} of the sub boxes of this larger experiment, the effect of the turbulent force will be lessened since the sub boxes of the larger experiments turbulence will be driven through cascades of the turbulent force working on $1 pc$ scales. Looking at the sub boxes of an experiment instead of looking at the entire experiment is a more physical observation and will thereby represent what we see in MCs/GMCs better. The resolution of the $0.33^3 pc^3$ experiment is reduced to $120 \times 120 \times 120$ cells so that the resolution of the sub boxes of the $1^3 pc^3$ experiment has the same resolution as the $0.33^3 pc^3$ experiment. To reduce this effect even further we could look at the sub-sub boxes of an even larger experiment. In line with the examples given above, we could choose an experiment of size $9^3 pc^3$ and then divide this experiment into 729 sub-sub boxes of size $1^3 pc^3$. These sub-sub boxes should have an even smaller effect on the v_{rms} from the turbulent force. The result of these tests can be seen in figure 12. The resolution of these boxes should be $1080 \times 1080 \times 1080$ cells, but since MPI is not working with particles at the moment in the DISPATCH code, it was not possible to run experiments with that resolution, due to lack of memory when running such memory heavy experiments. Not having access to enough memory to run experiments with resolutions larger than 360^3 cells, has a large effect on, especially, sub-sub boxes of experiments, which will be explored later.

Looking at figure 12 we see that there is not a big difference in the v_{rms} between the sub-sub boxes and the sub boxes of the experiments. But there is a significant difference between the full $0.33^3 pc^3$ experiment and the sub and sub-sub box experiments of $33\% - 48\%$. This indicates that the turbulent force influence on the v_{rms} for the experiments as a whole has a significant effect, and should be seen as a limitation in the determination of the v_{rms} of the different experiment sizes.

In figure 13 we explore the effect of the same error as in figure 12, but for the v_{rms} of an experiment of size $1^3 pc^3$ compared to the sub boxes of size $1^3 pc^3$ of an experiment of size $3^3 pc^3$
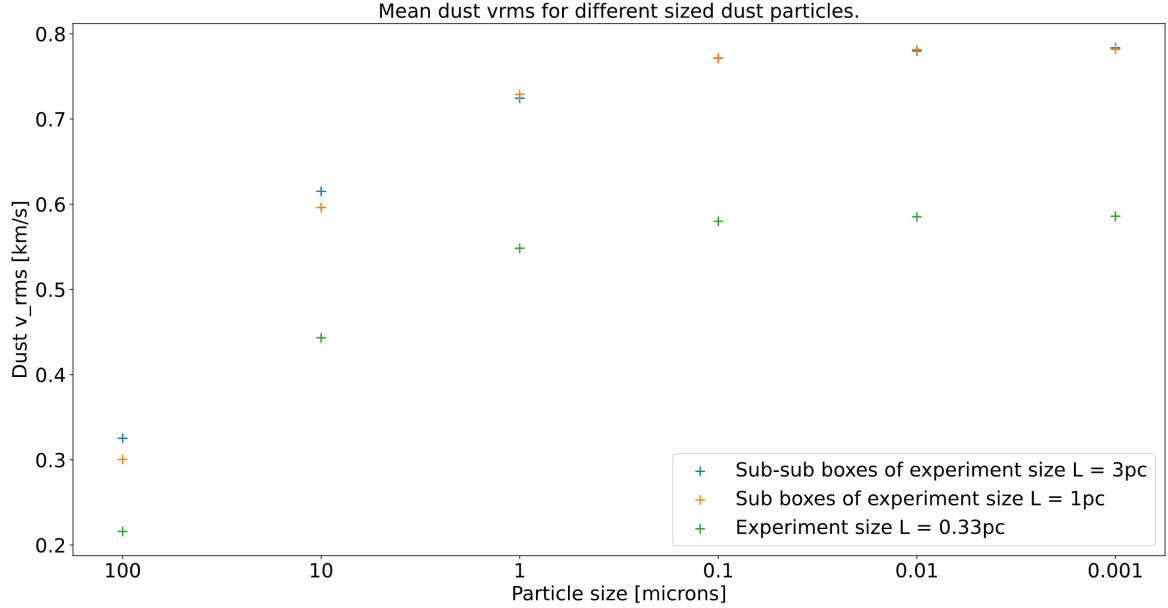
Figure 12: The mean dust v_{rms} plotted as a function of the dust size. Here the blue graph is the results for the $0.33^3 pc^3$ experiment, the orange graph is the mean over 27 sub boxes of size $0.33^3 pc^3$, derived from the $1^3 pc^3$ experiment, and the green graph is the mean over 729 sub-sub boxes of size $0.33^3 pc^3$, derived from the $3^3 pc^3$ experiment. The mean v_{rms} is found from the average over 40 snapshots between the times $t = 2.4\ t_{turn}$ to $t = 10\ t_{turn}$.

and the sub-sub boxes of size $1^3 pc^3$ for an experiment of size $9^3 pc^3$. Here we see that there is a larger difference between the sub boxes and the sub-sub boxes, but they still follow the same trend closely. We still see that there is a gap between the results of the 120^3 resolution experiments v_{rms}, and the v_{rms} of the sub boxes and sub-sub boxes. Here the sub and sub-sub boxes have a v_{rms} value of $34\% - 41\%$ above the v_{rms} of the 120^3 resolution experiment, which further confirms the need to look at this limitation.

The second limitation on the v_{rms} is due to the numerical diffusion being considerably larger for experiments with larger Mach number i.e. larger experiment sizes (seen from equation 4). When we look at the v_{rms} for different sub or sub-sub boxes inside an experiment instead of the v_{rms} at different dust sizes for the whole experiment of same size as the sub or sub-sub boxes, we will have a bulk motion of the dust particles for the sub and sub-sub boxes. This bulk motion of the dust particles is not present if we consider the v_{rms} over the entire experiment, since it encapsulates the experiment, and the gas, therefore, streams through it.

In figure 14 we see the mean dust v_{rms} as a function of the dust particle size for an experiment of size $0.33^3 pc^3$ and an average over the sub boxes of size $0.33^3 pc^3$ of an experiment of size $1^3 pc^3$, averaged over 5 experiments with different random seeds for the turbulence of the experiment, and also averaged over 40 snapshots between the times $t = 2.4\ t_{turn}$ to $t = 10\ t_{turn}$. This gives a better picture of how correct our dust v_{rms} to dust size correlations is. From the errorbars in the plot we can see that there is a significant spread in the values for the different mean dust v_{rms}, when we use different random seeds for the turbulence in the experiments. This means that there is a small limitation corresponding to what random seed you choose in the experiment, and therefore numerical diffusion limits the results of the experiments.

Since these two limitations are significant, it is safer to look at how the dust moves, normalized to the gas motion, and from these new results, explore how dust with different dust- and experiment sizes behaves in MCs/GMCs.
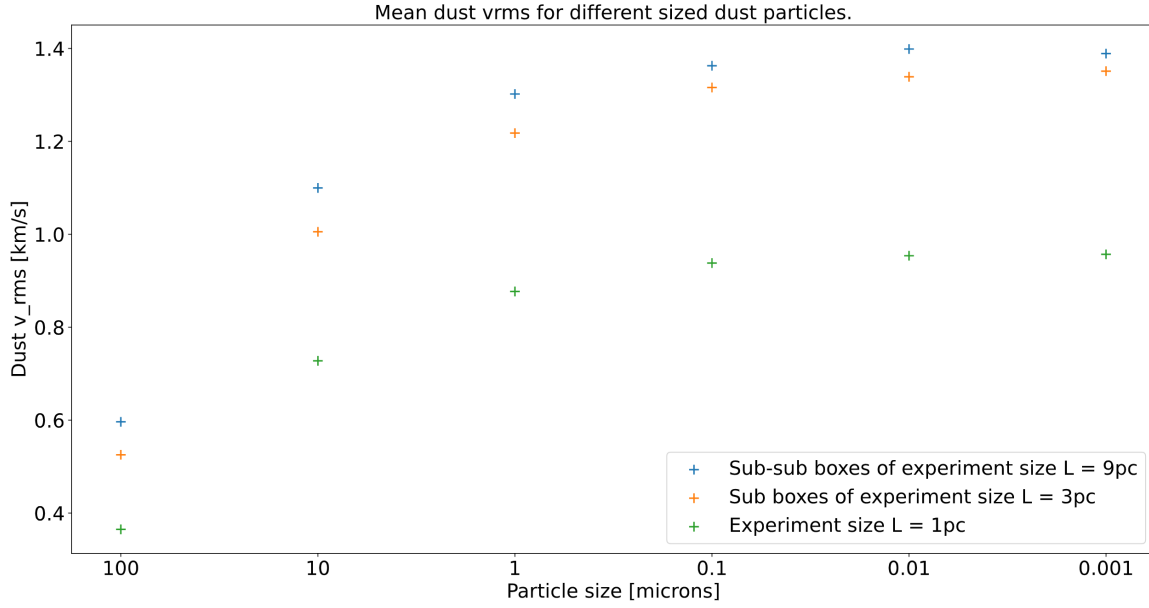
Figure 13: The mean dust v_{rms} plotted as a function of the dust size. Here the blue graph is the results for the 1^3pc^3 experiment, the orange graph is the mean over 27 sub boxes of size 1^3pc^3, derived from the 3^3pc^3 experiment, and the green graph is the mean over 729 sub-sub boxes of size 1^3pc^3, derived from the 9^3pc^3 experiment. The mean v_{rms} is found from the average over 40 snapshots between the times $t = 2.4\ t_{turn}$ to $t = 10\ t_{turn}$.
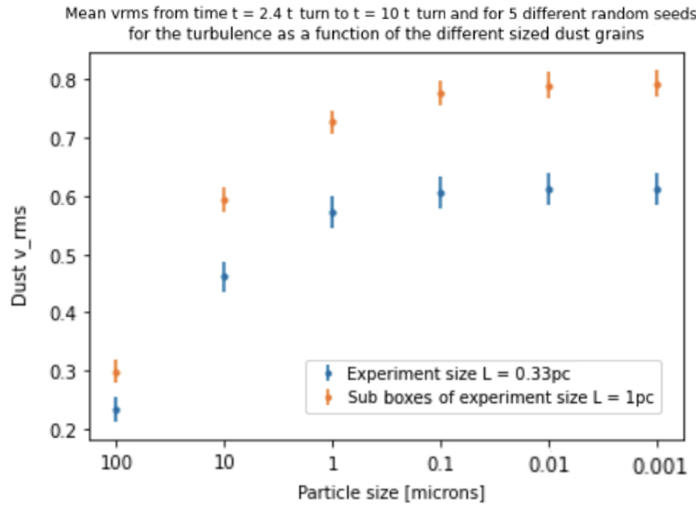

Figure 14: The blue figure is the mean dust v_{rms} for experiments with different dust particle sizes, and an experiment size of 0.33^3pc^3, averaged over 5 different random seeds for the turbulence, with corresponding errorsbars. The orange figure is the mean dust v_{rms} for experiments with different dust particle sizes, averaged over the 27 sub boxes of size 0.33^3pc^3 made from experiments of size 1^3pc^3, and averaged over 5 different random seeds for the turbulence, with corresponding errorsbars. Both figures are averaged over 40 time snapshots from the times: $t = 2.4\ t_{turn}$ to $t = 10\ t_{turn}$.

4.1.5   Outputs for experiments with different experiment sizes

Now that I found that the turbulent cascade had a significant effect when we looked at the v_{rms} over entire experiments, I choose to look at the mean v_{rms} of dust when normalized to the gas v_{rms}. This would get rid of the effect of the turbulent cascade as we do not look at the actual v_{rms} but rather what the ratio in v_{rms} is between the dust and gas in the experiments. The gas in the experiments was calibrated so that the dust v_{rms} would follow a power law in the form of equation 1. To begin with, I wanted to test how well this Larson relation was reproduced in the experiments, by comparing the gas v_{rms} for the different experiment sizes, both for the mean

over full experiments of sizes $0.33^3 pc^3$, $1^3 pc^3$, $3^3 pc^3$, $9^3 pc^3$, and $27^3 pc^3$, the mean over sub boxes of sizes $0.33^3 pc^3$, $1^3 pc^3$, $3^3 pc^3$, and $9^3 pc^3$, and the mean over sub-sub boxes of sizes $0.33^3 pc^3$, $1^3 pc^3$, and $3^3 pc^3$ as shown in figure 15.
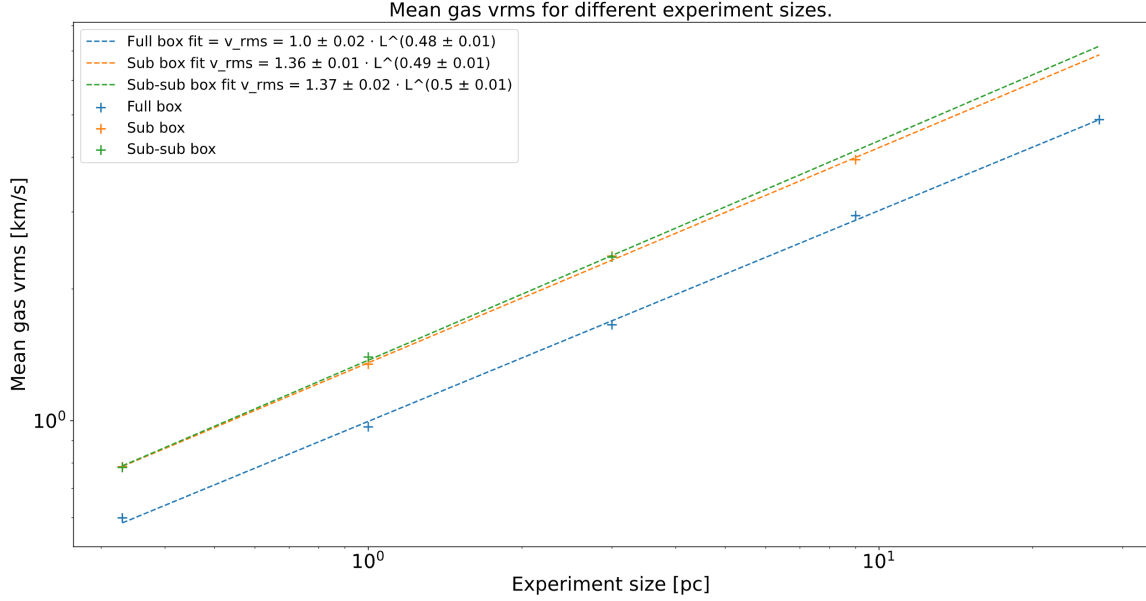

Figure 15: The gas v_{rms} averaged over the different dust sizes ($0.001\mu m$, $0.01\mu m$, $0.1\mu m$, $1\mu m$, $10\mu m$, $100\mu m$, $200\mu m$, and $500\mu m$) and experiment sizes ($0.33^3 pc^3$, $1^3 pc^3$, $3^3 pc^3$, $9^3 pc^3$, $27^3 pc^3$), in loglog space. The mean was made over 40 time snapshots going from $t = 2.4 \ t_{turn}$ to $t = 10 \ t_{turn}$. The blue crosses here represents the mean gas v_{rms} of the entire experiment, the orange crosses represents the mean gas v_{rms} averaged over 27 sub boxes of the different experiment sizes, and the green crosses represents the mean gas v_{rms} averaged over 729 sub-sub boxes of the different experiment sizes. Making a fit on the form $\sigma = a \cdot L^b$, corresponding to equation 1, gives a and b values of $a = 1.0 \pm 0.02$ and $b = 0.48 \pm 0.01$ when looking at the entire experiments, $a = 1.36 \pm 0.01$ and $b = 0.49 \pm 0.01$ when looking at the average over 27 sub boxes of the experiments, and $a = 1.37 \pm 0.02$ and $b = 0.5 \pm 0.01$ when looking at the average over 729 sub-sub boxes of the experiments. The dotted lines in the figure represent the fit of the mean gas v_{rms} as a function of the experiment size for the mean over the entire experiment, the mean over the sub boxes, and the mean over the sub-sub boxes.

Looking at figure 15, we see that the mean gas v_{rms} for both the full experiments, the sub boxes, and the sub-sub boxes have a power law relationship with the experiment sizes. If we fit the different mean gas v_{rms} as a function of the experiment sizes to an equation on the form of equation 1, we find the mean gas v_{rms} over the entire experiment to have a Larson relation of $v_{rms}(gas\ box) = 1.00 \cdot L^{0.48}$, the mean gas v_{rms} averaged over the sub boxes of the experiments to have a Larson relation of $v_{rms}(gas\ sub\ box) = 1.36 \cdot L^{0.49}$, and the mean gas v_{rms} averaged over the sub-sub boxes of the experiments to have a Larson relation of $v_{rms}(gas\ sub-sub\ box) = 1.37 \cdot L^{0.50}$. Thus we see that a power law of the mean gas v_{rms} as a function of the experiment size is to be found in my experiments, even though the values of a and b are different than the ones assumed in my previous calculations. The results here are between $12 - 24\%$ away from the values I have considered previously, which is acceptable when considering the spread in the values of the mean gas v_{rms} power law when observing the first Larson relation in MCs/GMCs in the universe. If we look at the power laws, depicted as dotted lines in figure 15, we see that they overlap with the results accurate enough for us to assume that the fits are proper approximations of the relation between the gas v_{rms} and the size of the experiment. A Pearson's chi squared test on the fits results in p values of 0.99 for all three fits, which shows that the fits are proper approximations of the data points.

Next, I found the mean v_{rms} of the dust in experiments of size $0.33^3 pc^3$, $1^3 pc^3$, $3^3 pc^3$, $9^3 pc^3$,

and $27^3 pc^3$ for 8 different dust particle sizes, namely $0.001\mu m$, $0.01\mu m$, $0.1\mu m$, $1\mu m$, $10\mu m$, $100\mu m$, $200\mu m$, and $500\mu m$. Then I found the mean v_{rms} of the gas for the same experiments and divided the mean dust v_{rms} with the mean gas v_{rms}. The result of these calculations can be seen in figure 16. Then I did the same for the sub boxes of the experiments with sizes $1^3 pc^3$ (creating 27 $0.33^3 pc^3$ sub boxes), $3^3 pc^3$ (creating 27 $1^3 pc^3$ sub boxes), $9^3 pc^3$ (creating 27 $3^3 pc^3$ sub boxes), and $27^3 pc^3$ (creating 27 $9^3 pc^3$ sub boxes). For the sub boxes, the average dust- and gas v_{rms} was found in the 27 individual sub boxes of the different experiments, and a mean was made over the 27 sub boxes, before dividing the two. In the end the same procedure was performed with the sub-sub boxes of the experiments with sizes $3^3 pc^3$ (creating 729 $0.33^3 pc^3$ sub-sub boxes), $9^3 pc^3$ (creating 729 $1^3 pc^3$ sub-sub boxes), $27^3 pc^3$ (creating 729 $3^3 pc^3$ sub-sub boxes). For the sub-sub boxes, the average dust- and gas v_{rms} was found in the 729 individual sub-sub boxes of the different experiments, and a mean was made over the 729 sub-sub boxes, before dividing the two. The result for the sub boxes can be seen in figure 17 and for the sub-sub boxes in figure 18. Here the sub box of size $27^3 pc^3$ is not present since I did not do a $81^3 pc^3$ experiment, and the sub-sub boxes of size $9^3 pc^3$ and $27^3 pc^3$ are not present, since I did not do a $81^3 pc^3$ or a $243^3 pc^3$ experiment, which would be able to create the sub- and sub-sub boxes needed. Running experiments of these sizes with a proper resolution would require more memory than was available. The standard deviation (std) was also found when calculating the mean dust v_{rms} normalized to the mean gas v_{rms}, which is shown as the errorbars in figure 16 to 18.
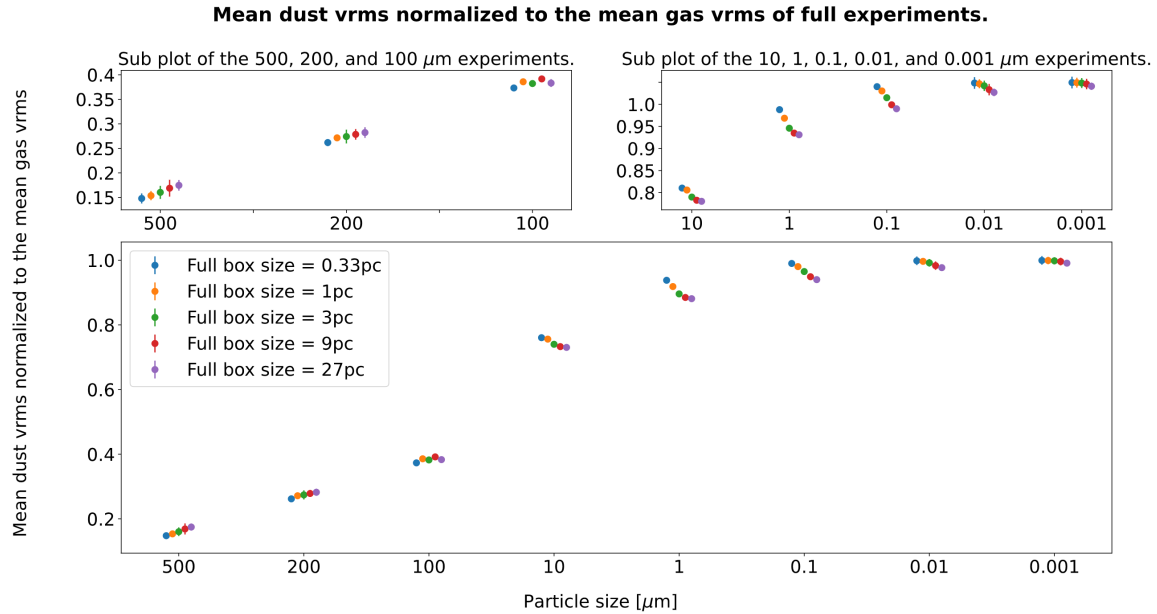

Figure 16: The mean dust v_{rms} normalized to the mean gas v_{rms} in the same experiment, as a function of the particle size, averaged over 40 time snapshots from $t = 2.4\ t_{turn}$ to $t = 10\ t_{turn}$, with corresponding errorbars, for 5 different experiment sizes namely $0.33^3 pc^3$, $1^3 pc^3$, $3^3 pc^3$, $9^3 pc^3$, and $27^3 pc^3$. The two sub plots at the top of the figure is to the left, a zoom in on the mean dust v_{rms} normalized to the mean gas v_{rms} of the experiments with dust size 100, 200, and 500 μm, and on the right, a zoom in on the mean dust v_{rms} normalized to the mean gas v_{rms} of the experiments with dust size 0.001, 0.01, 0.1, 1, and 10 μm.

From the experiments shown in figure 16, where we look at the mean over the entire experiment, we see that the dust particles of size $0.001\mu m$ for all the different experiment sizes have the same normalized mean dust v_{rms} of approximately 1. This means that no matter what experiment size we look at, all the dust will be coupled almost completely to the gas when looking at dust particles at size $0.001\mu m$. At $0.01\mu m$ the different experiment sizes normalized mean dust v_{rms} value lies a bit below 1, and are thus still very coupled to the gas, but starts to have a mean
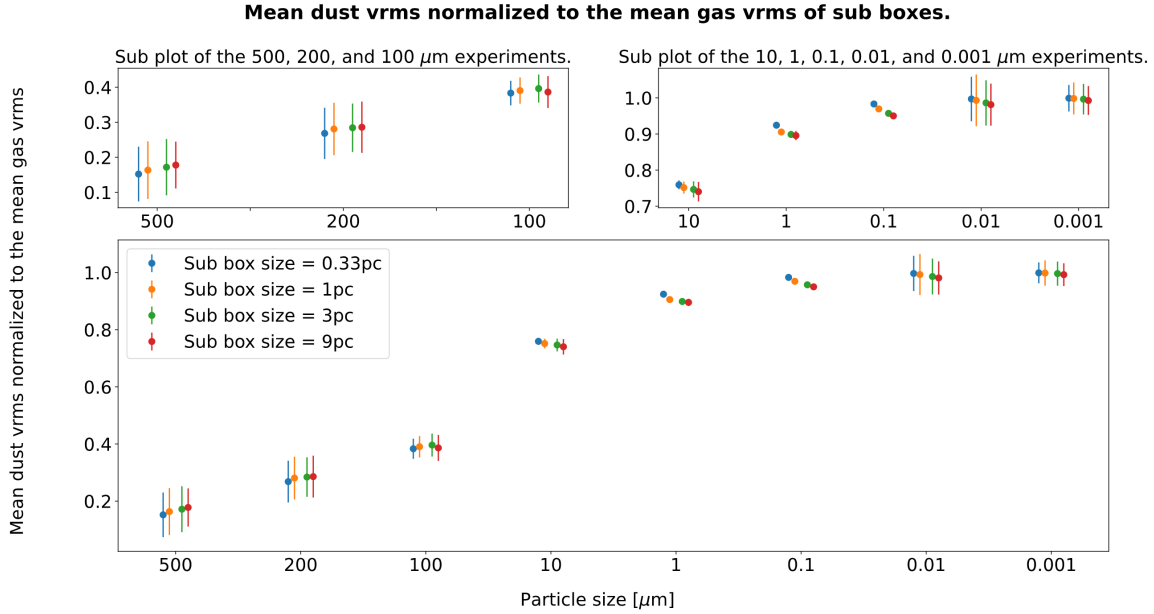
Mean dust vrms normalized to the mean gas vrms of sub boxes.

Figure 17: The mean dust v_{rms} normalized to the mean gas v_{rms} in the same experiment, as a function of the particle size, averaged over 40 time snapshots from $t = 2.4\ t_{turn}$ to $t = 10\ t_{turn}$, with corresponding errorbars, made from the mean over 27 sub boxes of experiments with sub box size $0.33^3 pc^3$ made from an experiment with size $1^3 pc^3$, sub box size $1^3 pc^3$ made from an experiment with size $3^3 pc^3$, sub box size $3^3 pc^3$ made from an experiment with size $9^3 pc^3$, and sub box size $9^3 pc^3$ made from an experiment with size $27^3 pc^3$. The two sub plots at the top of the figure is to the left, a zoom in on the mean dust v_{rms} normalized to the mean gas v_{rms} of the experiments with dust size 100, 200, and 500 μm, and on the right, a zoom in on the mean dust v_{rms} normalized to the mean gas v_{rms} of the experiments with dust size 0.001, 0.01, 0.1, 1, and 10 μm.

v_{rms} that lies below the gas v_{rms}, therefore moving a little bit differently than the gas. The trend continues for the $0.1\mu m$, $1\mu m$, and $10\mu m$ dust size experiments. And when we look at the difference in normalized mean dust v_{rms} between the $10\mu m$ experiments and the $100\mu m$ experiments, we see a big jump in the general normalized mean dust v_{rms}. This is also what we would expect since we calculated the dust size, where a smaller dust particle size than this would result in the dust being stopped by the gas inside the experiment, to be $55.83\mu m$ in equation 16. Now we can look at how the normalized mean dust v_{rms} changes for experiments of different sizes and a fixed dust particle size. For dust particles of size 0.001 to $10\mu m$ we see a approximate linear trend, where the smallest experiment size has a general mean dust v_{rms} closest to the mean gas v_{rms}, and as we move towards larger experiment sizes the normalized mean dust v_{rms} becomes smaller and smaller. The trends of the normalized mean dust v_{rms} as a function of the experiment size, have a different slope depending on what dust particle size we observe. Looking now at the last three dust sizes, namely $100\mu m$, $200\mu m$, and $500\mu m$, we see the trend of the experiment sizes have flipped so that we now see a falling mean dust v_{rms} normalized to the mean gas v_{rms} going from the largest experiment size to the smallest experiment size. We see that the general mean dust v_{rms} normalized to the mean gas v_{rms} still has a falling trend from $100\mu m$ to $500\mu m$, but that the decrease in normalized mean dust v_{rms} becomes less steep than between $10\mu m$ to $100\mu m$. This is due to the dust particles having a decrease in coupling to the gas as we go towards larger and larger dust particles and will continue to fall in the normalized mean dust v_{rms} towards a value of 0.

A non-constant trend in the relation between the normalized mean dust v_{rms} and the size of the experiment, is due to the power law between the mean dust v_{rms} and the experiment size deviating from the power law relation between the mean gas v_{rms} and the experiment size. We see the trends between the normalized mean dust v_{rms} and the experiment size in figure 16 to
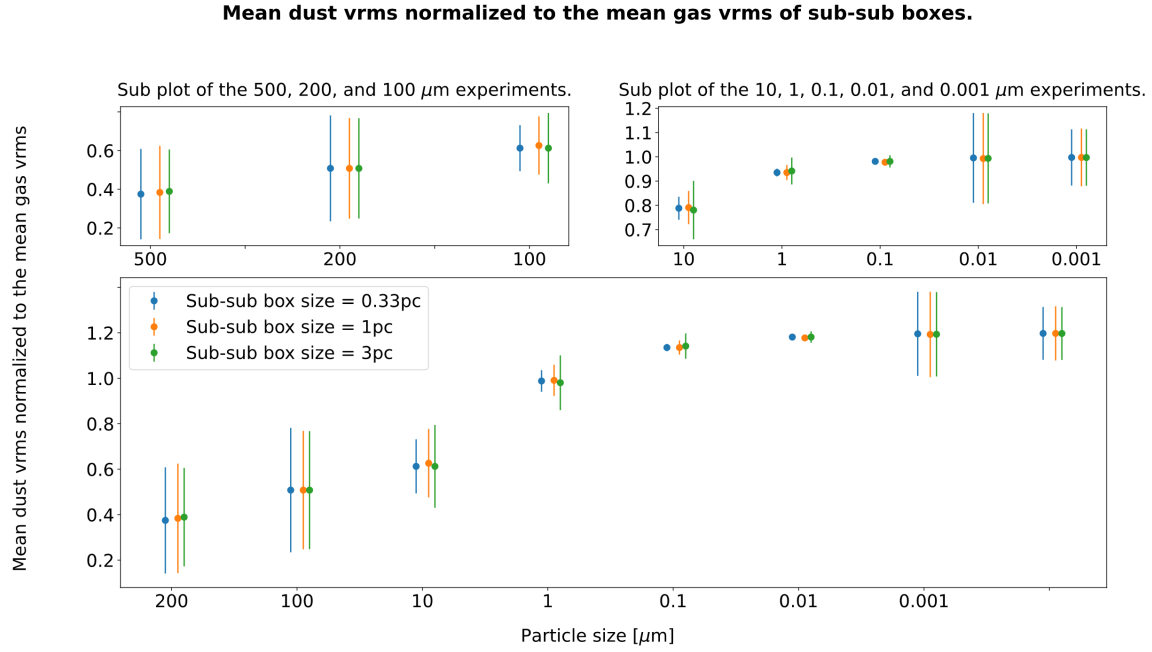
Mean dust vrms normalized to the mean gas vrms of sub-sub boxes.

Figure 18: The mean dust v_{rms} normalized to the mean gas v_{rms} in the same experiment, as a function of the particle size, averaged over 40 time snapshots from $t = 2.4\ t_{turn}$ to $t = 10\ t_{turn}$, with corresponding errorbars, made from the mean over 729 sub-sub boxes of experiments with sub-sub box size $0.33^3 pc^3$ made from an experiment with size $3^3 pc^3$, sub-sub box size $1^3 pc^3$ made from an experiment with size $9^3 pc^3$, and sub-sub box size $3^3 pc^3$ made from an experiment with size $27^3 pc^3$. The two sub plots at the top of the figure is to the left, a zoom in on the mean dust v_{rms} normalized to the mean gas v_{rms} of the experiments with dust size 100, 200, and 500 μm, and on the right, a zoom in on the mean dust v_{rms} normalized to the mean gas v_{rms} of the experiments with dust size 0.001, 0.01, 0.1, 1, and 10 μm.

18 for dust particles of size 0.01 to $500\mu m$. When we have a decreasing slope, having larger normalized mean dust v_{rms} for smaller experiment sizes, like for experiments containing dust particles of size $0.001\mu m$, $0.01\mu m$, $0.1\mu m$, $1\mu m$, and $10\mu m$, the power law relation between the mean dust v_{rms} and the experiment size will have a smaller exponent than in the Larson relation for the gas in the experiment. If we have an increasing slope, having larger normalized mean dust v_{rms} for larger experiment sizes, as we have for experiments with dust particles of size $100\mu m$, $200\mu m$, and $500\mu m$, the power law relation between the mean dust v_{rms} and the experiment size will have a larger exponent than in the Larson relation for the gas in the experiment.

If we now look at the normalized mean dust v_{rms} figures taking the mean over the sub boxes and the sub-sub boxes, namely figure 17 and 18, we see that the normalized mean dust v_{rms} is less when looking at the entire experiments as compared to the mean over the sub boxes and the sub-sub boxes. If we look at the $500\mu m$ experiments we see that the entire experiment normalized mean dust v_{rms} has a value between $0.14 - 0.17$, for the mean over sub boxes the normalized mean dust v_{rms} is between $0.15 - 0.18$, and for the mean over sub-sub boxes the normalized mean dust v_{rms} is between $0.17 - 0.19$. This is due to the dust particles having the possibility of obtaining a larger velocity inside larger experiments, since a particle inside a $3^3 pc^3$ experiment where we take the mean over the 729 sub-sub boxes of size $0.33^3 pc^3$, will have a larger volume to be worked on by the turbulent force and thereby be accelerated to larger velocities than if we only have a $0.33^3 pc^3$ experiment and we find the v_{rms} over the entire experiment. This gives a larger general normalized mean dust v_{rms} when taking the mean over the sub boxes as compared to looking at the entire experiment, as well as an even larger normalized mean dust v_{rms} when taking the mean over the sub-sub boxes as compared to the normalized mean dust v_{rms} over the entire experiment. Another difference between the three

figures is the errorbars, being larger for mean over the entire experiment compared to the mean over the sub-sub boxes. This is due to the number of cells used in the experiments is the same when we look at the mean over the entire experiment, the mean over the sub boxes, and the mean over the sub-sub boxes, resulting in the sub boxes having a lower resolution than the entire experiments, and the sub-sub boxes having an even lower resolution than the sub boxes. The increase in standard deviation is thus due to the large noise in the data for the sub- and sub-sub boxes connected to a low resolution. The uncertainties are the largest at very large and very small dust particles for the sub- and sub-sub boxes, which is a sign of significantly low resolution.

Now I wanted to find the power law between the normalized mean dust v_{rms} and the experiment/sub box/sub-sub box size. I did this by fitting a power law ($vrms_{dustnorm} = a \cdot L^b$) to the different values found at every dust particle size individually. The result from these fits can be found in figure 19 to 21.

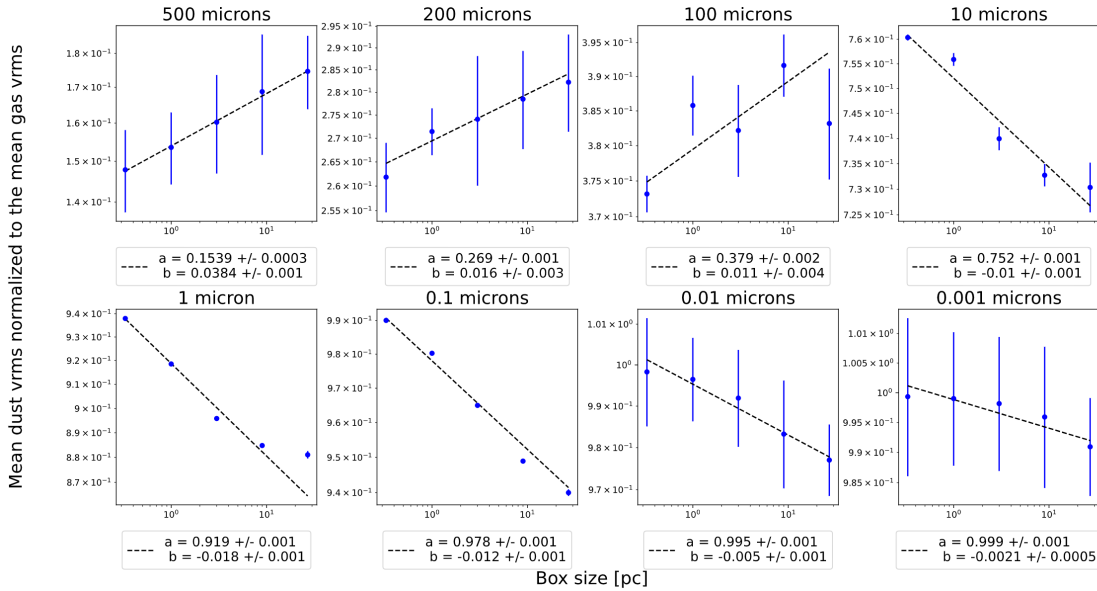Power law fits of the mean dust vrms normalized to the mean gas vrms as a function of the experiment size.

Figure 19: The mean dust v_{rms} normalized to the average gas v_{rms} in experiments with the same sized dust particles, as a function of the experiment size in pc, averaged over 40 time snapshots from $t = 2.4\ t_{turn}$ to $t = 10\ t_{turn}$, with corresponding errorbars and power law fits. In the top left figure, we have the normalized mean dust v_{rms} for a $0.33^3 pc^3$ experiment, a $1^3 pc^3$ experiment, a $3^3 pc^3$ experiment, a $9^3 pc^3$ experiment, and a $27^3 pc^3$ experiment (from left to right in the figure), for experiments containing dust particles of size $500 \mu m$. The upper left figure also has a dashed line corresponding to the power law fit made for the normalized mean dust v_{rms} as a function of the experiment sizes for the $500 \mu m$ experiment. The power law is shown in the legend box. Going from the top left to the top right and then from the bottom left to the bottom right, we see the same figure as just described for experiments containing dust particles of size $200 \mu m$, $100 \mu m$, $10 \mu m$, $1 \mu m$, $0.1 \mu m$, $0.01 \mu m$, and $0.001 \mu m$.

The fits made using the mean over the sub-sub boxes, shown in figure 21, have been made using only three normalized mean dust v_{rms} values. These three values all have a significant standard deviation, and should only be used as an extra indicator in combination with the fits for the mean over the entire experiments and the mean over the sub boxes since the fit coefficients mostly have the same- and a smaller value than their uncertainties. Looking at the three figures we see that the fits follows the actual values accurately both when we look at the mean over the entire experiments, the mean over the sub boxes, and the mean over the sub-sub boxes. Doing a Pearson's Chi squared test on the fits, gives a p values of 0.99 for all of the fits made in the three
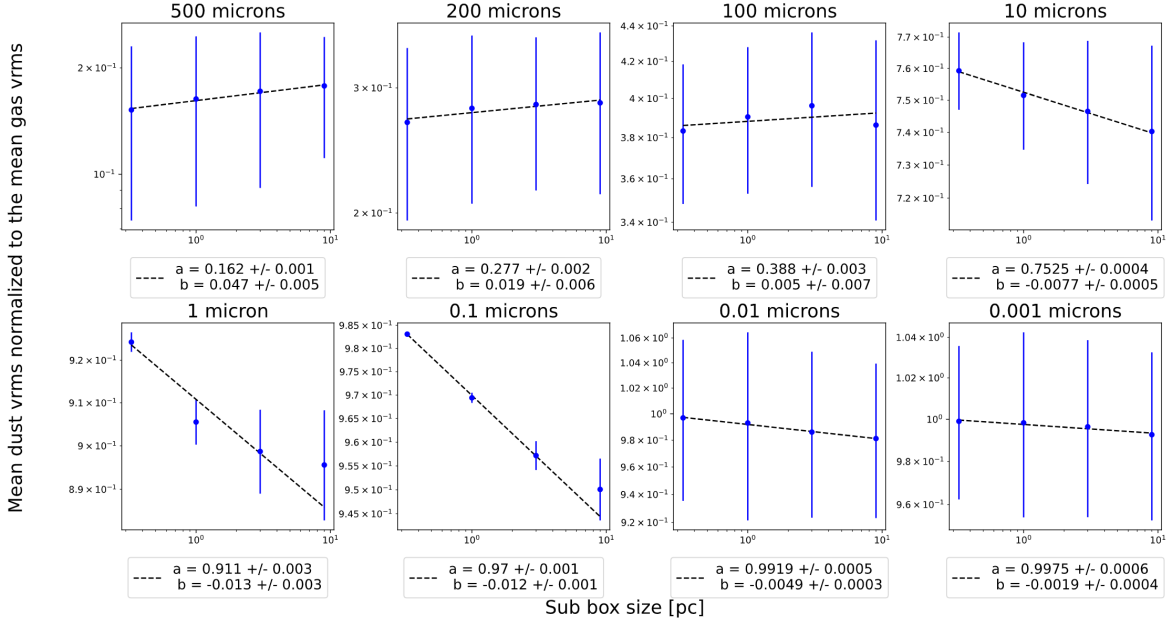
Power law fits of the mean dust vrms normalized to the mean gas vrms as a function of the sub box size.

Figure 20: The mean dust v_{rms} normalized to the average gas v_{rms} in experiments with the same sized dust particles, as a function of the sub box size in pc, averaged over 27 sub boxes and averaged over 40 time snapshots from $t = 2.4\ t_{turn}$ to $t = 10\ t_{turn}$, with corresponding errorbars and power law fits. In the top left figure, we have the normalized mean dust v_{rms} for the mean over 27 $0.33^3 pc^3$ sub boxes, over $1^3 pc^3$ sub boxes, over $3^3 pc^3$ sub boxes, and over $9^3 pc^3$ sub boxes (from left to right in the figure), for experiments containing dust particles of size $500\mu m$. The upper left figure also has a dashed line corresponding to the power law fit made for the normalized mean dust v_{rms} as a function of the sub experiment sizes for the $500\mu m$ experiment. The power law fitted is shown in the legend box. Going from the top left to the top right and then from the bottom left to the bottom right, we see the same figure as just described for experiments containing dust particles of size $200\mu m$, $100\mu m$, $10\mu m$, $1\mu m$, $0.1\mu m$, $0.01\mu m$, and $0.001\mu m$.

figures, which means that the power law fit is the most proper fit for the normalized mean dust v_{rms} as a function of the experiment/sub box/sub-sub box size, for experiments that contain dust particles of a single size.

The fit made for the normalized mean dust v_{rms} as a function of the experiment sizes for an experiment containing dust particles of size $500\mu m$, is given by $v_{rms}(500\ \mu m\ full) = 0.1539 \pm 0.0003 \cdot L^{0.0384\pm0.001}$, for the mean over the 27 sub boxes of each experiment size the power law relationship fitted is given by $v_{rms}(500\ \mu m\ sub) = 0.162 \pm 0.001 \cdot L^{0.047\pm0.005}$, and for the mean over the 729 sub-sub boxes of each experiment size the power law relationship fitted is given by $v_{rms}(500\ \mu m\ sub-sub) = 0.1824 \pm 0.0009 \cdot L^{0.035\pm0.005}$. From figure 15, we know that the first Larson relation in the experiments have been, when taking the mean over the entire experiment: $v_{rms}(gas\ box) = 1.00 \pm 0.02 \cdot L^{0.48\pm0.01}$, when taking the mean over the 27 sub boxes: $v_{rms}(gas\ sub\ box) = 1.36 \pm 0.01 \cdot L^{0.49\pm0.01}$, and when taking the mean over the 729 sub-sub boxes: $v_{rms}(gas\ sub-sub\ box) = 1.37 \pm 0.02 \cdot L^{0.50\pm0.01}$. Now we are interested in finding the power law fits for the unnormalized mean dust v_{rms}. In order to do so we need to look at how the fits in figure 19 to 21 are defined, which is given by

$$Norm\ Dust\ v_{rms} = \frac{v_{rms}(dust)}{v_{rms}(gas)}\ . \tag{69}$$

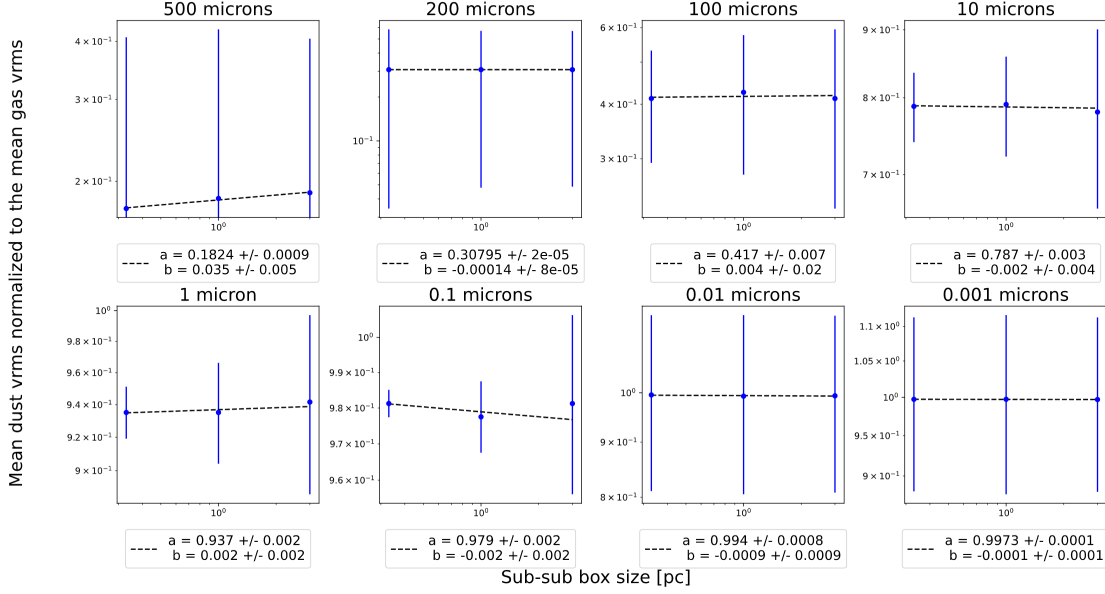If we want to find the mean dust v_{rms} we have to solve the relation in equation 69 for $v_{rms}(dust)$, as

Power law fits of the mean dust vrms normalized to the mean gas vrms as a function of the sub-sub box size.

Figure 21: The mean dust v_{rms} normalized to the average gas v_{rms} in experiments with the same sized dust particles, as a function of the sub-sub box size in pc, averaged over 729 sub-sub boxes and averaged over 40 time snapshots from $t = 2.4\ t_{turn}$ to $t = 10\ t_{turn}$, with corresponding errorbars and power law fits. In the top left figure, we have the normalized mean dust v_{rms} for the mean over 729 $0.33^3 pc^3$ sub-sub boxes, over $1^3 pc^3$ sub-sub boxes, and over $3^3 pc^3$ sub-sub boxes (from left to right in the figure), for experiments containing dust particles of size $500\mu m$. The upper left figure also has a dashed line corresponding to the power law fit made for the normalized mean dust v_{rms} as a function of the sub-sub experiment sizes for the $500\mu m$ experiment. The power law fitted is shown in the legend box. Going from the top left to the top right and then from the bottom left to the bottom right, we see the same figure as just described for experiments containing dust particles of size $200\mu m$, $100\mu m$, $10\mu m$, $1\mu m$, $0.1\mu m$, $0.01\mu m$, and $0.001\mu m$.

$$v_{rms}(dust) = v_{rms}(norm) \cdot v_{rms}(gas) = a_{norm} \cdot L^{b_{norm}} \cdot a_{gas} \cdot L^{b_{gas}} = a_{dust} \cdot a_{gas} \cdot L^{b_{norm} + b_{gas}}\ . \quad (70)$$

Using equation 70, we can find the power law relation between the mean dust v_{rms} and the experiment sizes for the $500\mu m$ experiment

$$v_{rms}(500\mu m) = 0.1539 \pm 0.0003 \cdot 1.00 \pm 0.02 \cdot L^{0.0384 \pm 0.001 + 0.48 \pm 0.01} = 0.154 \pm 0.003 \cdot L^{0.52 \pm 0.01}\ . \quad (71)$$

By doing the same procedure as just shown, we can find the mean dust v_{rms} for the fits made over all 8 dust particle sizes between the mean dust v_{rms} and the experiment/sub box/sub-sub box size. These results are shown in table 3.

Looking at table 3 we see that the mean dust v_{rms} power law made using the mean over 729 sub-sub boxes has the same power law exponent as the mean gas v_{rms}, for all of the different dust particle sizes except $500\mu m$. Since the sub-sub box power laws, as previously mentioned, are made using only three normalized mean dust v_{rms}, each with a large standard deviation, it is appropriate to ignore these power law fits, and instead focus on the power law fits made using the mean over the entire experiment and over the 27 sub boxes. We see that for all different dust particle sizes the mean dust v_{rms} will increase with an increasing MC/GMC size. This tendency is the same for the mean gas v_{rms}, which follows the first Larson relation. Another general trend we see in the power laws for the mean over the entire experiment and over the sub boxes

Dust particle size	Full experiment/sub box/sub-sub box	Mean dust v_{rms} as a function of experiment size power law fit
500μm	Full experiment	$0.154 \pm 0.003 \cdot L^{0.52 \pm 0.01}$
	Sub box	$0.220 \pm 0.003 \cdot L^{0.54 \pm 0.02}$
	Sub-sub box	$0.250 \pm 0.005 \cdot L^{0.54 \pm 0.02}$
200μm	Full experiment	$0.269 \pm 0.006 \cdot L^{0.50 \pm 0.01}$
	Sub box	$0.377 \pm 0.005 \cdot L^{0.51 \pm 0.02}$
	Sub-sub box	$0.422 \pm 0.006 \cdot L^{0.50 \pm 0.01}$
100μm	Full experiment	$0.38 \pm 0.01 \cdot L^{0.49 \pm 0.01}$
	Sub box	$0.53 \pm 0.01 \cdot L^{0.50 \pm 0.02}$
	Sub-sub box	$0.57 \pm 0.02 \cdot L^{0.50 \pm 0.03}$
10μm	Full experiment	$0.75 \pm 0.02 \cdot L^{0.47 \pm 0.01}$
	Sub box	$1.02 \pm 0.01 \cdot L^{0.48 \pm 0.01}$
	Sub-sub box	$1.08 \pm 0.02 \cdot L^{0.50 \pm 0.01}$
1μm	Full experiment	$0.92 \pm 0.02 \cdot L^{0.47 \pm 0.01}$
	Sub box	$1.24 \pm 0.01 \cdot L^{0.48 \pm 0.01}$
	Sub-sub box	$1.28 \pm 0.02 \cdot L^{0.50 \pm 0.01}$
0.1μm	Full experiment	$0.98 \pm 0.02 \cdot L^{0.47 \pm 0.01}$
	Sub box	$1.32 \pm 0.01 \cdot L^{0.48 \pm 0.01}$
	Sub-sub box	$1.34 \pm 0.02 \cdot L^{0.50 \pm 0.01}$
0.01μm	Full experiment	$1.00 \pm 0.02 \cdot L^{0.48 \pm 0.01}$
	Sub box	$1.35 \pm 0.01 \cdot L^{0.49 \pm 0.01}$
	Sub-sub box	$1.36 \pm 0.02 \cdot L^{0.50 \pm 0.01}$
0.001μm	Full experiment	$1.00 \pm 0.02 \cdot L^{0.48 \pm 0.01}$
	Sub box	$1.36 \pm 0.01 \cdot L^{0.49 \pm 0.01}$
	Sub-sub box	$1.37 \pm 0.02 \cdot L^{0.50 \pm 0.01}$
Gas	Full experiment	$1.00 \pm 0.02 \cdot L^{0.48 \pm 0.01}$
	Sub box	$1.36 \pm 0.01 \cdot L^{0.49 \pm 0.01}$
	Sub-sub box	$1.37 \pm 0.02 \cdot L^{0.50 \pm 0.01}$

Table 3: Table showing the power law fit for the mean dust v_{rms} as a function of the experiment/sub box/sub-sub box size, for individual dust particle sizes, as illustrated in figure 19 to 21, as well as the power law fits made for the mean gas v_{rms} as a function of the experiment/sub box/sub-sub box size (figure 15).

is the exponents that L is in the power of, takes on a larger value than in the gas power laws, for an experiment containing dust particles of size $100 - 500 \mu m$. Inside the uncertainties the exponent coefficient becomes equivalent to that of the gas around $100 \mu m$. Another trend shared by the power laws over the entire experiment and the mean over the 27 sub boxes is that the coefficient that we multiply L with has a small value for dust particles of size $500 \mu m$. From there the coefficient increases for smaller and smaller dust particles, and reach the coefficient value of the gas, for dust particles of size $0.01 \mu m$ and smaller, where the dust and gas are coupled, and therefore moves with the same v_{rms}. What we can gain from this is that the dust particles larger than $100 \mu m$ has a mean v_{rms} that are more affected by the size of the MC/GMC we are looking at than the mean gas v_{rms} is, but the mean dust v_{rms} is smaller the larger the dust particle we observe, due to the coefficient we multiply L with. The reason why dust particles larger than $100 \mu m$ mean v_{rms} are more affected by the size of the experiments than smaller dust particles and the gas, is due to the larger dust particles stopping length being larger than the length of the experiment L they are moving around in. This is in accordance with the dust particle size previously found, for the input values in this thesis, for which larger particle sizes will not be stopped inside the experiment they travel in, to be approximately $50 \mu m$. This effect for large dust particles is due to the mean gas density decreasing with an increase in the size of the experiment, since $\rho_g L = constant$, and thus the dust particles will have a less dense gas cylinder working against their movement through friction, the larger the MC/GMC we observe is. The $100 \mu m$ experiment has an exponent with uncertainties so large, that it is not possible, from these power law fits, to tell if the $100 \mu m$ particle also has a stopping length larger than the length of the experiment, which we would assume it to have from the calculations in equation 16. For smaller dust particles (below $100 \mu m$), the exponents of the fits is the same as for the fit of the mean gas v_{rms}, inside the uncertainties, due to these particles having a stopping time smaller than that of the length of the experiment, and will therefore always be stopped inside the experiment, no matter the size, which makes the effect on the mean v_{rms} of an increase in experiment the same for these sized dust particles as for the gas. The coefficient multiplied by L in the power law of particles of size $0.1 \mu m$ - $10 \mu m$ is larger than for dust particles of size $100 \mu m$ and larger, but still smaller than the coefficient in the gas power law fits. This means that for dust particles of size $0.1 \mu m$ to $10 \mu m$ the mean dust v_{rms} is larger than dust particles of a size larger than $100 \mu m$, but lower than the mean gas v_{rms}. This is caused by the dust particles still having a different movement through the MC/GMC than the gas, even though these particles are largely coupled to the gas. For dust particles of size $0.01 \mu m$ and smaller the power law fits are the same as for the gas, inside the uncertainties, since dust particles of these small sizes, are completely coupled to the gas.

I also chose to look at the relative difference in the reference frame between the dust velocity and the gas velocity of a given experiment. I did this by taking the absolute value of the velocity of the dust subtracted by the velocity of the gas in the x, y, and z-direction independently. Then I squared the values found in the three directions, added them together, and took the mean of these values. Next, I took the absolute values of the gas velocity and took the mean of all these values inside the experiments. Then I divided the mean of the dust velocity subtracted by the gas velocity with the mean gas velocity and took the square root of this value. I did this for 40 different time steps and then found the mean over those 40 time frames, between the times of 2.4 turn over times to 10 turn over times. The calculation can be seen in equation 72.

$$\text{Relative Difference} = \left\langle \frac{\langle |v_d - v_g| \rangle}{\langle |v_g| \rangle} \right\rangle_{time} \tag{72}$$

I did this calculation both for the entire experiments of size $0.33^3 pc^3$, $1^3 pc^3$, $3^3 pc^3$, $9^3 pc^3$, and $27^3 pc^3$ seen in figure 22, as well as for the mean over the 27 sub boxes of size $0.33^3 pc^3$ using

the 1^3pc^3 sized experiment, 1^3pc^3 using the 3^3pc^3 sized experiment, 3^3pc^3 using the 9^3pc^3 sized experiment, and 9^3pc^3 using the 27^3pc^3 sized experiment seen in figure 23. I also did the same calculation for the mean over the 729 sub-sub boxes of size 0.33^3pc^3 using the experiment of size 3^3pc^3, 1^3pc^3 using the experiment of size 9^3pc^3, and 3^3pc^3 using the experiment of size 27^3pc^3 seen in figure 24.
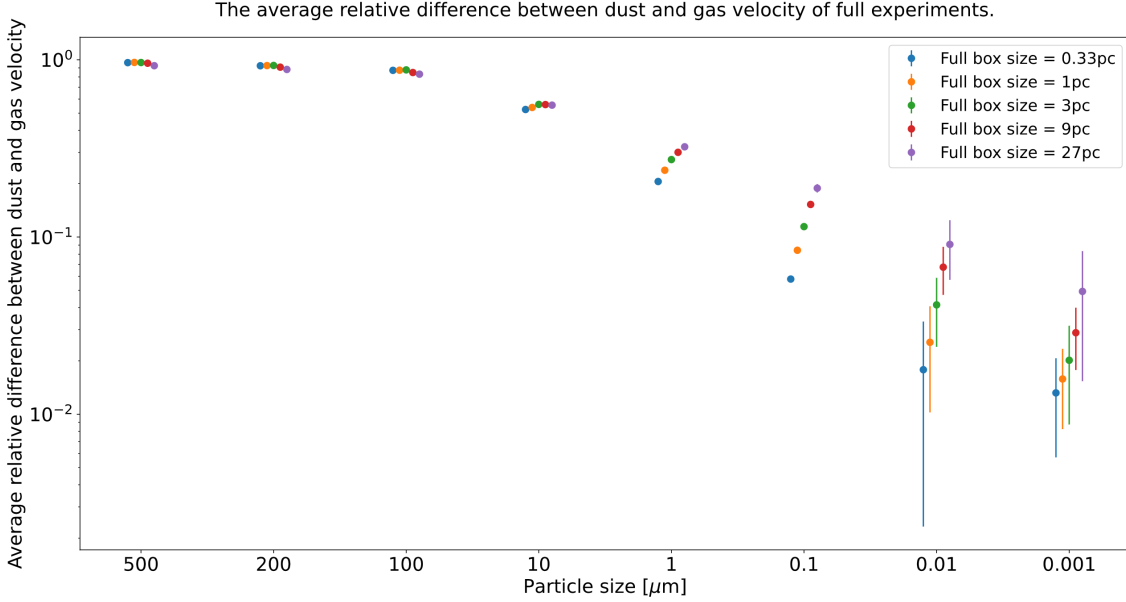

Figure 22: The average relative difference in the reference frame between the dust and gas velocity in the same experiment, as a function of the particle size, averaged over 40 time snapshots from $t = 2.4\ t_{turn}$ to $t = 10\ t_{turn}$, for 5 different experiment sizes namely 0.33^3pc^3, 1^3pc^3, 3^3pc^3, 9^3pc^3, and 27^3pc^3, with corresponding errorbars.
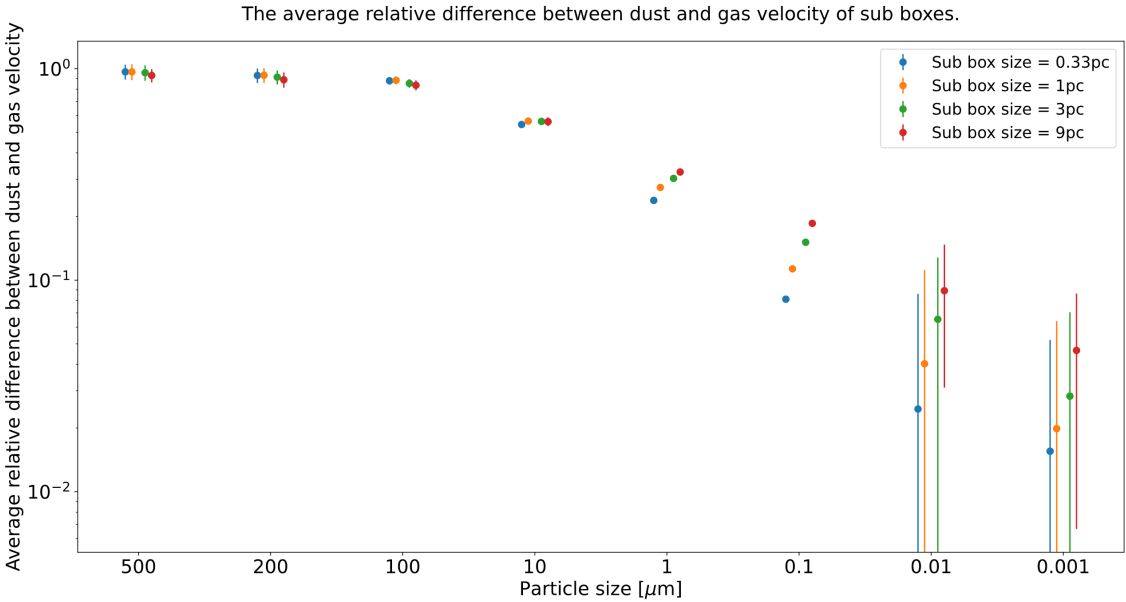

Figure 23: The average relative difference in the reference frame between the dust and gas velocity in the same experiment, as a function of the particle size, averaged over 40 time snapshots from $t = 2.4\ t_{turn}$ to $t = 10\ t_{turn}$, made from the mean over the 27 sub boxes of the different experiments of sub box size 0.33^3pc^3 made from an experiment with size 1^3pc^3, sub box size 1^3pc^3 made from an experiment with size 3^3pc^3, sub box size 3^3pc^3 made from an experiment with size 9^3pc^3, and sub box size 9^3pc^3 made from an experiment with size 27^3pc^3, with corresponding errorbars.
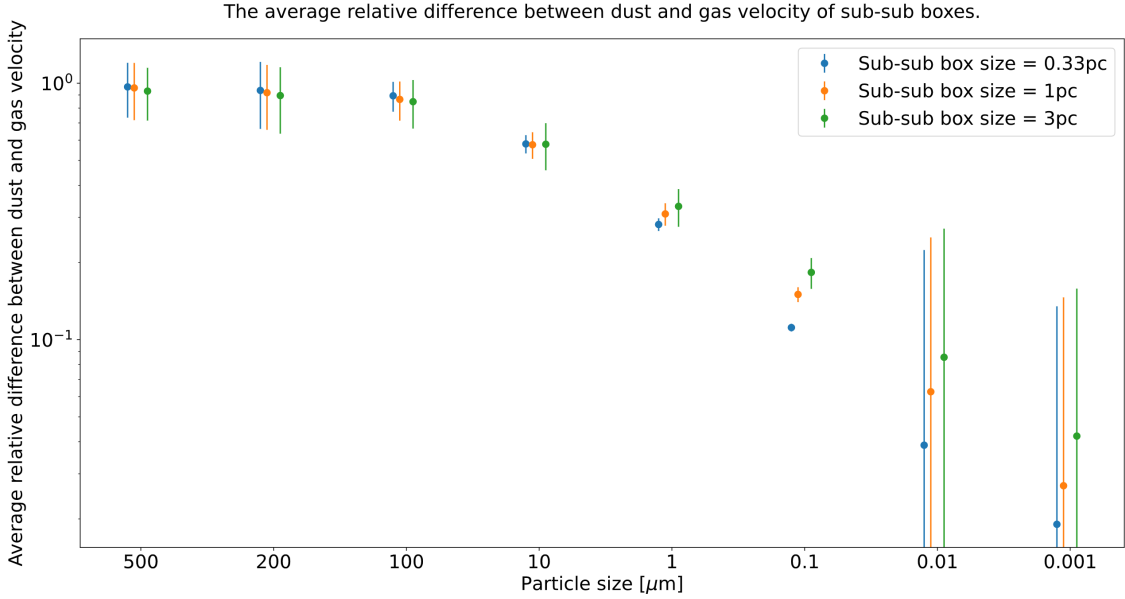
Figure 24: The average relative difference in the reference frame between the dust and gas velocity in the same experiment, as a function of the particle size, averaged over 40 time snapshots from $t = 2.4\ t_{turn}$ to $t = 10\ t_{turn}$, made from the mean over the 729 sub-sub boxes of the different experiments of sub-sub box size $0.33^3 pc^3$ made from an experiment with size $3^3 pc^3$, sub-sub box size $1^3 pc^3$ made from an experiment with size $9^3 pc^3$, and sub-sub box size $3^3 pc^3$ made from an experiment with size $27^3 pc^3$, with corresponding errorbars.

The average relative difference in the reference frame between the dust and gas velocity can tell us something about the coupling between the gas and the dust. If the stopping length is longer than the length of the experiment, sub box, or the sub-sub box ($L_{stop} > L_{box}$) the dust will not be stopped inside the experiment/sub box/sub-sub box, and the value of the relative difference will be close to 1. Here the dust is mostly decoupled from the gas and has its own motion insignificantly affected by the motion of the gas. If the value is close to 0, the dust will be stopped inside the experiment and will be coupled to the gas, and its movement will predominantly follow the gas movement inside the MC/GMC.

From the experiments with the average relative difference in the reference frame between the dust and gas velocity seen in figure 22 to 24, we see that the experiments with dust particles of size $100\mu m$, $200\mu m$, and $500\mu m$ will not be stopped inside the experiment/sub box/sub-sub box that they move inside, since their average relative difference in the reference frame between the dust and gas velocity is close to 1. The $10\mu m$ experiment has an average relative difference between dust and gas velocity that, compared to the larger dust particle experiments, is significantly below 1, and thus there is a larger probability of dust of $10\mu m$ to be stopped inside the experiment/sub box/sub-sub box. This shows that the dust is more and more coupled to the gas when going from larger dust particles to smaller. Continuing going from large dust particles towards smaller dust particles we see the average relative difference in the reference frame between the dust and gas velocity decreasing until it is almost 0 for dust particles of size 0.01 and $0.001\mu m$. The average relative difference in the reference frame between the dust and gas velocity is the mean difference in the dust and gas velocity (Δv) normalized to the gas velocity, and looking at equation 23, we know that the average relative difference in the reference frame between the dust and gas velocity, for small particles, will be proportional to the size of the dust particle and to the experiment/sub box/ sub-sub box size. Large dust particles will be so decoupled from the gas that they will have a constant value of almost one for any experiment/sub box/sub-sub box size and are therefore not dependent on the experiment/sub box/sub-sub box size. We see the dependence from equation 23 in the three figures, from the average relative

Power law fits of the average relative difference between dust and gas velocity as a function of the full experiments size.
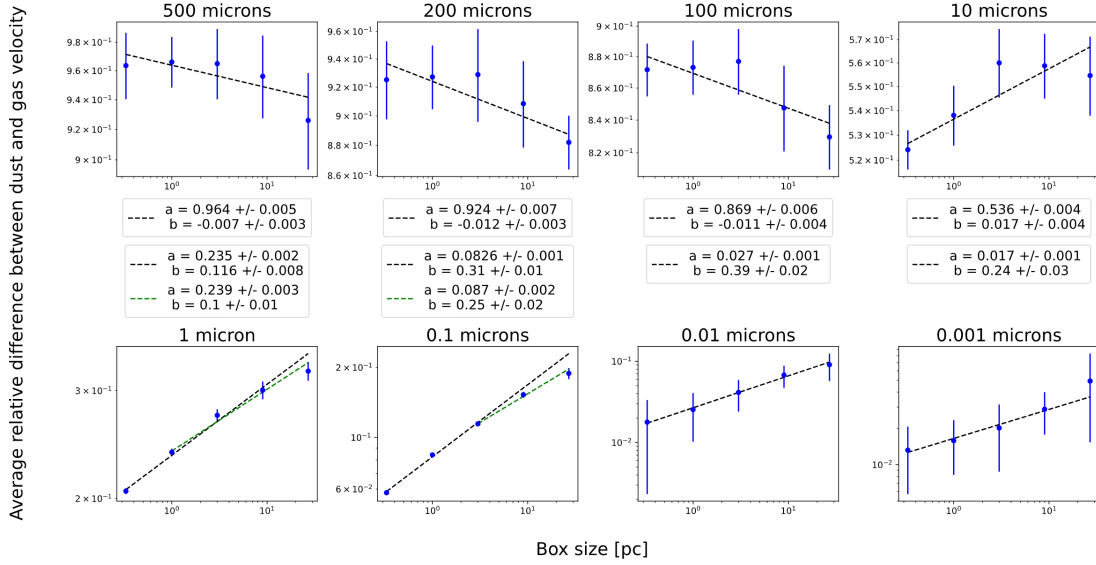

Figure 25: The average relative difference in the reference frame between the dust and gas velocity in experiments with the same sized dust particles, as a function of the experiment size in pc, averaged over 40 time snapshots from $t = 2.4\ t_{turn}$ to $t = 10\ t_{turn}$, with corresponding errorbars and power law fits. In the top left figure, we have the average relative difference in the reference frame between the dust and gas velocity for a $0.33^3 pc^3$ experiment, a $1^3 pc^3$ experiment, a $3^3 pc^3$ experiment, a $9^3 pc^3$ experiment, and a $27^3 pc^3$ experiment (from left to right in the figure), for experiments containing dust particles of size $500\mu m$. The upper left figure also has a dashed line corresponding to the power law fit made over the average relative difference in the reference frame between the dust and gas velocity as a function of the experiment sizes for the $500\mu m$ experiment. The power law is shown in the legend box. Going from the top left to the top right and then from the bottom left to the bottom right, we see figures similar to the one just described for experiments containing dust particles of size $200\mu m$, $100\mu m$, $10\mu m$, $1\mu m$, $0.1\mu m$, $0.01\mu m$, and $0.001\mu m$. The green dashed line present, in the figure for experiments containing dust particles of size $0.1\mu m$, and $1\mu m$, is a fit made over the experiment sizes corresponding to a supersonic relative difference in the reference frame between the dust and gas velocity, and a single experiment size corresponding to a relative difference in the reference frame between the dust and gas velocity just below the supersonic regime.

difference in the reference frame between the dust and gas velocity increasing as a function of the dust size and the experiment/sub box/ sub-sub box size, looking at dust particles of size $1\mu m$ and smaller. If we look at a single experiment/sub box/ sub-sub box size we see an almost linear relationship in loglog space, between the average relative difference in the reference frame between the dust and gas velocity and the dust size, for the different dust particle sizes between $1\mu m$ and $0.001\mu m$. If we look at a single dust particle size between the dust particle sizes of $0.001\mu m$ to $10\mu m$ and look at the average relative difference in the reference frame between the dust and gas velocity over the different experiment/sub box/sub-sub box sizes we also see an almost linear relationship in loglog space.

A linear relationship in loglog space is equivalent to a power law, which means that there must exist a power law relationship between the bulk velocity of the dust particles and the size of the dust particles and another power law relationship between the bulk velocity of the dust particles and the size of the MC/GMC observed. The fits of the average relative difference in the reference frame between the dust and gas velocity as a function of the size of the experiment can be seen in figure 25. The fits for the average relative difference in the reference frame between the dust and gas velocity averaged over 27 sub boxes as a function of the size of the experiment, can be seen in figure 26. And the fits for the average relative difference in the reference frame between the dust and gas velocity averaged over 729 sub-sub boxes as a function of the size of the experiment, can be seen in figure 27. For the fits of the average relative difference in the

Power law fits of the average relative difference between dust and gas velocity as a function of the sub box sizes.
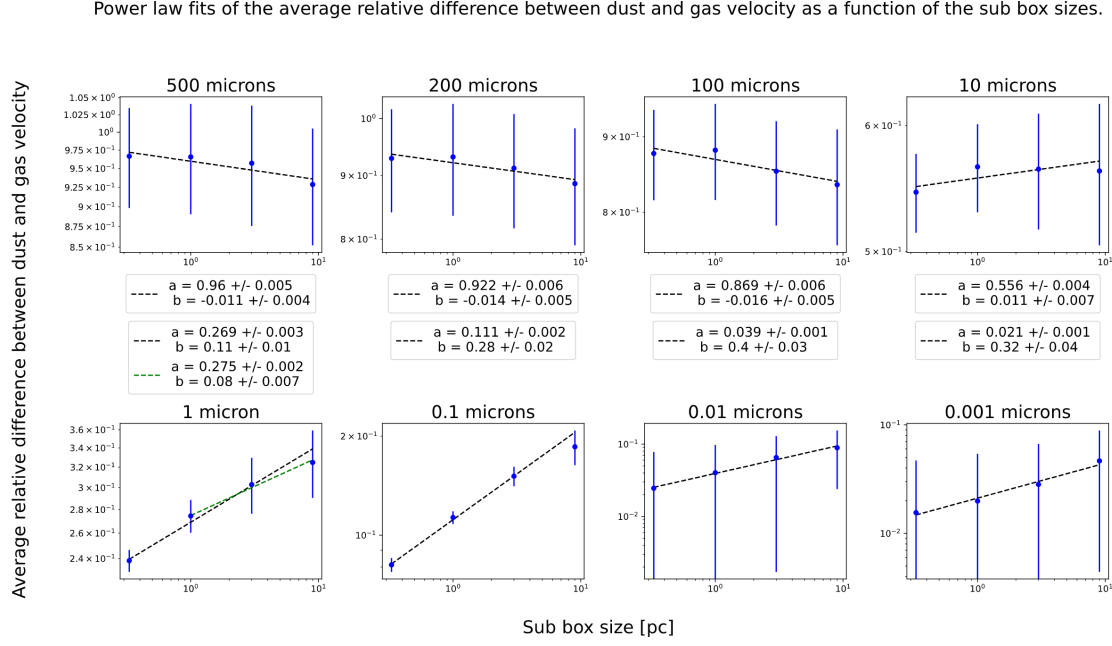

Figure 26: The average relative difference in the reference frame between the dust and gas velocity in experiments with the same sized dust particles, as a function of the sub box size in pc, averaged over 27 sub boxes and averaged over 40 time snapshots from $t = 2.4\ t_{turn}$ to $t = 10\ t_{turn}$, with corresponding errorbars and power law fits. In the top left figure, we have the average relative difference in the reference frame between the dust and gas velocity for the mean over 27 $0.33^3 pc^3$ sub boxes, over $1^3 pc^3$ sub boxes, over $3^3 pc^3$ sub boxes, and over $9^3 pc^3$ sub boxes (from left to right in the figure), for experiments containing dust particles of size $500\mu m$. The upper left figure also has a dashed line corresponding to the power law fit made over the average relative difference in the reference frame between the dust and gas velocity as a function of the sub experiment sizes for the $500\mu m$ experiment. The power law fitted is shown in the legend box. Going from the top left to the top right and then from the bottom left to the bottom right, we see figures similar to the one just described for experiments containing dust particles of size $200\mu m$, $100\mu m$, $10\mu m$, $1\mu m$, $0.1\mu m$, $0.01\mu m$, and $0.001\mu m$. The green dashed line present in the figure representing experiments containing dust particles of size $1\mu m$, is a fit made over the experiment sizes corresponding to a supersonic relative difference in the reference frame between the dust and gas velocity, and a single experiment size corresponding to a relative difference in the reference frame between the dust and gas velocity just below the supersonic regime.

reference frame between the dust and gas velocity as a function of the dust particle size, the fits for the average over the entire experiment can be seen in figure 28, the fits for the average over 27 sub boxes, can be seen in figure 29, and the fits averaged over 729 sub-sub boxes, can be seen in figure 30. Doing the same procedure as with the normalized mean dust v_{rms}, using the mean gas v_{rms} fits found in figure 15, we can find the un-normalized average relative difference in the reference frame between the dust and gas velocity, which can be seen in table 4, and the true relation between the average relative difference in the reference frame between the dust and gas velocity and the dust particle size, can be seen in table 5.

If we look at the $0.33^3 pc^3$ experiment in figure 22, the linear decrease in average relative difference in the reference frame between the dust and gas velocity as we go from larger dust particle sizes towards smaller dust particle sizes, between $0.1\mu m$ and $1\mu m$, starts to flatten. The same tendency, of a flattening of the linear decrease in average relative difference in the reference frame between the dust and gas velocity, is present for the $1^3 pc$ experiment between a dust particle size of $0.001\mu m$ and $0.01\mu m$. The flattening is due to a transition from the supersonic to the subsonic regime. This transition happens when the Mach number changes from being above 1 to below one from equation 4. The speed of sound used in the experiments is set to $c_s = 0.18 km/s$, and if we now observe the average relative difference in the reference frame between the dust and gas velocity when considering the mean over the entire experiment of

The power law fit of the average relative difference between dust and gas velocity as a function of the sub-sub box sizes.
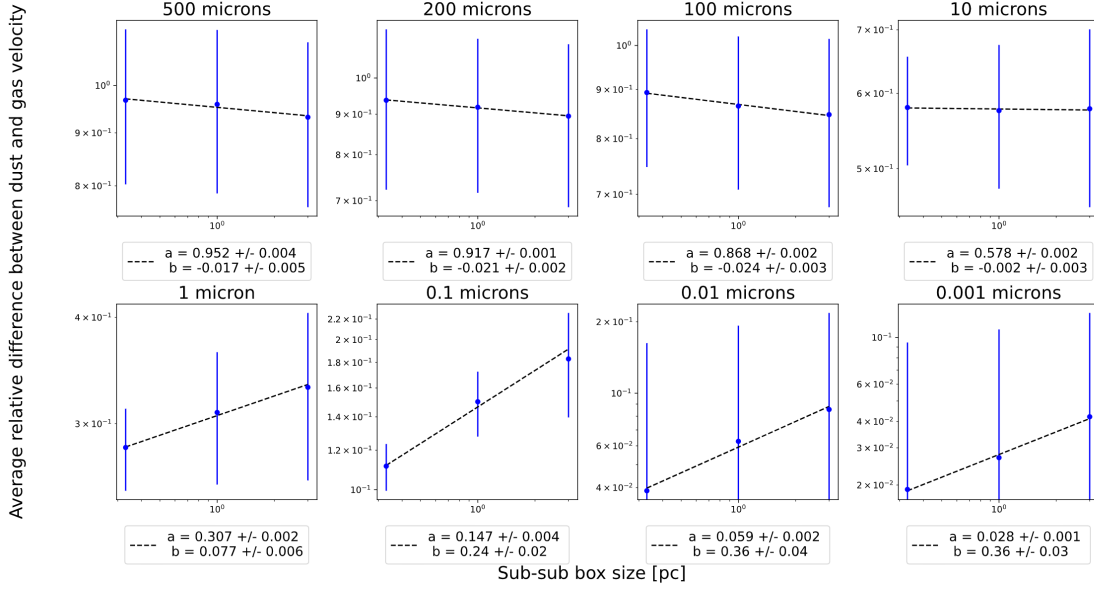

Figure 27: The average relative difference in the reference frame between the dust and gas velocity in experiments with the same sized dust particles, as a function of the sub-sub box size in pc, averaged over 729 sub-sub boxes and averaged over 40 time snapshots from $t = 2.4\ t_{turn}$ to $t = 10\ t_{turn}$, with corresponding errorbars and power law fits. In the top left figure, we have the average relative difference in the reference frame between the dust and gas velocity for the mean over 729 $0.33^3 pc^3$ sub-sub boxes, over $1^3 pc^3$ sub-sub boxes, and over $3^3 pc^3$ sub-sub boxes (from left to right in the figure), for experiments containing dust particles of size $500 \mu m$. The upper left figure also has a dashed line corresponding to the power law fit made over the average relative difference in the reference frame between the dust and gas velocity as a function of the sub-sub experiment sizes for the $500 \mu m$ experiment. The power law fitted is shown in the legend box. Going from the top left to the top right and then from the bottom left to the bottom right, we see figures similar to the one just described for experiments containing dust particles of size $200 \mu m$, $100 \mu m$, $10 \mu m$, $1 \mu m$, $0.1 \mu m$, $0.01 \mu m$, and $0.001 \mu m$.

size $0.33^3 pc^3$, the mean gas v_{rms} should be $1 \cdot 0.33^4 8 = 0.59 km/s$. This gives a Mach number of $M_g = \frac{0.59 km/s}{0.18 km/s} = 3.3$, which is supersonic. The average relative difference in the reference frame between the dust and gas velocity for a $0.33^3 pc^3$ experiment with $1 \mu m$ dust particles are approximately 0.2, and the Mach number for the dust particles are therefore 0.2 times the Mach number of the gas mean: $M_{d-0.33-1} = 0.2 \cdot 3.3 = 0.7$ which is subsonic. If we look at the same experiment size but with $10 \mu m$ dust particles the Mach number is $M_{d-0.33-10} = 0.5 \cdot 3.3 = 1.6$ and thus supersonic. This shows that for experiments of size $0.33^3 pc^3$ and dust particle size less than $1 \mu m$, the dust particles will move with a bulk velocity compared to the gas that is less than the speed of sound and the thermal velocity will therefore be significant causing the Larson relations to become an oversimplification, and the relations can not be used. The same is true for the definition of the stopping time used, which can not be used in the subsonic regime due to oversimplification when the thermal velocity becomes significant. This explains why the average relative difference in the reference frame between the dust and gas velocity stops being linear in loglog space as a function of the dust particle size, when looking at dust particle sizes of $1 \mu m$ and below for a $0.33^3 pc^3$ experiment. If we now look at the Mach number for an experiment of size $1^3 pc^3$ we see that for an experiment containing $1 \mu m$ particles the Mach number is $M_{d-1-1} = 0.25 \cdot \frac{1 \cdot 1^{0.48} km/s}{0.18 km/s} = 1.4$, which is supersonic. Continuing like this, we find the dust particle size, where the average relative difference in the reference frame between the dust and gas velocity starts to flatten and deviate from being linear, to be particles of size $0.1 \mu m$ and below for a $1^3 pc^3$ sized experiment. Performing the same analysis for an experiment of size $3^3 pc^3$ we find the transition from supersonic to subsonic happening between 0.01 and $0.1 \mu m$.

For an experiment of size $9^3 pc^3$ the transition happens between 0.001 and $0.01\mu m$. And for an experiment of size $27^3 pc^3$ the transition happens below $0.001\mu m$. This limits the results we can use to develop a power law between the bulk velocity of the dust particles and the size of the dust particles in the experiments as well as the power law relationship between the bulk dust velocity and the size of the experiment we look at. If we now look at the average relative difference in the reference frame between the dust and gas velocity averaged over 27 sub boxes and over 729 sub-sub boxes, we see the transitions from supersonic to subsonic is the same as for the mean over the entire experiments for all different experiments, except for experiments of size $9^3 pc^3$, where the transition for the mean over the sub boxes happens for particles smaller than $0.001\mu m$.

Power law fits of the average relative difference between dust and gas velocity as a function of the dust particle sizes.
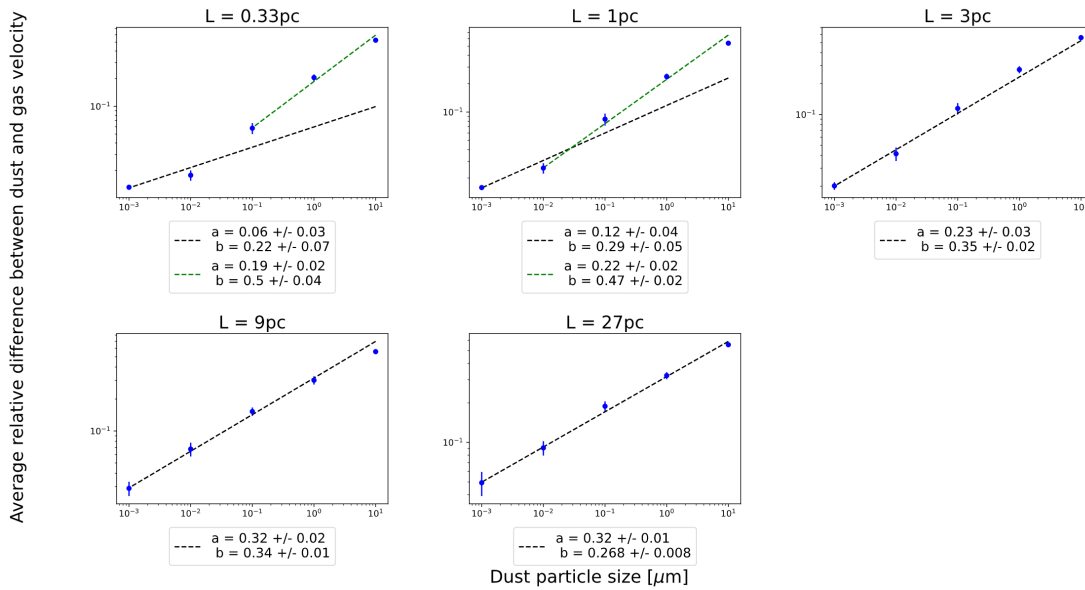

Figure 28: The average relative difference in the reference frame between the dust and gas velocity in experiments with the same experiment size, as a function of the size of the dust particles (0.001 to $10\mu m$) in the experiment, averaged over 40 time snapshots from $t = 2.4\ t_{turn}$ to $t = 10\ t_{turn}$, with corresponding errorbars and power law fits. In the top left figure, we have the average relative difference in the reference frame between the dust and gas velocity for an experiment containing dust particles of size $0.001\mu m$, $0.01\mu m$, $0.1\mu m$, $1\mu m$, and $10\mu m$ (from left to right in the figure), for experiments of experiment size $0.33^3 pc^3$. The upper left figure also has a dashed line corresponding to the power law fit made over the average relative difference in the reference frame between the dust and gas velocity as a function of the size of the dust particles in the experiment for the $0.33^3 pc^3$ sized experiments. The power law is shown in the legend box. Going from the top left to the top right and then from the bottom left to the bottom right, we see figures similar to the one just described for experiments of size $1^3 pc^3$, $3^3 pc^3$, $9^3 pc^3$, and $27^3 pc^3$. The green dashed line present in the figure representing experiments of size $0.33^3 pc^3$, and $1^3 pc^3$ is a fit made over the dust particle sizes moving with a supersonic relative difference in the reference frame between the dust and gas velocity, and a single dust particle size that corresponds to a relative difference in the reference frame between the dust and gas velocity just below the supersonic regime.

In figure 28 to 30, I have used dust particle sizes $0.001\mu m$, $0.01\mu m$, $0.1\mu m$, $1\mu m$ and $10\mu m$. The reason for using the average relative difference in the reference frame between the dust and gas velocity for the experiment containing $10\mu m$ in the fits, is to have enough data points to make proper fits, even though the $10\mu m$ value deviate a bit from the linearity observed in figure 22 to 24. Looking at figure 25 to 30, the green extra fits I have chosen to do for some of the fits, have been made using the supersonic average relative difference in the reference frame between the dust and gas velocity, and the first average relative difference in the reference frame between the dust and gas velocity below a supersonic velocity. My reason to chose one average relative

Dust particle size	Full experiment/sub box/sub-sub box	Average difference in the reference frame between the dust and gas velocity as a function of dust particle size power law fit
500μm	Full experiment	$0.96 \pm 0.02 \cdot L^{0.47 \pm 0.01}$
	Sub box	$1.31 \pm 0.02 \cdot L^{0.48 \pm 0.01}$
	Sub-sub box	$1.30 \pm 0.02 \cdot L^{0.48 \pm 0.02}$
200μm	Full experiment	$0.92 \pm 0.03 \cdot L^{0.47 \pm 0.01}$
	Sub box	$1.25 \pm 0.02 \cdot L^{0.48 \pm 0.02}$
	Sub-sub box	$1.26 \pm 0.02 \cdot L^{0.48 \pm 0.01}$
100μm	Full experiment	$0.87 \pm 0.02 \cdot L^{0.47 \pm 0.01}$
	Sub box	$1.18 \pm 0.02 \cdot L^{0.47 \pm 0.02}$
	Sub-sub box	$1.19 \pm 0.02 \cdot L^{0.48 \pm 0.01}$
10μm	Full experiment	$0.54 \pm 0.01 \cdot L^{0.50 \pm 0.01}$
	Sub box	$0.76 \pm 0.02 \cdot L^{0.50 \pm 0.02}$
	Sub-sub box	$0.79 \pm 0.01 \cdot L^{0.50 \pm 0.01}$
1μm	Full experiment	$0.24 \pm 0.01 \cdot L^{0.58 \pm 0.02}$
	Sub box	$0.37 \pm 0.01 \cdot L^{0.57 \pm 0.02}$
	Sub-sub box	$0.42 \pm 0.01 \cdot L^{0.58 \pm 0.02}$
0.1μm	Full experiment	$0.087 \pm 0.002 \cdot L^{0.73 \pm 0.03}$
	Sub box	$0.151 \pm 0.004 \cdot L^{0.77 \pm 0.03}$
	Sub-sub box	$0.20 \pm 0.01 \cdot L^{0.74 \pm 0.03}$
0.01μm	Full experiment	$0.027 \pm 0.002 \cdot L^{0.87 \pm 0.03}$
	Sub box	$0.053 \pm 0.002 \cdot L^{0.89 \pm 0.04}$
	Sub-sub box	$0.081 \pm 0.004 \cdot L^{0.86 \pm 0.05}$
0.001μm	Full experiment	$0.017 \pm 0.001 \cdot L^{0.72 \pm 0.04}$
	Sub box	$0.029 \pm 0.002 \cdot L^{0.81 \pm 0.05}$
	Sub-sub box	$0.038 \pm 0.002 \cdot L^{0.86 \pm 0.04}$
Gas	Full experiment	$1.00 \pm 0.02 \cdot L^{0.48 \pm 0.01}$
	Sub box	$1.36 \pm 0.01 \cdot L^{0.49 \pm 0.01}$
	Sub-sub box	$1.37 \pm 0.02 \cdot L^{0.50 \pm 0.01}$

Table 4: Table showing the power law fits for the average difference in the reference frame between the dust and gas velocity as a function of the experiment/sub box/sub-sub box size, as well as the power law fits made for the mean gas v_{rms} as a function of the experiment/sub box/sub-sub box size (figure 15), for individual dust particle sizes, illustrated in figure 25 to 27.

Power law fits of the average relative difference between dust and gas velocity as a function of the dust particle sizes.
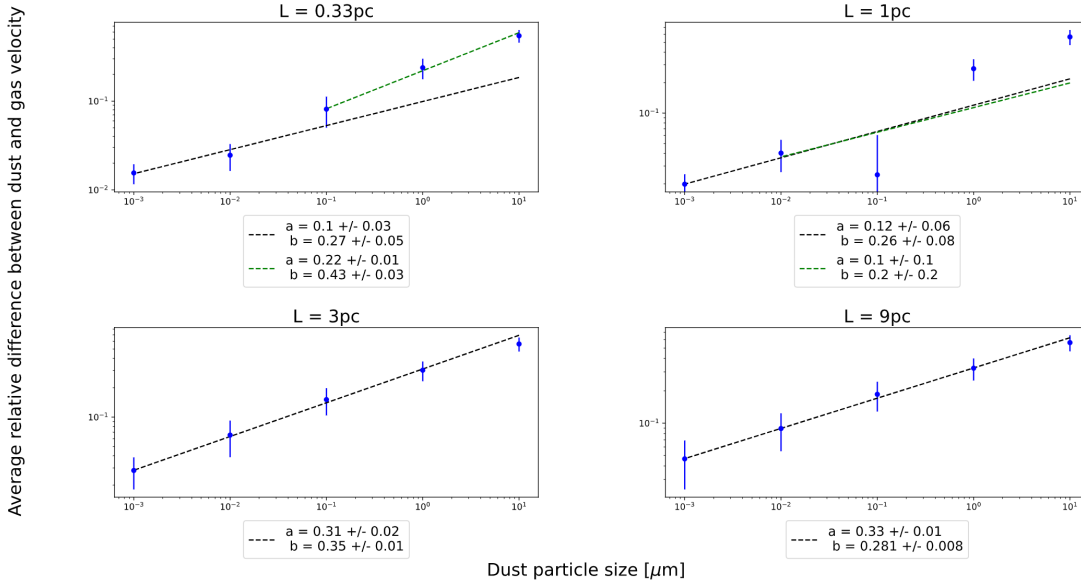

Figure 29: The average relative difference in the reference frame between the dust and gas velocity in experiments with the same sub box size, as a function of the size of the dust particles (0.001 to $10\mu m$) in the experiment, averaged over 27 sub boxes and averaged over 40 time snapshots from $t = 2.4\ t_{turn}$ to $t = 10\ t_{turn}$, with corresponding errorbars and power law fits. In the top left figure, we have the average relative difference in the reference frame between the dust and gas velocity for the mean over 27 $0.33^3 pc^3$ sub boxes, for an experiment containing dust particles of size $0.001\mu m$, $0.01\mu m$, $0.1\mu m$, $1\mu m$, and $10\mu m$ (from left to right in the figure). The upper left figure also has a dashed line corresponding to the power law fit made over the average relative difference in the reference frame between the dust and gas velocity as a function of the size of the dust particles in the experiment for the experiments of sub box size $0.33^3 pc^3$. The power law fitted is shown in the legend box. Going from the top left to the top right and then from the bottom left to the bottom right, we see figures similar to the one just described for experiments of sub box size $1^3 pc^3$, $3^3 pc^3$, and $9^3 pc^3$. The green dashed line present in the figure representing experiments of size $0.33^3 pc^3$, and $1^3 pc^3$ is a fit made over the dust particle sizes moving with a supersonic relative difference in the reference frame between the dust and gas velocity, and a single dust particle size that corresponds to a relative difference in the reference frame between the dust and gas velocity just below the supersonic regime.

difference in the reference frame between the dust and gas velocity below the supersonic velocity is to obtain a more accurate fit than by using all the average relative difference in the reference frame between the dust and gas velocity values, but without using too few values for the fit (below three values). All fits have a p value, when performing a Pearson's Chi squared test, of 0.99, except for the $L = 0.33pc$ and $L = 1pc$ fits in figure 28 to 30, which have p values of $0.70 - 0.96$ when using all of the dust particle sizes, but p values of 0.99, when using the green fits. One fit did not have a p value of 0.99 for either the fit using all the dust particle sizes and the fit only using one average difference between the dust velocity and the gas velocity above a supersonic velocity and one of subsonic velocity, namely the sub box fit for experiment size $L = 1pc$ in figure 29. The fit using all the dust particle sizes has a p value of 0.94, whereas the fit only using three average difference between the dust velocity and the gas velocity above a supersonic velocity, and one subsonic velocity, has a p value of 0.81. Looking at figure 29 we see that for a $L = 1pc$ sub box experiment the average relative difference in the reference frame between the dust and gas velocity has an odd value for the $0.1\mu m$ experiment, and the green fit using only one subsonic average relative difference in the reference frame between the dust and gas velocity, gives a worse fit than if we use all of the average relative difference in the reference frame between the dust and gas velocity values. Therefore I here chose to use all the values instead of the green fit when calculating the un-normalized average difference in the reference

Power law fits of the average relative difference between dust and gas velocity as a function of the dust particle sizes.
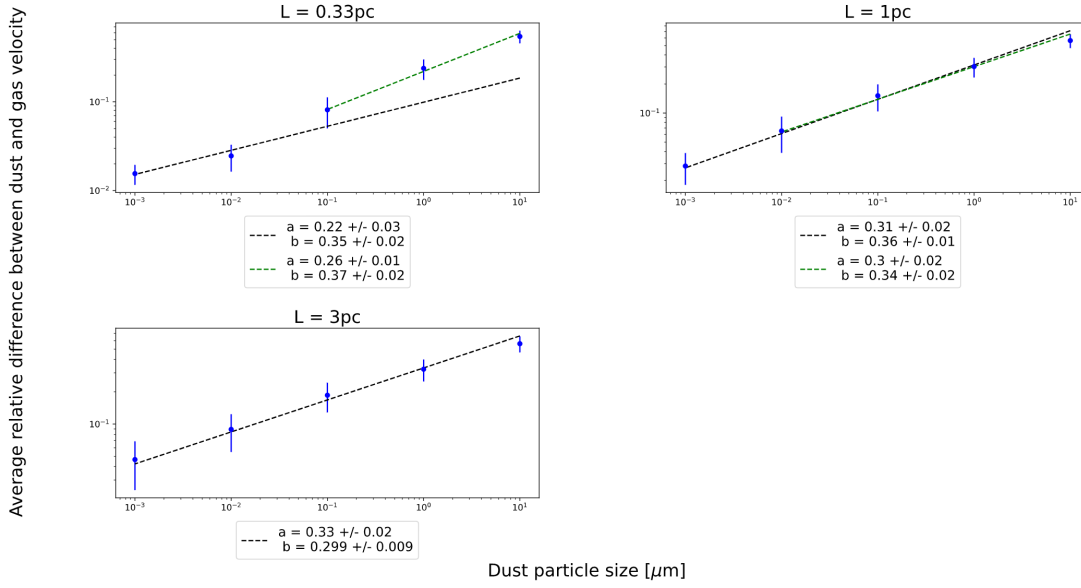

Figure 30: The average relative difference in the reference frame between the dust and gas velocity in experiments with the same sub-sub box size, as a function of the size of the dust particles (0.001 to $10\mu m$) in the experiment, averaged over 729 sub-sub boxes and averaged over 40 time snapshots from $t = 2.4$ t_{turn} to $t = 10$ t_{turn}, with corresponding errorbars and power law fits. In the top left figure, we have the average relative difference in the reference frame between the dust and gas velocity for the mean over 729 $0.33^3 pc^3$ sub-sub boxes, for an experiment containing dust particles of size $0.001\mu m$, $0.01\mu m$, $0.1\mu m$, $1\mu m$, and $10\mu m$ (from left to right in the figure). The upper left figure also has a dashed line corresponding to the power law fit made over the average relative difference in the reference frame between the dust and gas velocity as a function of the size of the dust particles in the experiment for the experiments of sub-sub box size $0.33^3 pc^3$. The power law fitted is shown in the legend box. Going from the top left to the top right and then from the bottom left to the bottom right, we see figures similar to the one just described for experiments of size $1^3 pc^3$, and $3^3 pc^3$. The green dashed line present in the figure representing experiments of size $0.33^3 pc^3$, and $1^3 pc^3$ is a fit made over the dust particle sizes moving with a supersonic relative difference in the reference frame between the dust and gas velocity, and a single dust particle size that corresponds to a relative difference in the reference frame between the dust and gas velocity just below the supersonic regime.

frame between the dust and gas velocity fit in table 5. For all other fits where it was possible to get enough values for a proper fit (for the $0.01\mu m$ and smaller fits between the average relative difference in the reference frame between the dust and gas velocity and the size of the experiment I would only have two values to make the reduced fit which would be too little), I used the fits containing one subsonic value, when calculating the un-normalized power laws in table 4 and table 5. We once again see very large uncertainties on the fits made from the mean over the 729 sub-sub boxes, due to the limited number of average relative difference in the reference frame between the dust and gas velocity values. Thus these should also here be seen as a supplement to the fits made using the entire experiment and the mean over the sub boxes.

Looking at the fits In table 4, we see a general trend of a larger average difference in the reference frame between the dust and gas velocity for larger MCs/GMCs. This means that the larger the MC/GMC we observe the larger mean v_{rms} the gas will have in the reference frame of the dust particles. Another trend to notice is the coefficient we multiply L by is larger for larger dust particles in the power law relation and falls as we look at smaller and smaller sized dust particles. The opposite is true if we look at the coefficient that L is in the power of, which goes from a value almost the same as for the mean gas v_{rms} power law relation, and then increases until it reaches a maximum value for $0.01\mu m$-sized dust particles, and then the coefficient falls in

Experiment size	Full experiment/ sub box/ sub-sub box	Average difference in the reference frame between the dust and gas velocity as a function of experiment size power law fit
$L = 0.33pc$	Full experiment	$0.19 \pm 0.02 \cdot a^{0.98 \pm 0.05}$
	Sub box	$0.30 \pm 0.02 \cdot a^{0.92 \pm 0.04}$
	Sub-sub box	$0.36 \pm 0.02 \cdot a^{0.87 \pm 0.03}$
$L = 1pc$	Full experiment	$0.22 \pm 0.04 \cdot a^{0.95 \pm 0.03}$
	Sub box	$0.16 \pm 0.08 \cdot a^{0.51 \pm 0.02}$
	Sub-sub box	$0.41 \pm 0.03 \cdot a^{0.84 \pm 0.03}$
$L = 3pc$	Full experiment	$0.23 \pm 0.03 \cdot a^{0.83 \pm 0.03}$
	Sub box	$0.42 \pm 0.03 \cdot a^{0.84 \pm 0.02}$
	Sub-sub box	$0.45 \pm 0.03 \cdot a^{0.80 \pm 0.02}$
$L = 9pc$	Full experiment	$0.32 \pm 0.03 \cdot a^{0.82 \pm 0.02}$
	Sub box	$0.45 \pm 0.02 \cdot a^{0.77 \pm 0.02}$
$L = 27pc$	Box	$0.32 \pm 0.02 \cdot a^{0.75 \pm 0.02}$
Gas	Full experiment	$1.00 \pm 0.02 \cdot L^{0.48 \pm 0.01}$
	Sub box	$1.36 \pm 0.01 \cdot L^{0.49 \pm 0.01}$
	Sub-sub box	$1.37 \pm 0.02 \cdot L^{0.50 \pm 0.01}$

Table 5: Table showing the power law fits for the average difference in the reference frame between the dust and gas velocity as a function of the experiment/sub box/sub-sub box size, for individual experiment sizes, as well as the power law fits made for the mean gas v_{rms} as a function of the experiment/sub box/sub-sub box size (figure 15), illustrated in figure 28 to 30.

value again for the $0.001\mu m$-sized dust particles. This results in the larger dust particles having a larger average relative difference in the reference frame between the dust and gas velocity and is the least affected by the size of the experiment we are looking at, and the smaller dust particles having a lower average relative difference in the reference frame between the dust and gas velocity, but are more affected by the size of the experiment size, with dust particles of size $0.001\mu m$ being a bit less affected by the size of the experiment than the dust particles of size $0.01\mu m$. The average difference in the reference frame between the dust and gas velocity is the mean v_{rms} that the gas moves towards a dust particle by, in the reference frame of the dust particle. With this in mind, what the power law fit for the large dust particles $(100 - 500\mu m)$ shows us is that in the reference frame of these particles the dust will move towards them as they travel through the MC/GMC with the same mean v_{rms} as the mean gas v_{rms} within the cloud, no matter how large a MC/GMC the large dust particles move around in. This is due to the large particles and the gas almost having no v_{rms} in common, and large dust particles $(100\mu m$ and larger) and gas inside a MC/GMC will therefore move around completely differently inside a MC/GMC. The reason for the average difference in the reference frame between the dust and gas velocity for dust particles of size 0.01 to $10\mu m$, to become smaller and smaller is that the smaller the dust grain the more it will move around the MC/GMC with the gas. This results in the mean gas v_{rms} seen from the dust particles perspective are small since the frame of reference is mostly moving around with the gas. The reason for the size of the MC/GMC having a larger and larger effect on the average difference in the reference frame between the dust and gas velocity comes from the dust particles stopping time being longer than that of the gas, so when the gas change direction the dust particles will take longer to change direction than the gas does. This effect will be pronounced in larger MCs/GMCs, where the gas has a larger volume to move around in, from equation 22. For dust particles of size $0.001\mu m$, the average difference in the reference frame between the dust and gas velocity will be even smaller than for the $0.01\mu m$, but

the effect of the size of the MC/GMC will be less for the $0.01\mu m$ sized dust particle than for the $0.001\mu m$ sized particle. This slight deviation in the increase in dependence to the size of the MC/GMC, is due to the size of the dust particle here only having a supersonic average difference in the reference frame between the dust and gas velocity for a 27^3pc^3 sized experiment. All the other sized experiments for the $0.001\mu m$ experiment has a average difference in the reference frame between the dust and gas velocity that lies below the speed of sound, deviating from the linear trend in loglog space. Therefore the $0.001\mu m$ fit between the average difference in the reference frame between the dust and gas velocity and the size of the experiment is best to ignore.

If we now instead look at table 5, we need to remember that these relations are only true for dust particles below $10\mu m$. A general trend here for the different experiment sizes is that we have an increasing average difference in the reference frame between the dust and gas velocity with increasing dust particle size. This means that if we are in the reference frame of the dust particle, the gas will have a larger mean v_{rms} for larger dust particles. This suggests that larger dust particles will have a mean v_{rms} that is very different from the mean gas v_{rms}. Looking at the power laws we see the average difference in the reference frame between the dust and gas velocity increases for larger MCs/GMCs, as the coefficient, we multiply the dust particle size a within the power law relations, takes on a larger and larger value. The effect of the size of the dust particle becomes less and less important as we go from small MCs/GMCs to larger MCs/GMCs, as the coefficient we take L to the power of, decreases. The reason for the average difference in the reference frame between the dust and gas velocity to increase with increasing experiment size is (as previously discussed), due to the stopping time for particles becoming larger and larger with an increasing experiment size, and thus the time it takes for the dust particles to change directions will be increasing with an increasing experiment size. The reason for the smaller experiment sizes to have a larger dependency on the size of the dust particle sizes is due to the stopping time also being dependent on the size of the dust particle, seen in equation 5. Looking at equation 23, we see that the average difference in the reference frame between the dust and gas velocity is proportional to the size of the dust particle and the size of the MC/GMC observed $\Delta v \propto aL$. For small MCs/GMCs L will be small and the effect of a change in dust particle size will be greater, whereas for a large MC/GMC, the size of the MC/GMC will dominate the value of the average difference in the reference frame between the dust and gas velocity, and the size of the dust particle will be less significant.

Now I wanted to explore the probabilities of having dust at different dust densities and thereby exploring what would be the most probable dust density we would see in the different experiments. I explored 5 different experiment sizes each for 6 different dust sizes, and made histograms of the different densities and their probability, both for dust and gas. The histograms can be seen in figure 31 for gas densities and figure 32 for dust densities. The histograms were made from averaging over 24 time-steps between the times 3.2 and 5.6 in code units. These times were chosen in order for the experiments to have enough time to have reached the physical equilibrium in velocity where the gas and dust in the experiment moves like in a physical MC/GMC, and runs for a bit more than 3 turn over times, to have time to average the density distributions over. The densities got $1.1 \cdot 10^{-10}$ added to the values, in order to get them above the noise.

I made the two histograms using pythons `hist` function inside the python library `matplotlib`. Here I flattened the data into a 1-dimensional array of the dust and gas densities, and took the 10-logarithm of the values. I used 200 bins, in order to get a proper resolution without overexposing the data. In order to get the averaged PDF over the 24 time-steps, I added up the values of the histogram bins (`hist(...)[0]`) of the 24 histograms and then divided the summed bin values by the number of time steps (24). The gas PDFs (figure 31), has the form of a log-normal plot, with some perturbations for the lower densities, due to the lower densities
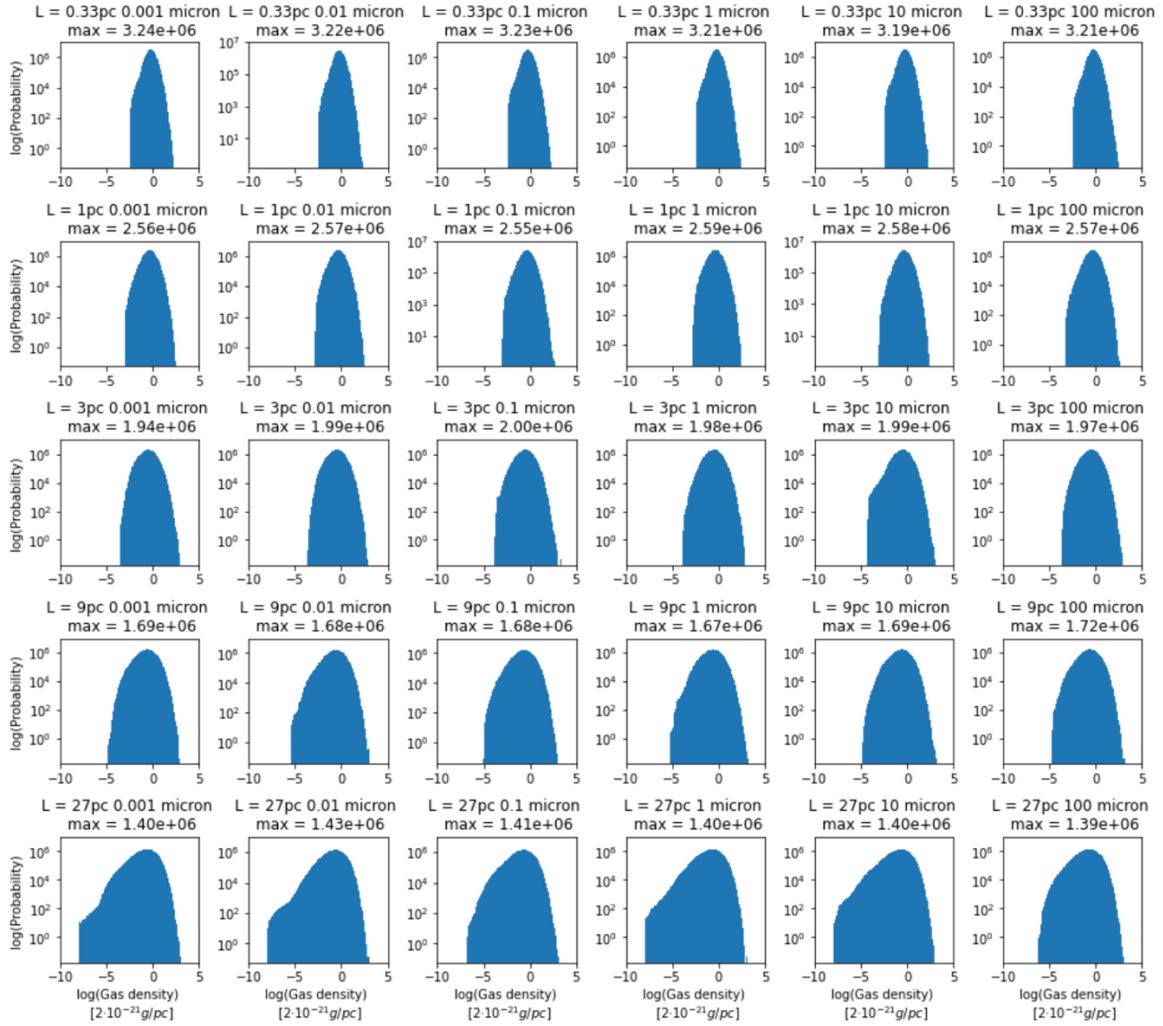
Figure 31: The probability density functions (PDF) of 30 experiments of size $0.33^3 pc^3$, $1^3 pc^3$, $3^3 pc^3$, $9^3 pc^3$, and $27^3 pc^3$, and 6 different dust sizes (namely $0.001\mu m$, $0.01\mu m$, $0.1\mu m$, $1\mu m$, $10\mu m$, and $100\mu m$), and averaged over the time $3.2 - 5.6$ in code units. On the x-axis, we have the 10-logarithm of the gas density and on the y-axis, we have the probability of finding a gas particle inside a region of that gas density. The different experiment sizes are seen from the top to the bottom with the $0.33^3 pc^3$ experiment being in the top 6 subplots, and the $27^3 pc^3$ being at the bottom. The different dust particle sizes used in the experiments are seen from left to right, the furthest to the left being $0.001\mu m$ and the one furthest to the right being the $100\mu m$ experiment.

representing voids. Voids take up a large volume, and therefore there exist very few of them inside an experiment. Since there are only a few voids we get a small sample size of low densities and thus a large noise in the voids. This noise is what we see as fluctuations in the left side of the gas density PDFs. The log-normal form shows that the gas is evenly distributed in the different experiments for the different dust sizes used in the experiment, having most of the density in the bulk with a small amount in high density regions and a small amount in low density regions. One feature we can notice is the width of the PDFs changing with different experiment size, meaning that the variance of the dust motion is larger for larger experiment sizes, and the probability of finding gas in lower- and higher gas density regions are higher for the experiments with large experiment sizes than the experiments with a small experiment size. This is due to the volume that the gas can move around in, has become larger in the larger experiments, so that the gas is spread out in a larger volume and is therefore present in a broader variety of densities.
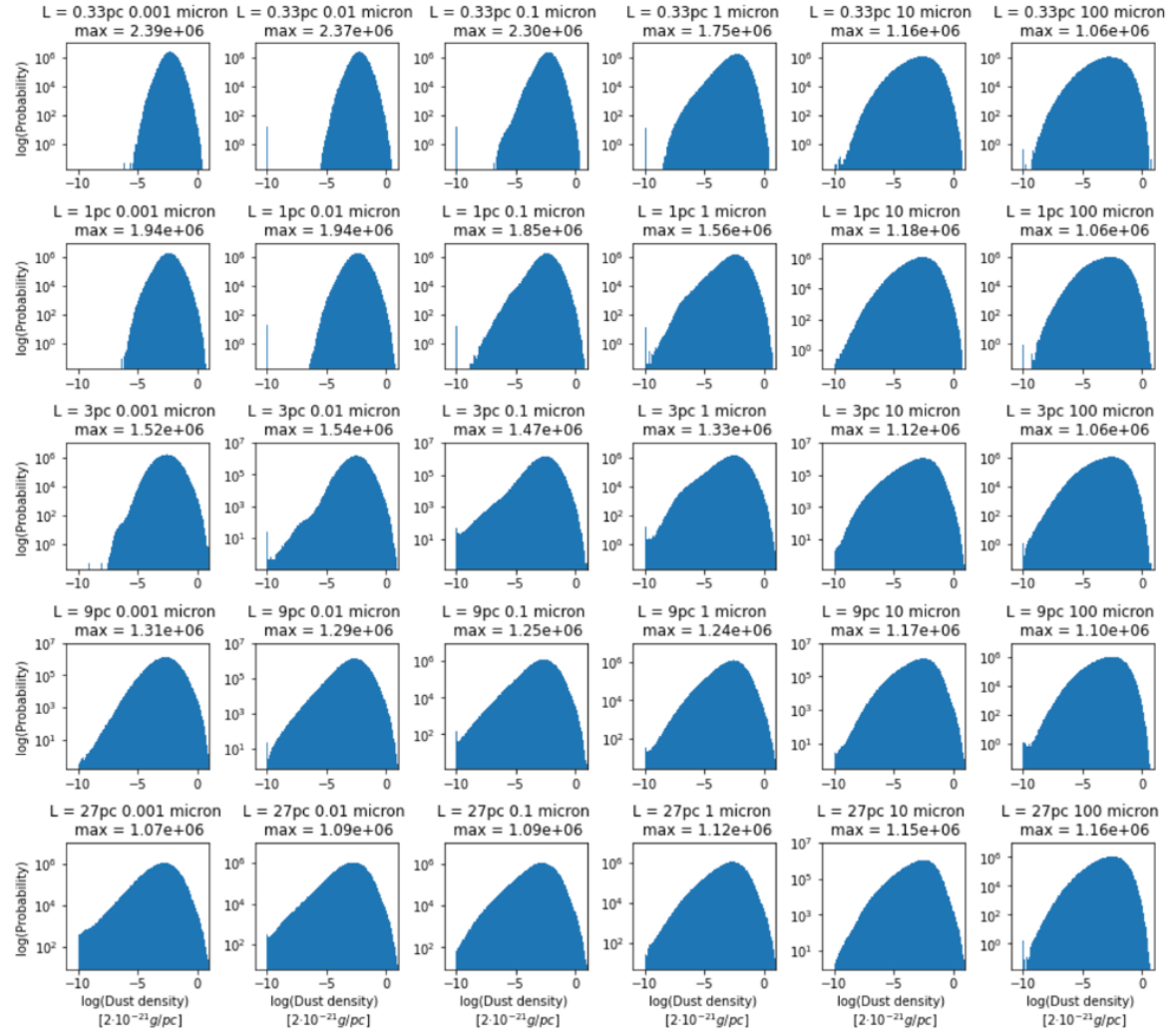
Figure 32: The probability density functions (PDF) of 30 different experiments of size $0.33^3 pc^3$, $1^3 pc^3$, $3^3 pc^3$, $9^3 pc^3$, and $27^3 pc^3$, and 6 different dust sizes (namely $0.001\mu m$, $0.01\mu m$, $0.1\mu m$, $1\mu m$, $10\mu m$, and $100\mu m$), and averaged over the time $3.2 - 5.6$ in code units. On the x-axis, we have the 10-logarithm of the dust density and on the y-axis, we have the probability of finding a dust particle in a region of that dust density. The different experiment sizes are seen from the top to the bottom with the $0.33^3 pc^3$ experiment being in the top 6 subplots, and the $27^3 pc^3$ being at the bottom. The different dust particle sizes used in the experiments are seen from left to right, the furthest to the left being $0.001\mu m$ experiment and the one furthest to the right being the $100\mu m$ experiment.

Now looking at the dust particle PDFs in figure 32, we see that they have a log-normal right side, and an exponential left side (since it is linear in a loglog plot). The lognormal distribution on the right side means that at larger dust densities the dust is evenly distributed with most of the dust being in the bulk with a certain dust density and a small amount at high dust densities. The left sides exponential curve, means that at lower densities we see an expansion. We see an expansion, since an even distribution would have been log normal, with a step fall in the probability of having dust at low densities, and what we instead see is a slower decrease in probability towards lower densities through a linear trend. This gives a higher probability of dust being at lower densities than if we have had a log normal curve. Thus we see dust moving away from the high dust density regions towards lower dust density regions, as a function of time. Having this in mind we would expect dust to move from high-density regions and in half a dynamic time, move to a lower dust density region. This means that the dynamical dust timescale is longer than the dynamical gas time scale. The large regions of a medium dust density in figure 5 is due to the dust being on its way inside another region. Meaning that the only way to uphold

a region of high dust density is to have a large convergence in the velocity field, otherwise the dust will move from high dust density fields to low dust density fields.

4.2   Discussion

The power law fits in table 3, helps us to get an understanding of how fast dust particles of different size move around inside different sized MCs/GMCs, and the power law fits in table 4 and 5, helps us to get an understanding of how dust particles move compared to the gas for different dust particle sizes, in different sized MCs/GMCs. Why it is so important to understand the dust dynamics is the fact that stars are created when a large overdensity of gas develops inside a MC/GMC, and if enough dust is present inside the protoplanetary disc in the protostellar environment, planets can be formed. A way to get enough dust inside these discs is if dust is carried with the gas through the ISM into the discs. In order for the dust to become concentrated inside these overdense protoplanetary disc, the dust particles' stopping length needs to be short enough to be stopped inside the disc. As we have seen, larger dust particles of a sizes above approximately $50\mu m$, are mostly decoupled from the gas, having a stopping time longer than the size of the MC/GMC, and the likelihood of these dust particles to contribute to the formation of protoplanetary discs are low. We have also seen that the increase in decoupling already starts to be significant for $1\mu m$ particles, which means that dust of size $1\mu m$ and $10\mu m$, will still move around with the gas predominantly, but not all of the dust will concentrate in the same regions as the gas. For dust particles below $50\mu m$, we have seen that the average relative difference in the reference frame, will be close enough to 0 for all different MC/GMC sizes, for dust particles to move predominantly with the gas, thereby being caught in gas overdensities, and contribute to the creation of protoplanetary discs. For the smaller dust particles below a size of $10\mu m$, the larger the MC/GMC we look at, the more the size of the dust particle becomes irrelevant for the difference in mean v_{rms} between dust and gas. This suggests that if we observe large MCs/GMCs, we will see a wider range in the size of dust particles being transported by the gas from the ISM to presellar systems, which means that larger MCs/GMCs will have a larger dust particle transport from the ISM to prestellar systems due to coupling with the gas than smaller MCs/GMCs, and there could be a larger probability of dust enriched protoplanetary disc formation in larger MC/GMC than in smaller. The only way for larger dust particles above a size of $100\mu m$ to contribute to protoplanetary disc formation is if they break apart, and thereby reduce in size, or if they move directly into an overdensity and thereby accumulating enough mass in front of them to be stopped.

From figure 6, 5, 9, 10, and 11, it seems probable that the way dust travels inside MCs/GMCs is collectively in coherent groups that form overdensities when two groups crosses paths. If these regions where the two groups of coherent dust meet, are where protoplanetary discs are, it will contribute to the conditions needed inside them for planet formation. For dust particles of sizes smaller than about $56\mu m$, we see that the overdensities in dust will mostly be where overdensities of gas is also present. For larger dust particles, the overdensities will mostly be outside of overdense gas regions. From the probability density functions in figure 31 and 32, we see an expansion of dust particles away from overdense dust regions, towards underdense dust regions. One condition that can work against this accumulation of dust from low density regions to higher dust density regions being a large velocity divergence in the velocity field.

Looking at (Liubin Pan, Paolo Padoan 2018) [45], Pan and Padoan found a connection between the v_{rms} of a turbulent flow and the v_{rms} of a particle traveling in that turbulent flow, given by

$$v' = u' \left(\frac{T_L}{T_L + \tau_p} \right)^{1/2} . \tag{73}$$

Here, v' is the v_{rms} of the particle, u' is the v_{rms} of the turbulent flow, T_L is the turn over time for the turbulent flow, and τ_p is the stopping time of the particle. From equation 73, we see that if the stopping time of the particle τ_s is small the turbulent flow and the particle will have the same velocity. This is also what we have found in my thesis, with dust particles with a small stopping time, i.e. a small size, having the same v_{rms} as the gas. The larger the stopping time of the particle becomes, the smaller the particles v_{rms} becomes, which is also what we see in the results of this thesis. When we looked at the power law relations between the mean dust v_{rms}, we saw that for larger particles (with a higher stopping time), they will have lower v_{rms} than particles of a smaller size. If we want to see what equation 73 predicts for the difference in the reference frame between the dust and gas velocity, we can subtract u' from v' as

$$v' - u' = u' \left(\left(\frac{T_L}{T_L + \tau_p} \right)^{1/2} - 1 \right) . \tag{74}$$

In equation 74, we see that when $\tau_p \to 0$ the difference in the reference frame between the dust and gas velocity goes towards 0, which is also what we see in the results of this thesis. If we instead look at $\tau_p \to \infty$, the difference in the reference frame goes towards u', which is also what we see in the results of this thesis. Thus, the results from this thesis, is in accordance with the results of Pan and Padoan (2018).

4.3   Reevaluating results

Now it seems appropriate to look at how accurate the power laws, just found, really are, and thereby explore some of the limitations of the results found. In order to do this, we can look at how big an impact the resolution has on the results. Since my results have been limited to a resolution of $360 \times 360 \times 360$ cells, it is interesting to see how big (if any) difference there would have been in my results, had I only had resources to obtain a third of that resolution, namely $120 \times 120 \times 120$ cells, which can illustrate the importance of resolution. I have therefore looked at the relationship between the normalized mean dust v_{rms} for an experiment with a resolution of $360 \times 360 \times 360$ cells and an experiment of resolution $120 \times 120 \times 120$ cells, with different dust particle sizes of $0.001\mu m$, $0.01\mu m$, $0.1\mu m$, $1\mu m$, $10\mu m$, and $100\mu m$, both over the entire experiment, the mean over 27 sub boxes, and the mean over 729 sub-sub boxes. The result is shown in figure 33.

In figure 33 we see that comparing the normalized mean dust v_{rms} for a $0.33^3 pc^3$ and $1^3 pc^3$ experiment with the two different resolutions, the values are similar when looking at the entire experiment and the mean over the sub boxes, with a slight difference between the normalized mean dust v_{rms} between the two resolutions for dust particles of size $100\mu m$ and larger. If we compare the normalized mean dust v_{rms} for a $0.33^3 pc^3$ and $1^3 pc^3$ experiment with the two different resolutions, the values are similar when looking at the mean over the sub-sub boxes for small dust particle sizes. This similarity continues until a dust particle size of $1\mu m$, where the normalized mean dust v_{rms} starts to be significantly different between the two resolutions, with a difference of approximately 3%. This shows that there only is a small error due to resolution for the two different resolutions when looking at the normalized mean dust v_{rms} over the entire experiment and the mean over the 27 sub boxes. But when we look at the normalized mean dust v_{rms} over the sub-sub boxes, we see a considerable difference between the two resolutions. We can also look at the average relative difference in the reference frame plot with the same two
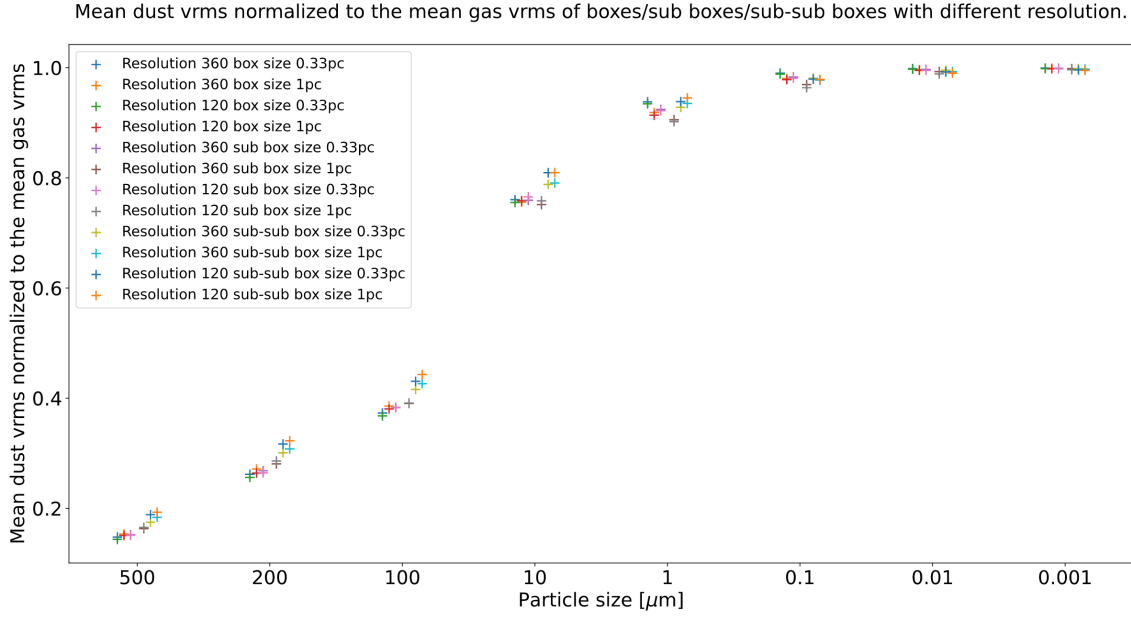
Mean dust vrms normalized to the mean gas vrms of boxes/sub boxes/sub-sub boxes with different resolution.

Figure 33: The normalized mean dust v_{rms} as a function of the dust particle size for experiments with resolution $360 \times 360 \times 360$ cells, and $120 \times 120 \times 120$ cells and experiment sizes of $0.33^3 pc^3$ and $1^3 pc^3$, created by taking the mean over the entire experiment, over 27 sub boxes, and 729 sub-sub boxes. The normalized mean dust v_{rms} is made from 40 snapshots between the times $t = 2.4\ t_{turn}$ to $t = 10\ t_{turn}$ and divided with the mean gas v_{rms} made from an average over the same 40 time snapshots.

different resolutions, seen in figure 34.

Average relative difference between dust and gas velocity of boxes/sub boxes/sub-sub boxes with different resolution.
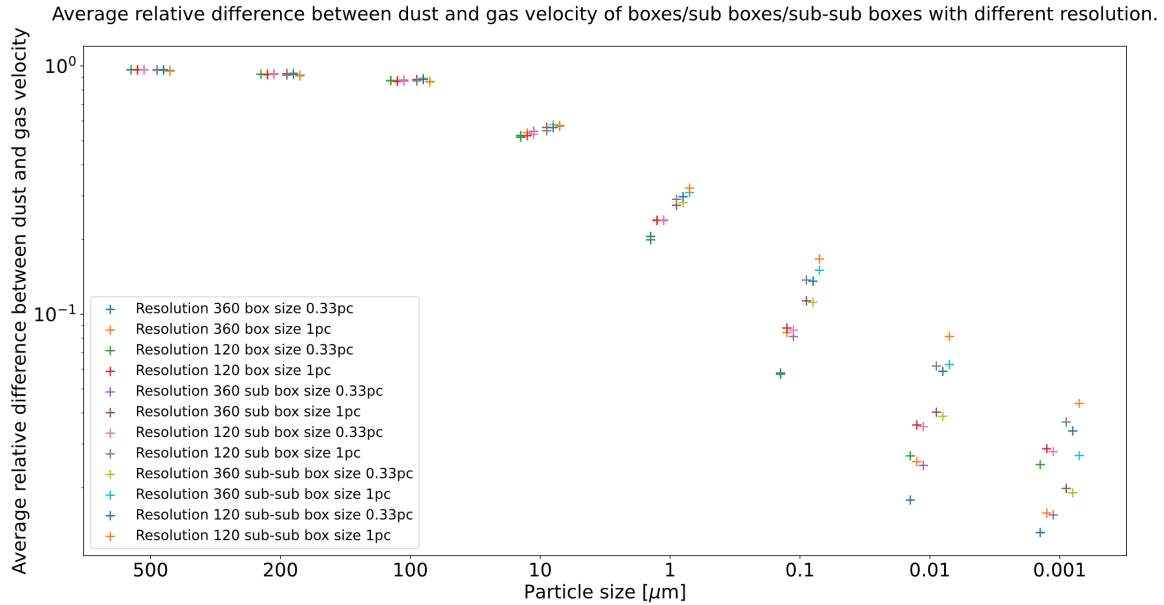

Figure 34: The average relative difference in the reference frame between the dust and gas velocity as a function of the dust particle size for experiments with a resolution of $360 \times 360 \times 360$ cells, and $120 \times 120 \times 120$ cells and experiment sizes of $0.33^3 pc^3$ and $1^3 pc^3$, created by taking the mean over the entire experiment, over 27 sub boxes, and 729 sub-sub boxes. The average relative difference in the reference frame between the dust and gas velocity is made from 40 snapshots between the times $t = 2.4\ t_{turn}$ to $t = 10\ t_{turn}$.

In figure 34, we see the same small effect of the resolution on the results as in figure 33 for the normalized mean dust v_{rms} over the entire experiment and the mean over 27 sub boxes, and we

can thus conclude that there is a small effect on the results due to the resolution when looking at the entire experiment and the mean over the sub boxes. We also see a larger effect of the resolution on the normalized mean dust v_{rms} when looking at the mean over 729 sub-sub boxes. We can thereby conclude that the sub-sub box results are considerably affected by the resolution.

Another limit on our results we can look at is the limit due to the v_{rms} that is possible to reach in the confinements of the different sized experiments. To explain further what is meant here, we know that looking at an experiment of size $0.33^3 pc^3$ where we look at the mean dust v_{rms} of the entire experiment, there is a maximum velocity that the dust will be able to reach since the dust only has the $0.33^3 pc^3$ volume to move around in. If we instead look at the mean v_{rms} of a sub box with size $0.33^3 pc^3$ of an experiment of size $1^3 pc^3$, the dust will be able to move around in a volume of size $1^3 pc^3$, and therefore these dust particles will have had the possibility of having a larger v_{rms} since they have a larger volume of building up a larger velocity inside. In order to explore this effect, we can compare the normalized mean dust v_{rms} as a function of dust particle size when looking at the mean over the entire experiment, to the mean over the 27 sub boxes of a larger experiment, and to the mean over the 729 sub-sub boxes of an even larger experiment. This comparison can be seen in figure 35. We can also compare the average relative difference in the reference frame between the dust and gas velocity when looking at the entire experiment, to the 27 sub boxes of a larger experiment, and to the 729 sub-sub boxes of an even larger experiment, which is done in figure 36.
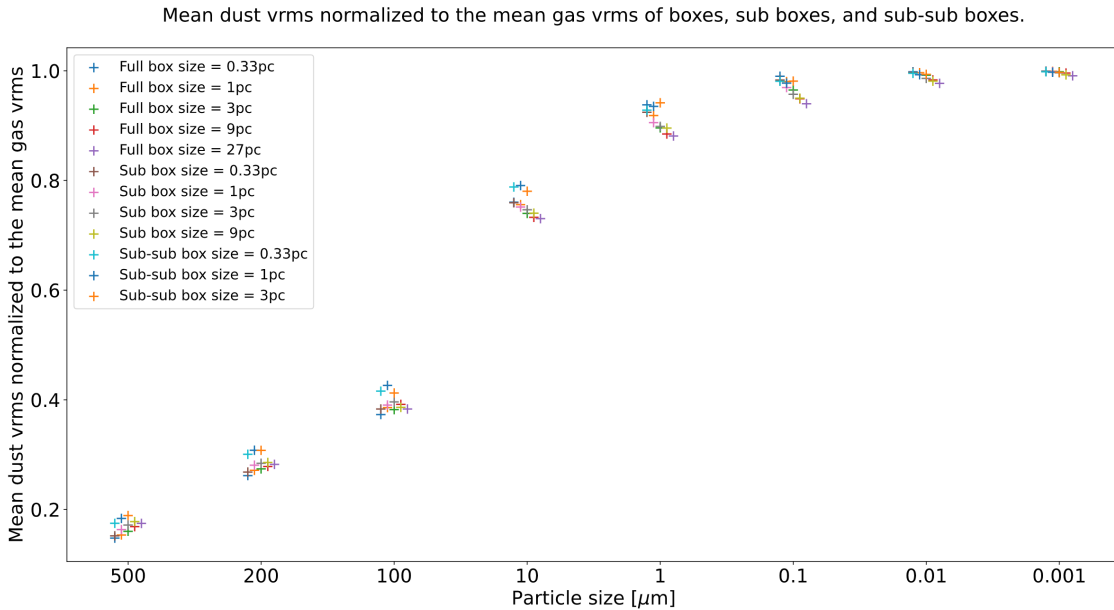

Figure 35: The normalized mean dust v_{rms} as a function of the dust particle size when looking at the entire experiments of size $0.33^3 pc^3$, $1^3 pc^3$, $3^3 pc^3$, $9^3 pc^3$, and $27^3 pc^3$, as well as the normalized mean dust v_{rms} over the 27 sub boxes of sub box size $0.33^3 pc^3$, $1^3 pc^3$, $3^3 pc^3$, $9^3 pc^3$, and the normalized mean dust v_{rms} over the 729 sub-sub boxes of sub-sub box size $0.33^3 pc^3$, $1^3 pc^3$, $3^3 pc^3$. The normalized mean dust v_{rms} is made from 40 snapshots between the times $t = 2.4\ t_{turn}$ to $t = 10\ t_{turn}$.

If we start by looking at figure 35, we see that the normalized mean dust v_{rms} has the same value of around 1 for the smaller dust particles, independent of whether we are looking at the mean over the entire experiment, the mean over the 27 sub boxes or the mean over the 729 sub-sub boxes. Starting at around a dust particle size of $1\mu m$ we see the sub-sub box value start to have a larger normalized mean dust v_{rms} than the mean over the entire experiment and the mean over the sub boxes. This trend continues until the $100\mu m$-sized particles, where the sub-sub box has a $10\% - 12\%$ larger normalized mean dust v_{rms} than the results from the mean over the
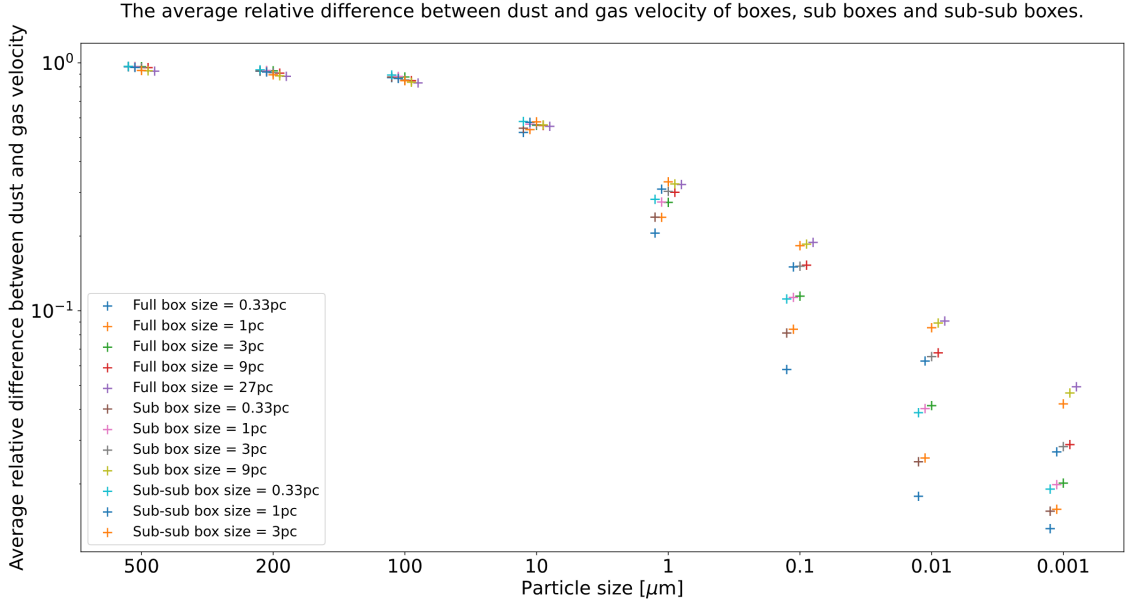
Figure 36: The average relative difference in the reference frame between the dust and gas velocity as a function of the dust particle size, when looking at the entire experiments of size $0.33^3 pc^3$, $1^3 pc^3$, $3^3 pc^3$, $9^3 pc^3$, and $27^3 pc^3$, as well as the normalized mean dust v_{rms} over the 27 sub boxes of sub box size $0.33^3 pc^3$, $1^3 pc^3$, $3^3 pc^3$, $9^3 pc^3$, and the normalized mean dust v_{rms} over the 729 sub-sub boxes of sub-sub box size $0.33^3 pc^3$, $1^3 pc^3$, $3^3 pc^3$. The average relative difference in the reference frame between the dust and gas velocity is made from 40 snapshots between the times $t = 2.4\ t_{turn}$ to $t = 10\ t_{turn}$.

sub boxes and the entire experiment. We see that the mean over the sub boxes also has a larger normalized mean dust v_{rms} when compared to the mean over the whole experiment, but this is a lot less significant (around 3%). Thus, the effect from the size of the volume that the dust particles can build up a velocity inside has a large effect when looking at the mean of the dust v_{rms} over the sub-sub boxes compared to when we are looking at the normalized mean dust v_{rms} over the entire experiment, and over the sub boxes. This makes sense when we think about a $500 \mu m$ dust particle traveling inside an experiment with a size of $3^3 pc^3$, which has a v_{rms} that is almost completely independent of the dust velocity. This dust particle will have the ability to build up a large velocity and if we then look inside a section of this experiment with a size of $3^3 pc$ the mean v_{rms} we will observe will be significantly larger than if a dust particle of the same size only had a $0.33^3 pc$ volume to move around in. For the average relative difference in the reference frame between the dust and gas velocity in figure 35, we see for experiments containing dust particles of size $0.1 \mu m$ and $1 \mu m$ the sub-sub boxes having a significantly different value than the sub boxes, which again has a significantly different value than for the entire experiment. The difference between the average relative difference in the reference frame between the dust and gas velocity for the sub-sub boxes and the entire experiment is $37\% - 48\%$, and between the sub boxes and the entire experiment, the difference in average relative difference in the reference frame between the dust and gas velocity is between $24\% - 29\%$. We, therefore, have significantly different results depending on whether we observe the results from an entire (but smaller) experiment, compared to if we take the mean over the sub boxes or sub-sub boxes of larger experiments.

5 Future work

Since most GMCs have sizes of between $20 - 200 pc$ it would be appropriate to analyze an experiment of a larger GMC. An interesting GMC to simulate would be one of size $100^3 pc^3$, since an experiment of that size would replicate a slice of the Milkyway and would give a good un-

derstanding of several different GMC in a larger context. The most accurate result would be found by taking the mean of the sub-sub boxes of the experiments. This could roughly simulate taking the mean over different GMCs of the same size. Another reason to look at the mean over sub-sub boxes of size $100^3 pc^3$ instead of the whole experiment is the effects of the artificial driving in the experiment, which will not be as profound, and will therefore replicate the turbulent cascade inside a real GMC more accurately. We see in the analysis made in the "Reevaluating Results" section, that a higher resolution is important if we wish to look at sub and sub-sub sections of GMCs, so we would need a much higher resolution than used in my experiments in order to get a accurate result from such a large experiment. Since the computer memory of a single computational node needed for this kind of experiment was not available during my thesis, it would be something that could be further explored. A higher resolution and more memory available would also allow experiments where we look at a wider range of GMCs, and thereby have more data for the analysis of the power law relationships between the dust v_{rms} and the size of the dust particle and the size of the GMC.

In my experiments, I had no gravitation and magnetic fields, which is a big part of the dynamics of GMCs, and including these would thus contribute to a more precise experiment of the actual processes happening inside GMCs. Having overdensities in the experiment simulating prestellar cores would be an interesting parameter to add to the experiments, exploring the effect of their gravitational pull on dust particles. Additionally, another interesting property to add to the experiments would be sandblasting by small dust particles on larger dust particles, which would also give a more realistic representation of molecular clouds, as well as adding sources of dust particles in the ISM like asymptotic giant branch (AGB) stars adding diffuse dust or supernovas adding high velocity dust to the experiment. The tools needed to make experiments including these properties were not available during my thesis work. Adding these to the experiments run for this project was outside the scope of this thesis. Another effect present in real GMCs but absent in my thesis is the coagulation of particles, and collisions of particles. These effects are also crucial for the dynamics of dust particles within real GMCs and are obvious points of interest when revisiting the dynamics of dust particles within the ISM.

Running a simulation applying the above suggestions would give a more realistic GMC to study, giving a more accurate understanding of the relationship between the mean dust v_{rms} and the size of the GMC we observe. Examining the more realistic mean dust v_{rms} in different sized GMCs would give an indication of the accuracy of the relations found in this thesis. The Larson relations have been found to differ greatly in the universe depending on the GMCs observed, and thus this might also be true for the mean dust v_{rms}. An understanding of the other parameters that might also go into the determination of the mean v_{rms} of dust and the average difference in the reference frame between the dust and gas velocity inside GMCs, would also help us to understand the dynamics of dust even further. These parameters could also be found using more realistic GMCs. Investigating fragmentation from dust particles would be a great way to further explore how the dynamics of dust particles in the ISM can create initial conditions for protoplanetary disc formation, and thereby find the dynamical distribution of dust particle sizes in GMCs. This knowledge of how dust particles fragment, would also give us a better indication of whether a $500 \mu m$ particle has a probability of contributing to the formation of protoplanetary discs due to its probability of fragmenting being very high, and it is likely that such particles will fragment and their dust mass will follow the gas more closely, in the form of smaller particles.

6 Conclusions

In this thesis, the DISPATCH framework has been used with the HLLC hydrodynamical solver RAMSES, to perform experiments simulating MCs/GMCs of different sizes. The experiments

replicated dust and gas movement and the influence of gas on dust through friction inside MCs/GMCs of sizes $0.33^3 pc^3$, $1^3 pc^3$, $3^3 pc^3$, $9^3 pc^3$ and $27^3 pc^3$, looking at dust particles of sizes from $0.001\mu m$ to $500\mu m$.

1. The experiments show an expected correlation between the size of dust particles and the amount of coupling to the gas flow, where smaller dust particles are more coupled to the gas flow than larger dust particles. The size of dust uncoupled from the gas, was calculated to be approximately $50\mu m$. This is in agreement with the experiments where dust stops being completely coupled to the gas once it has a size between $1\mu m$ and $100\mu m$ in diameter. This suggests that particles of size $\geq 100\mu m$ will on average not be stopped inside the confinements of the MC/GMC observed, for the experimental setup in this thesis. This is due to their stopping length being larger than the experiment length, and a transition from being completely coupled to the gas, to becoming mostly decoupled starting to happen for dust particles of size $1\mu m$. A latency on the dust's reaction to a change in the gas movement can also be seen when looking at the v_{rms} of dust and gas inside the experiments. Here the dynamical time of the dust is larger than that of the gas, and it, therefore, takes longer for dust, compared to the gas, to change directions due to its correlation with the gas. This latency increases with dust size. It is found that even though larger dust particles are mostly decoupled from the gas, the gas still has an effect on the large dust particles through friction, which over a couple of turn over times gives rise to overdense dust regions to form, mostly outside the regions of overdense gas.

2. The simulation of a $1^3 pc^3$ MC/GMC also showed that the velocity dispersion is largest where the dust density is the largest no matter what dust particle size is being observed. The observation of dust accumulating in filaments even for large dust particle sizes over time, suggests that dust moves in coherent groups, even for particle sizes where friction relative to the gas is small. The regions of overdensities in dust will then be present where two or more coherent groups of dust cross paths.

3. The relation between the mean dust v_{rms} and the size of the MC/GMC looked at is found to follow a power law trend, such as the relationship between the mean gas v_{rms} and the MC/GMC size found in the first Larson relation. A different power law relation is found for different dust particle sizes. The power law relationship between the mean dust v_{rms} and the size of the MC/GMC observed shows an increasing mean dust v_{rms} with an increasing MC/GMC size, like the first Larson relation. As a result of dust particles being coupled to the gas, dust particles $\leq 0.01\mu m$ have the same relation between the mean dust v_{rms} and the size of the MC/GMC as the first Larson relation. For dust particles of size $\geq 200\mu m$, the power law between the mean dust v_{rms} and the size of the MC/GMC is found, inside the uncertainties, to have a larger exponent than the exponent in the first Larson relation inside the MCs/GMCs. The dust of size $\geq 200\mu m$ is, therefore, more affected by the size of the MC/GMC than the gas. Looking at particles of size $\leq 100\mu m$ we see that the exponent of the mean dust v_{rms} power law fit is, inside the uncertainties, the same as for the mean dust v_{rms}. Large dust particles are more affected by a change in the size of the MC/GMC observed due to large dust particles having a stopping length that is longer than the length of the MC/GMC observed. They will therefore not be stopped inside the cloud due to the friction caused by the gas in the MC/GMC. A larger MC/GMC size will mean a smaller mean gas density and the larger particles will be less affected by the friction due to interactions with the gas. Smaller particles of sizes $< 100\mu m$ have a stopping length less than that of the experiment size and will therefore be stopped inside the experiment, making the size of the experiment have the same effect on them as the gas. The coefficient multiplied by the size of the cloud L in the power law has a decreasing value for an increasing dust particle size, until $0.01\mu m$ where the coefficient is the same as for the mean gas v_{rms} power law fit. This causes the mean dust v_{rms} for particles $> 0.01\mu m$

to be less than the mean gas v_{rms}, due to the particles effectively speaking being "more massive" than the gas.

4. Looking at the average difference between the dust velocity and the gas velocity in the reference frame of the dust particle, a power law relation is found to exist between the average difference between the dust velocity and the gas velocity and the size of the MC/GMC observed. This relation also extends between the average difference between the dust velocity and the gas velocity as well as the size of the dust particle observed, when looking at dust particles of size $\leq 1\mu m$. With a fixed dust particle size the power law relation between the average difference between the dust and gas velocity and the size of the MC/GMC is found to increase in the average difference between the dust velocity and the gas velocity for an increasing MC/GMC size. It is found that the average difference between the dust velocity and the gas velocity is almost equivalent to the mean gas v_{rms} for particles of size $\geq 100\mu m$. This is expected since dust particles of these sizes are mostly decoupled from the gas and thus have a completely different mean v_{rms}. For dust particles of size $\leq 10\mu m$, the average difference between the dust velocity and the gas velocity is found to have a decreasing value going towards smaller dust particles, where dust particles will be more coupled to the gas and therefore the mean gas v_{rms} seen from the dust particles frame of reference will be less. The average difference between the dust velocity and the gas velocities dependency on the size of the MC/GMC increases towards smaller dust particles. This can be explained by the smaller dust particles almost having the same mean v_{rms} as the gas, and thus the average difference between the dust velocity and the gas velocity will be small for small dust particles and as the size of the MC/GMC increases so does the mean v_{rms} of the gas as well as the stopping time of the dust particles. This increase in stopping time delays the dust particles when changing directions with the gas. They will therefore change directions with an increasing delay as the size of the MC/GMC chosen to be observed increases.

5. For the power law relationship between the average difference between the dust velocity and the gas velocity as well as the size of the dust particles for dust particles of size $\leq 1\mu m$, and having a fixed MC/GMC size, it is found that the average difference between the dust velocity and the gas velocity is decreasing with increasing MC/GMC size. It is also found that the average difference between the dust velocity and the gas velocity became more dependent on the size of the dust particle for smaller MCs/GMCs. This is due to the stopping time also being dependent on the size of the dust particle observed, and an increase in stopping time will result in the mean dust v_{rms} deviating further from the mean gas v_{rms}, and thereby resulting in a larger average difference between the dust velocity and the gas velocity. Since the stopping time is also affected by the size of the MC/GMC observed, the smaller MC/GMC will be more affected by a change in the size of the dust particle observed, whereas for large MCs/GMCs, the size of the MC/GMC will dominate the value of the stopping time, and a change in the dust particle size will be less significant.

6. Looking at 5 different experiment sizes between $0.33^3 pc^3$ and $27^3 pc^3$, and 6 different dust particle sizes between $0.001\mu m$ and $100\mu m$, the probability density function of the dust density as compared to the gas probability density function, shows the gas has an even distribution in the experiments. Most of the gas has a density near the average density and a small fraction of gas in higher and lower density regions. The distribution of dust in the experiments is mostly in the bulk, with a small fraction of the dust being in high density regions and with an expansion-like behavior for the dust in low density regions. This suggests that dust inside high dust density regions tends to expand into regions of lower dust density unless there is a large velocity convergence in the velocity field, working against the expansion.

Bibliography

[1] Author: Woong-Tae Kim, Eve C. Ostriker, and James M. Stone, Title: Magnetorotationally driven galactic turbulence and the formation of giant molecular clouds, Published: September 2 2003, Publisher: The Astrophysical Journal, 599:1157–1172

[2] Author: William W. Roberts, Jr., and Glen R. Stewart, Title: The role of orbital dynamics and cloud-cloud collisions in the formation of giant molecular clouds in global spiral structures, Published: August 25 1986, Publisher: The Astrophysical Journal, 314:10-32

[3] Author: Frank H. Shu, Title: Star Formation in Molecular Clouds , Published: 1985, Publisher: The Milky Way Galaxy pp 561-566

[4] Author: D. S. Mathewson, P. C. van der Kruit, and W. N. Brouw, Title: A high resolution radio continuum survey of M51 and NGC 5195 at 1415 MHz, Published: July 30 1971, Publisher: Astronomy & Astrophysics

[5] Author: Frank H. Shu, Fred C. Adams, and Susana Lizano, Title: Star formation in molecular clouds: observation and theory , Published: 1987, Publisher: Astronomy & Astrophysics

[6] Author: Christopher F. McKee and Eve C. Ostriker, Title: Theory of Star Formation , Published: 22 September 2007, Publisher: Astronomy & Astrophysics

[7] Author: Jeffrey G. Mangum, Title: Encyclopedia of Physical Science and Technology (Third Edition), Published: 2003, Publisher: Elsevier Science Ltd., Page: 853-871

[8] Author: Jack J. Lissauer, Title: Planet formation, Published: 1993, Publisher: Ahnu. Rev. Astron. Astrophys. 1993.31: 129-74

[9] Author: A. Wolszczan & D. A. Frail, Title: A planetary system around the millisecond pulsar PSR1257 + 12, Published: 09 January 1992, Publisher: Nature volume 355, pages: 145–147(1992)

[10] Author: Jack J. Lissauer, Rebekah I. Dawson & Scott Tremaine , Title: Advances in exoplanet science from Kepler, Published: 17 September 2014, Publisher: Nature volume 513, pages336–344

[11] Author: Brice-Olivier Demory, David Ehrenreich, Didier Queloz et. al., Title: Hubble Space Telescope search for the transit of the Earth-mass exoplanet α Centauri B b, Published: 29 April 2015, Publisher: Monthly Notices of the Royal Astronomical Society, Volume 450, Issue 2

[12] Author: Elisabeth R. Newton, Andrew W. Mann, Benjamin M. Tofflemire, et. al., Title: TESS Hunt for Young and Maturing Exoplanets (THYME): A Planet in the 45Myr Tucana–Horologium Association, Published: July 23 2019, Publisher: The Astrophysical Journal Letters, 880:L17 (15pp)

[13] Author: Kristen Walbolt, Title: Exoplanet exploration Planets beyond our solar system, https://exoplanets.nasa.gov/what-is-an-exoplanet/overview/, Last Updated: December 3, 2020

[14] Author: Jonathan P. Gardner, John C. Mather, Mark Clampin, et. al., Title: The James Webb Space Telescope, Published: 15 May 2006, Publisher: Space Science Reviews (2006) 123: 485–606

[15] Author: Philip J. Armitage, Title: Dynamics of Protoplanetary Disks, Published: 23 Aug 2011, Publisher: Annual review Stronomy & Astrophysics, 49, 195-236

[16] Author: Michael Kuffmeier, Troels Haugbølle, and Åke Nordlund, Title: Zoom-in Simulations of Protoplanetary Disks Starting from GMC Scales, Published: August 24 2017, Publisher: The Astrophysical Journal, 846:7 (21pp)

[17] Author: T. Birnstiel, C. P. Dullemond, and F. Brauer , Title: Gas- and dust evolution in protoplanetary disks, Published: 26 January 2010, Publisher: Junior Research Group at the Max-Planck-Institut für Astronomie

[18] Author: L. Mattsson, J. P. U. Fynbo, B. Villarroel Title: Small-scale clustering of nano-dust grains in supersonic turbulence , Published: 17 October 2019, Publisher: Monthly Notices of the Royal Astronomical Society 000, 1–11 (2019)

[19] Author: Sarah Lewin, Title: Life on Earth Can Thank Its Lucky Stars for Jupiter and Saturn, `https://www.space.com/31577-earth-life-jupiter-saturn-giant-impacts.html`, Last Updated: January 12, 2016

[20] Author: Mark Heyer, Coleman Krawczyk, Julia Duval, and James M. Jackson , Title: Re-examining Larson's scaling relationships in galactic molecular clouds, Published: 18 June 2009, Publisher: The Astrophysical Journal

[21] Author: Richard B. Larson, Title: Turbulence and star formation in molecular clouds, Published: 1981, Publisher: Monthly Notices of the Royal Astronomical Society (1981) 194, 809-826

[22] Author: Nancy Hall, Title: Mach Number, `https://www.grc.nasa.gov/www/k-12/airplane/mach.html`, Last Updated: Oct 09 2019

[23] Author: J. Kainulainen and J. C. Tan, Title: High-dynamic-range extinction mapping of infrared dark clouds Dependence of density variance with sonic Mach number in molecular clouds, Published: 30 October 2012, Publisher: Astronomy and Astrophysics

[24] Author: Guillaume Laibe and Daniel J. Price , Title: Dusty gas with SPH — II. Implicit time stepping and astrophysical drag regimes, Published: 21 August 2018, Publisher: Centre for Stellar and Planetary Astrophysics and School of Mathematical Sciences

[25] Author: John S. Mathis, Title: Molecular cloud, `https://www.britannica.com/science/molecular-cloud`, Last Updated: May 08, 2020.

[26] Author: Uriel Frisch , Title: Turbulence: The Legacy of A.N. Kolmogorov , Published: November 1995, Publisher: Cambridge University Press

[27] Author: Weisstein, Eric W., Title: Root-Mean-Square., `https://mathworld.wolfram.com/Root-Mean-Square.html`, Last Updated: 2021

[28] Author: T. Padmanabhan, Title: Theoretical Astrophysics: Volume 3, Galaxies and Cosmology, Published: 2000, Publisher: Cambridge University Press, pages: 86

[29] Author: Online Dictionary of Crystallography, Title: Cross-section , `https://dictionary.iucr.org/Cross-section`, Last Updated: 12 March 2018

[30] Author: Donna Roberts, Title: Spheres and Hemispheres , `https://mathbitsnotebook.com/Geometry/3DShapes/3DSpheres.html`, Last Updated: 2021

[31] Author: Barbara Ryden, Title: Dynamics, Published: 18. February 2016, Publisher: The Ohio State University, Page: 161 - 196

[32] Author: Bastian Körtgen, Christoph Federrath, and Robi Banerjee , Title: The driving of turbulence in simulations of molecular cloud formation and evolution , Published: 22 March 2017, Publisher: Monthly Notices of the Royal Astronomical Society, Volume 472, Issue 2

[33] Author: D. Falceta-Gonçalves, G. Kowal, E. Falgarone, and A. C.-L. Ch, Title: Turbulence in the interstellar medium, Published: 16 May 2014, Publisher: Nonlin. Processes Geophys., 21, 587–604

[34] Author: Murdin, Paul, Title: Encyclopedia of astronomy and astrophysics, Published: 2001, Publisher: IOP Publishing and London: Nature Publishing

[35] Author: Ake Nordlund, Jon P. Ramsey, Andrius Popovas, and Michael Kuffmeier , Title: DISPATCH: A Numerical Simulation Framework for the Exa-scale Era. I. Fundamentals, Published: February 2018, Publisher: Monthly Notices of the Royal Astronomical Society, Vol. 477, No. 1, 2018, p. 624-638

[36] Author: Karla Morris, Title: Emulating Multiple Inheritance in Fortran 2003/2008, Published: 24 January 2015, Publisher: Hindawi Publishing Corporation

[37] Author: J. E. Akin, Title: Object Oriented Programming via Fortran 90, Published: 1999, Publisher: Engineering Computations, v. 16, n. 1, pp. 26-48

[38] Author: Miles D. Cranmer, Benjamin R. Barsdell, Danny C. Price et. al., Title: Bifrost: A Python/C++ Framework for High-Throughput Stream Processing in Astronomy, Published: October 12 2017, Publisher: Journal of Astronomical InstrumentationVol. 06, No. 04

[39] Author: P.E.Farrell, M.D.Piggott, C.C.Pain et. al., Title: Conservative interpolation between unstructured meshes via supermesh construction, Published: 1 July 2009, Publisher: Computer Methods in Applied Mechanics and Engineering, Volume 198, Issues 33–36

[40] Author: G.Beliakov, H.Bustince, D.P.Goswami, U.K.Mukherjee, N.R. Pal, Title: On averaging operators for Atanassov's intuitionistic fuzzy sets, Published: 15 March 2011, Publisher: Information Sciences Volume 181, Issue 6

[41] Author: Romain Teyssier, Title: Cosmological Hydrodynamics with Adaptive Mesh Refinement A New High Resolution Code Called RAMSES, Published: 2002, Publisher: Astronomy and Astrophysics

[42] Author: Thomas Y. Hou and Philippe G. Le Floch, Title: Why nonconservattive schemes converge to wrong solutions: error analysis, Published: April 1994, Publisher: Mathematics of computation volume 62, Number 206

[43] Author: Peter K. Sweby, Title: Godunov Methods, Published: October 1999, Publisher: Department of Mathematics, The University of Reading

[44] Author: Sandra May and Marsha Berger, Title: Two-dimensional slope limiters for finite volume schemes on non-coordinate-aligned meshes, Published: 10 September 2013, Publisher: SIAM Journal on Scientific Computing, Volume 35, Issue 5

[45] Author: Liubin Pan, Paolo Padoan, Title: Turbulence-Induced Relative Velocity of Dust Particles I: Identical Particles, Published: 9 Aug 2013 , Publisher: American Astronomical Society, The Astrophysical Journal